



Universiteit
Leiden
The Netherlands

The symmetry of crystals and the topology of electrons

Slager, R.J.

Citation

Slager, R. J. (2016, January 12). *The symmetry of crystals and the topology of electrons*. Retrieved from <https://hdl.handle.net/1887/37232>

Version: Corrected Publisher's Version

License: [Licence agreement concerning inclusion of doctoral thesis in the Institutional Repository of the University of Leiden](#)

Downloaded from: <https://hdl.handle.net/1887/37232>

Note: To cite this publication please use the final published version (if applicable).

Cover Page



Universiteit Leiden



The handle <http://hdl.handle.net/1887/37232> holds various files of this Leiden University dissertation.

Author: Slager, Robert-Jan

Title: The symmetry of crystals and the topology of electrons

Issue Date: 2016-01-12

The symmetry of crystals and the topology of electrons

PROEFSCHRIFT

TER VERKRIJGING VAN DE GRAAD
VAN DOCTOR AAN DE UNIVERSITEIT LEIDEN,
OP GEZAG VAN DE RECTOR MAGNIFICUS
PROF. MR. C. J. J. M. STOLKER,
VOLGENS BESLUIT VAN HET COLLEGE VOOR PROMOTIES
TE VERDEDIGEN OP DINSDAG 12 JANUARI 2016
KLOKKE 16.15 UUR

DOOR

Robert-Jan Slager

GEBOREN TE GOES (ZEELAND), NEDERLAND IN 1988

Promotor: Prof. dr. J. Zaanen, Universiteit Leiden
Co-promotor: Dr. V. Juričić, NORDITA

Promotiecommissie: Prof. dr. E. R. Eliel, Universiteit Leiden
Prof. dr. K. E. Schalm, Universiteit Leiden
Prof. dr. X. -L. Qi, Stanford University
Prof. dr. F. von Oppen, Freie Universität Berlin
Prof. dr. M. S. Golden, Universiteit van Amsterdam
Dr. V. V. Cheianov, Universiteit Leiden

Casimir Ph.D. series, Delft-Leiden, 2015-22
ISBN 978-90-8593-230-7

Dit werk maakt deel uit van het onderzoekprogramma van de Stichting voor Fundamenteel Onderzoek der Materie (FOM), die deel uit maakt van de Nederlandse Organisatie voor Wetenschappelijk Onderzoek (NWO).

This work is part of the research programme of the Foundation for Fundamental Research on Matter (FOM), which is part of the Netherlands Organisation for Scientific Research (NWO).



To my 4+1 dimensional family

Contents

1	Introduction	1
1.1	Essentials of topological band theory	3
1.1.1	The Integer Quantum Hall effect	4
1.1.2	Quantum anomalous Hall effect	7
1.1.3	\mathbb{Z}_2 topological band insulators	9
1.1.4	General perspective and the tenfold way	12
1.2	Topics of this thesis	13
1.3	This thesis	16
1.A	Adiabatic curvature and Chern numbers	18
2	Phenomenology of topological band insulators	21
2.1	Bulk perspective	21
2.1.1	Anomalous quantum Hall and quantum spin Hall models	21
2.1.2	Three dimensional \mathbb{Z}_2 topological band insulators	24
2.1.3	Field theories of \mathbb{Z}_2 topological band insulators	24
2.2	Edge state perspective	26
2.2.1	Jackiw-Rebbi solitons in the Su-Schrieffer-Heeger model	26
2.2.2	Two dimensional topological band insulators	29
2.2.3	Three dimensional \mathbb{Z}_2 topological band insulators	31
3	Universal bulk probes of the \mathbb{Z}_2 topological insulator	35
3.1	Zero-modes bound to a π -flux vortex	36
3.1.1	Self-adjoint extension	40
3.2	Quantum numbers of the zero-energy modes	44
3.3	π -fluxes as a bulk classification tool	45

3.4	Dislocations as probes of the physics beyond the tenfold way	47
3.5	Conclusions	52
4	The space group classification of topological band insulators	53
4.1	Classification scheme and general principles	54
4.1.1	Three spatial dimensions	61
4.2	Topological signatures in the Greens function structure	63
4.3	The space group classification as an experimental guide	68
4.4	Conclusions	69
4.A	Verification within M-B model setting	70
4.B	Probing the topologically non-trivial phases	74
4.C	Topological signatures in the Greens function structure	79
4.C.1	Details codimension-1 case	79
4.C.2	Details codimension-2 case	81
5	The K-b-t rule	83
5.1	Formulation and general principles	84
5.2	Implications of the rule	88
5.3	Exemplification	89
5.4	Experimental consequences	91
5.5	Conclusions	92
5.A	Model details	93
5.B	Analytical and numerical evaluation of dislocations modes in three dimensional \mathbb{Z}_2 topological insulators	96
5.B.1	Edge dislocations	96
5.B.2	Screw dislocations	104
6	Isospinless graphene on grain boundaries in topological band insulators	111
6.1	General principles underlying the emergence of semi-metals at grain boundaries	113
6.2	Stability of the spinon metal	119
6.3	Experimental signatures	120
6.4	Conclusions	122
6.A	Emergent time reversal symmetric semi-metals at grain boundaries . . .	124
6.A.1	Lattice dislocations and spinon zero mode hybridization	124

6.A.2 Helical modes on dislocation lines and their hybridization . . .	126
6.A.3 Analytical motivation	129
6.B Disorder analysis of the grain boundary states	133
7 Conclusions and outlook	137
References	141
List of Publications	157
Samenvatting	159
Curriculum Vitae	163
Acknowledgements	165

Chapter 1

Introduction

Einstein famously stated: *"It can scarcely be denied that the supreme goal of all theory is to make the irreducible basic elements as simple and as few as possible without having to surrender the adequate representation of a single datum of experience"* [1]. A gas, the state of all matter at sufficiently high temperatures, is one of the simplest systems in physics and therefore allows for an effective theory that meets this aspiration most straightforwardly. The associated model minimally consists of weakly-interacting point particles. Nevertheless, as the temperature is lowered, interactions between the constituents start to correlate their motion and eventually lead to a regular crystalline structure in which the individual atoms can hardly move. The resulting crystalline order exemplifies a strongly-correlated state, which cannot be captured by the simple gas model, and confronts one with the inspiring observation that the translation to more generally entails a formidable process [2]. The elegance, however, is in these cases to be retrieved in the elementary principles of the *emergent* laws, that tend to universally reproduce those of traditional fundamental theories, including gauge and even string theories.

Aspects of condensed matter physics revolve around this question of how macroscopic orders emerge due to interactions between the elementary constituents. In a lot of instances this can be explained by means of symmetry breaking. The formation of a periodic crystal lattice, for instance, arises due to the electrostatic repulsion of the ions, breaking in turn the continuous translational and rotational symmetries of Euclidean space. The corresponding symmetry classification of order has been well understood since the 1950's, predominantly by virtue of the work of Landau [3, 4]. Each ordered

phase is characterized by an order parameter that quantifies the symmetry breaking and different phases are separated by phase transitions that are signaled by singularities in the free energy functional. Close to the phase transition the free energy can consequently be expanded, leading to a phenomenological Ginzburg-Landau theory that reflects the relevant symmetries. In some instances even the excitations, such as the phonons in the crystal example, are intimately connected with the symmetry analysis, as the spontaneous breaking of a continuous symmetry is necessarily accompanied by gapless degrees of freedom [5, 6]. In conjunction with Landau-Fermi liquid theory, which exhausts the Pauli and adiabatic principle to treat interacting Fermion systems as a collection of free quasi-particles with perturbatively incorporated interactions, it hence appeared that, at least at a conceptual level, all phases of condensed matter could be characterized. Indeed, for quite some time there were no systems that could not effectively be captured by renormalization group methods or perturbation schemes falling within this Landau-Fermi liquid paradigm.

However, in the past few decades condensed matter has been astounded by new experimental results and signatures, that necessitate physical descriptions outside the above-mentioned scope. On one hand, the discovery of high-temperature superconductors [7] has fueled an intensive research effort in understanding non-Fermi liquid-like 'strange' metallic states. Interestingly, this has lead to the mobilization of a holographic duality [8, 9] known as the AdS/CFT correspondence [10, 11, 12]. This duality provides for a mapping of a strongly coupled d -dimensional conformal field theory to a weakly coupled string theory living in a $d + 1$ Anti-de Sitter space and therefore has significant potential value in dealing with strongly correlated systems turning conformal at a phase transition. Recent endeavors and progress even revolve around application away from strict conformality. On the other hand, the discovery of quantum Hall states [13, 14] impelled the emergence of a completely different characterization of order based on the concept of topology.

Topology essentially is the study of classes of objects invariant under smooth deformations, mathematically described by so-called homotopies. Heuristically, this amounts to the notion that a coffee cup, for instance, can smoothly be deformed into a torus, whereas for the two-sphere this is not possible. More concretely, it is possible to assign invariants to distinguish the resulting topological equivalence classes, serving as analogues of the order parameters associated with broken symmetries. This topological description of matter will set the appropriate stage for the remainder. In particular,

the notion of topology may be used to classify band structures, being maps from well-defined Brillouin zones into the Bloch space of Hamiltonians. Topological considerations of these maps then define invariants characterizing different equivalence classes of knotted electronic spectra, that cannot continuously be deformed into each other. This description is evidently robust as long as the system is an insulator and therefore leads to the notion of topological insulating states that can be distinguished from the trivial counterparts.

A notable physical signature of a nontrivial topological band structure is the existence of metallic states localized to the perimeter of the system. These edge states are a consequence of a deeper correspondence that relates the topological entity characterizing the bulk to gapless modes at the boundary and in essence shares similarities with the holographic principle. This thesis is concerned with reminiscent signatures of topological order in band theory by exploring the physics of *defects*, with the emphasis on dislocations. We will find that in addition to a plethora of interesting mechanisms, which are related to the defects themselves and culminate, inter alia, in helical propagating fermionic modes bound to freely deformable channels and exotic isospinless graphene-like states, these results in turn expose an extension of the classification of topological band insulators by incorporating the underlying space group symmetries. To make this explicit, we set off sketching the appropriate context by motivating some essential concepts of topological band theory.

1.1 Essentials of topological band theory

The flourishing of topological considerations in condensed matter physics was sparked by the study of quantum Hall effects [13, 14]. These Hall effects are realized in two dimensional electron systems subjected to sufficiently low temperatures and high external magnetic fields and pertain to the phenomenon that the Hall conductance σ_{xy} shows sharply quantized plateaus. Instances of these plateaus occurring at integer and fractional values of the unit of conductance $\frac{e^2}{h}$ have been observed and therefore lead to the notion of the integer and fractional quantum Hall effect, respectively. In spite of the apparent physical connection, these Hall effects nevertheless feature profound differences. The fractional quantum Hall effect (FQHE) is found to have an inherent topological nature [15] or long range entanglement [16], signaled by a ground state degeneracy and frac-

tional excitations, and consequently necessitates a description that relies on a many body approach [17]. In contrast, the integer quantum Hall effect (IQHE) is adequately captured by a single particle quantum mechanical picture, that nonetheless also allows for topological considerations. Indeed, the IQHE represents one of the fundamental examples of topological order and lies at the heart of topological band theory.

1.1.1 The Integer Quantum Hall effect

Turning to the integer quantum Hall effect, the corresponding Hamiltonian takes the plain form

$$H(x_1, x_2) = -\frac{1}{2m} \sum_i (\hbar \partial_i - \frac{iq_e A_i}{c})^2, \quad (1.1)$$

where m, q_e denote the electron mass and charge, the index $i = 1, 2$ refers to the coordinates and the vector potential $(A_1, A_2)^\top = \frac{B}{2}(-x_2, x_1)$ is evaluated in the CGS valued symmetric gauge in terms of the uniform magnetic field B . The above Schrödinger equation can subsequently further be simplified upon applying a similarity transformation generated by $G = \exp(\frac{x_1^2 + x_2^2}{4l_B^2})$, where the magnetic length is defined as $l_B^2 = |\frac{c\hbar}{eB}|$ and relates to the unit flux quantum $\Phi_0 = \frac{hc}{e}$ via $2\pi l_B^2 = \Phi_0$. Specifically, in complex coordinates $z = x + iy$ and $\bar{z} = x - iy$ the Hamiltonian may then be rewritten as

$$H(z, \bar{z}) = -\frac{2\hbar^2}{m} \exp(\frac{-|z|^2}{4l_B^2}) [(\partial_z - \frac{\bar{z}}{2l_B^2}) \partial_{\bar{z}}] \exp(\frac{|z|^2}{4l_B^2}) + \frac{1}{2} \hbar \omega_c. \quad (1.2)$$

This form immediately exposes the eigenstates of the quantized Landau level structure in terms of the cyclotron frequency $\omega_c = \frac{q_e B}{mc}$ and the eigenfuctions $\Psi_n(z, \bar{z})$ corresponding with the energies $E = (n + \frac{1}{2}) \hbar \omega_c$ are given by

$$\Psi_n(z, \bar{z}) = \exp(\frac{-|z|^2}{4l_B^2}) \mathcal{A}^n \mathcal{F}(z), \quad (1.3)$$

were $\mathcal{A} = \partial_z - \frac{\bar{z}}{2l_B^2}$ and $\mathcal{F}(z)$ is a holomorphic function. Furthermore, we have assumed that $q_e B > 0$, by virtue of $q_e B < 0$ yielding a similar calculation in terms of eigenfuctions that require an anti-holomorphic function $\mathcal{F}(\bar{z})$. A more noteworthy observation regarding the Hamiltonian (1.2) pertains to the fact that the ordinary translations generated by ∂_z and $\partial_{\bar{z}}$ do not commute with the Hamiltonian. Instead, one should define magnetic translational operators $k = \partial_z - \frac{\bar{z}}{4l_B^2}$ and $\bar{k} = \partial_{\bar{z}} - \frac{z}{4l_B^2}$, satisfying

$$[H, k] = [H, \bar{k}] = 0, \quad [k, \bar{k}] = \frac{1}{2l_B^2}, \quad (1.4)$$

which in turn result in the definition of a *magnetic* transitional algebra, playing an important role in the geometrical understanding of the IQHE [18]. To complete the characterization of the IQHE eigenstates one also has to take into account the degeneracy. In the outlined symmetric gauge, the wave functions can accordingly most easily be labeled by angular momentum. This is particularly evident for the lowest Landau level. As $\mathcal{F}(z)$ is holomorphic, Ψ_0 can be expanded in the basis states $\phi_m(z) = \alpha z^m \exp(\frac{-|z|^2}{4l_B^2})$, carrying angular momentum m . These functions have a ring shape and the corresponding area can be shown to enclose m flux quanta, which demonstrates that the number of states in this Landau level is exactly equal to the number of flux quanta. Henceforth, we observe that when the filling factor ν of particles over flux quanta equates to unity each state is exactly occupied, giving a direct explanation for the observed plateau by the Pauli exclusion principle.

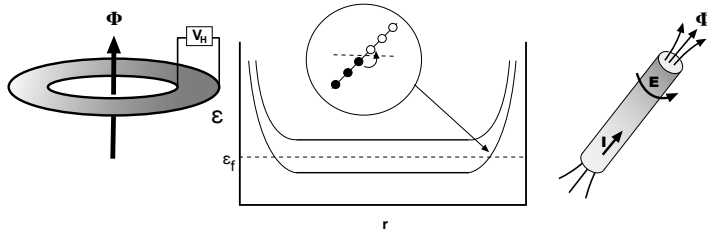


Figure 1.1: *The two left panels illustrate the Laughlin argument on an annulus. The Fermi energy is located in the gap resulting in ν filled Landau levels. As the confining potential pushes the energy levels up at the edges, this also implies ν metallic edge states. Adiabatic insertion of a unit flux quantum $\frac{hc}{e}$ then maps the system onto a gauge equivalent copy, but induces a spectral flow. Specifically, ν states sink below the Fermi surfaces at the inner edge and are transported to the outer edge. This directly results in a quantized transverse Hall conductivity σ_{xy} . Correspondingly, generating a Faraday electric field by threading an IQHE state on a cylinder geometry with the same flux prompts a similar transport of an integral number of electrons from one end to the other.*

Although the above analysis gives some clues about the incompressibility and nature of the IQHE by straightforward generalization to arbitrary integer filling, the real underlying physics finds its foundation in the the role of the associated topology. Laughlin was the first to realize in this regard that given its complete universality the quantization must be insensitive to continuous deformations of the sample geometry and deeply rooted in

the gauge principle. That is, he realized that the periodicity emerging from the gauge invariance allows for an adiabatic quantum pump interpretation of the system [19]. Basically, inserting adiabatically a unit of quantum flux defines the cycle of the quantum pump and maps the system on a gauge equivalent copy, leaving the total basis of single electron functions unchanged. This does not mean, however, that the individual basis states get mapped on themselves. Indeed, the flux insertion procedure effectively shifts the individual angular momentum m eigenfunctions to $m + 1$. Consequently, completing one cycle results in the transport of an integral number of states from one edge to the other, which can readily be shown to yield a quantized transverse conductivity $\sigma_{xy} = \nu \frac{e^2}{h}$ (see Figure 1.1). This analysis does moreover not depend on the specific geometry of the system and can similarly be applied to a cylinder (see Figure 1.1). Correspondingly, analogous arguments have also shown to be applicable in the treatment of, for example, one dimensional charge pumps associated with an one dimensional charge polarization during the Laughlin cycle [20, 21].

The Laughlin argument then provides for the final stepping stone on the road towards the topological characterization of the IQHE, specifying the distinction to normal band insulators. The explicit connection was established by Thouless et al. [22, 23]. They showed that the charge transported during the adiabatic flux change, as may be calculated with the Kubo formula [24], can be recognized as an integer topological invariant; it is the first Chern class of a $U(1)$ principle fibre bundle on a torus, with the magnetic Brillouin zone being the torus and the Bloch waves the corresponding fibres [25, 26]. The resulting integer invariants are accordingly known as first Chern characters. Although the details are left to Appendix 1.A, the basic idea is that these Chern characters quantify the twisting of the bundles during one cycle. Heuristically speaking, the wave functions experience curvature during adiabatic transport over the underlying Brillouin zone and the integration of such curvature then results in a topological invariant. This can be viewed as a generalization of the Gauss-Bonnet theorem

$$\int_M K dA = 2\pi\chi(M), \quad (1.5)$$

which relates the Euler characteristic $\chi(M) = 2 - 2g$, quantifying a topological number by counting the number of 'handles' or genus g , to the analytic procedure of integrating the local curvature K over the closed manifold M . As a result, the total Hall conductance is exactly equal to the sum over all the first Chern characters \mathcal{C}_m^1 corresponding to the

occupied bands m

$$\sigma^{xy} = \frac{e^2}{h} \sum_m \mathcal{C}_m^1.$$

The above relation may then be regarded as the embodiment of the fundamental role of topology; it directly connects the physical signature σ_{xy} to a topological invariant, that is robust as long as the system remains gapped, and is also in direct accordance with the number of edge states.

1.1.2 Quantum anomalous Hall effect

The topological characterization of the IQHE is intimately related with the breaking of time reversal symmetry (TRS), which is effectively incorporated by the introduction of the magnetic field. Strikingly, it was found that such integer quantum Hall states can also be realized in band theory models without a net magnetic field. An influential example of such anomalous quantum Hall effect is the Haldane model [27]. This model is significant as it directly translates the notions of the previous subsection to a simple two band model and, from a historical point of view, paved the way to the concept of the \mathbb{Z}_2 topological band insulator.

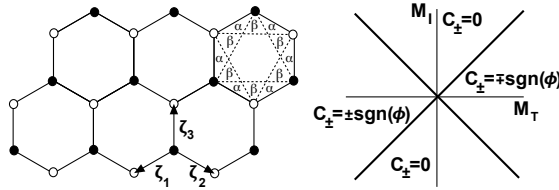


Figure 1.2: Honeycomb lattice of graphene consisting of the triangular lattice A (black sites) and the triangular lattice B (white sites). The vectors connecting the nearest neighbors are given by $\zeta_1 = \frac{a}{2\sqrt{3}}(-\sqrt{3}\mathbf{e}_x - \mathbf{e}_y)$, $\zeta_2 = \frac{a}{2\sqrt{3}}(\sqrt{3}\mathbf{e}_x - \mathbf{e}_y)$ and $\zeta_3 = \frac{a}{\sqrt{3}}\mathbf{e}_y$. In the Haldane model [27] the assumed fluxes Φ_α/Φ_β through regions α/β , belonging to the two different sub lattices, add up to zero for the hexagons marking closed nearest neighbor paths, but result in a phase for the next nearest neighbor hopping terms (dashed lines). Specifically, these hoppings become of the form $t_2 e^{i\phi}$, with $\phi = 2\pi(2\Phi_\alpha + \Phi_\beta)/\Phi_0$, and result in a time reversal breaking mass term M_T . This mass term drives the system into an anomalous quantum Hall regime, when it exceeds the inversion breaking mass M_I .

The Haldane model is based on the simplest tight-binding model of graphene, describing the π electrons [28, 29, 30]. In the two component basis associated with the spin suppressed Bloch states on each sub lattice, the Hamiltonian assumes the form

$$H(\mathbf{k}) = \begin{pmatrix} 0 & \Gamma(\mathbf{k}) \\ \Gamma(\mathbf{k})^* & 0 \end{pmatrix}, \quad \Gamma(\mathbf{k}) = -t \sum_{m=1}^3 \exp(i\mathbf{k} \cdot \boldsymbol{\zeta}_m), \quad (1.6)$$

where $\boldsymbol{\zeta}_1, \boldsymbol{\zeta}_2, \boldsymbol{\zeta}_3$ are the nearest neighbor vectors connecting the two sub lattices (Figure 1.2). The resultant spectrum at half filling is a semimetal and the two bands touch at the corners of the hexagonal Brillouin zone. Moreover, the energy dispersion in the vicinity of these points is linear and as a result the effective continuum theory is given by a massless Dirac Hamiltonian, that is obtained by expanding around the two inequivalent Fermi points $\mathbf{k}_+ = -\mathbf{k}_- = \frac{4\pi}{3a}\mathbf{e}_x$. Concretely, in terms of the usual Pauli matrices $\boldsymbol{\tau}$, Fermi velocity $v_f = \frac{\sqrt{3}at}{2\hbar}$ and $\mathbf{q}_{\pm} \equiv (\mathbf{k} - \mathbf{k}_{\pm})$ the result in leading order is readily verified to be

$$H_{\pm}^{eff}(\mathbf{q}) = \pm v_f (\tau_x q_{x\pm} \pm \tau_y q_{y\pm}). \quad (1.7)$$

The Hamiltonian (1.6) posses inversion symmetry as well as time reversal symmetry. Indeed, the combination of the two requires the absence of terms proportional to τ_z and ultimately results in the protection of the degeneracies at $\mathbf{q} = 0$. When these symmetries are broken the degeneracies can be lifted. For example, if the two atoms in the unit cell are made inequivalent, one obtains an inversion symmetry breaking mass term that is proportional to $M_I \tau_z$ for small M_I . This results in a normal insulating state. Haldane, however, imagined introducing a second neighbor hopping term accompanied by a staggered flux, which adds up to zero for each hexagon (Figure 1.2). Accordingly, the next nearest neighbor hoppings attain a phase, producing a time reversal symmetry breaking mass term $\pm M_T \tau_z$ that has an *opposite* sign at \mathbf{k}_+ and \mathbf{k}_- . Explicit calculation of the first Chern character in presence of M_I and M_T then shows the existence of the quantum Hall state when $|M_T| > |M_I|$, producing the phase diagram shown in Figure 1.2. These results hold similarly for the lattice regularized model. Moreover, upon crossing the critical lines $|M_T| = |M_I|$ the system develops chiral edge states; the two bands are inverted closing the gap at one of the Dirac points and the nontrivial regime features two opposite metallic chiral movers, bound to opposite surfaces of the system. On a deeper level, one should therefore actually interpret this model as the condensed matter realization of the parity anomaly, which is manifest in the associated field theory and intimately related to the fact that the chiral movers are localized to the surface. For the present discussion,

however, we accentuate that the crucial observation pertains to the fact that the Haldane model provides for a concrete route of realizing a nontrivial Chern character, and thus non-zero Hall conductance, per spin component.

1.1.3 \mathbb{Z}_2 topological band insulators

Recently, the concepts of topological band structures were rekindled by incorporating the spin degree of freedom and the associated role of time reversal symmetry, leading in two spatial dimensions to an analog of the quantum Hall effect, known as the quantum spin Hall effect. The first system exhibiting such a spin Hall effect was proposed by Kane and Mele [31, 32] and entails a generalization of the Haldane model. Specifically, reverting to the spinful variant of the graphene Hamiltonian, one observes that the model allows for a mass term of the form

$$M_{SO} = \pm \lambda_{SO} \tau_z \sigma_z, \quad (1.8)$$

where \pm refers to the two Dirac points and the matrix σ_z acts in spin space. This term respects all symmetries, but moreover couples the spin to the hopping. As a result, the $\sigma_z = \pm 1$ Haldane copies have an opposite Hall conductivity. Nonetheless, the system can now be shown to develop a net *spin* current and, in analogy with the Haldane model, the spin Hall phase exhibits a *single* pair of counter-propagating helical edge states. As in that case, the Nielsen-Nimomiya theorem [33, 34] demanding lattice fermion doubling for the lattice regularized counterpart is evaded by virtue of these states living on the boundary of a bulk lattice system.

The spin filtered property of the edge states already reveals that they are not susceptible to Anderson localization and signals robustness to backscattering if time reversal symmetry is maintained. These notions can be shown to be profound. It turns out that the presence of time reversal symmetry plays a key role and allows for a topological characterization analogous to the definition of the Chern character, which is zero due to its presence. In particular, time reversal symmetry imposes specific conditions on the Bloch waves as fibres of the torus defined by the Brillouin zone; the corresponding anti-unitary operator Θ has the property $\Theta^2 = -1$ and relates states with opposite momenta $|u_i(-\mathbf{k})\rangle = \Theta|u_i(\mathbf{k})\rangle$. This means that the associated bundle is so-called twisted and results in a $\mathbb{Z} \times \mathbb{Z}_2$ classification [25, 35, 36]. The \mathbb{Z}_2 invariant ν subsequently distinguishes the trivial insulating phase ($\nu = 0$) from the topological spin Hall phase

($\nu = 1$), providing for a direct relation to the edge state description. Namely, as time reversal symmetry imposes $\Theta H(\mathbf{k}) \Theta^{-1} = H(-\mathbf{k})$, points in the Brillouin zone satisfying $H(\mathbf{k}) = H(-\mathbf{k})$ host protected Kramers degeneracies. In the quantum spin Hall phase the Kramers pairs then essentially switch partners an odd number of times, leading to an odd number of crossings of the Fermi surface and an associated spectrum that cannot continuously be deformed into a trivial insulator. Alternatively, one can also relate to the Laughlin argument. This is particularly evident in case of S_z conservation. In that instance, a Laughlin cycle amounts to the transport of a spin up state from one edge to the other as well as the simultaneous transfer of a down state in opposite direction. As a result, it is evident that in a \mathbb{Z}_2 topological band insulator the insertion of half a flux-quantum results in a change of the Kramers degeneracy associated with the ends. Although in the general case this labeling of the spin with respect to a specific axis is no longer valid, the change in degeneracy nonetheless remains well-defined, conveying the direct physical meaning of the \mathbb{Z}_2 invariant.

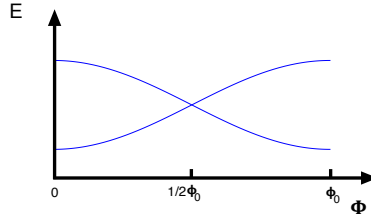


Figure 1.3: The \mathbb{Z}_2 invariant pertains to the change in time reversal polarization when a half unit flux-quantum is adiabatically inserted. Heuristically, in the case of S_z conservation, the two reduced Hamiltonian operators, corresponding with the z projections of the spin, feature an opposite odd integer quantum Hall spectral flow, or charge polarization, during a Laughlin cycle. Accordingly, considering a \mathbb{Z}_2 topological insulator on a cylinder, just as in the right panel of Figure 1.1, the many body levels evolve schematically as illustrated during this process. Although in the general scenario S_z conservation is lost, the change in degeneracy associated with the ends, being the change in time reversal polarization, remains adequate

While the \mathbb{Z}_2 topological band insulator is intimately related with the Quantum Hall effect, general mathematical arguments show that notion of the spin Hall state, or two dimensional \mathbb{Z}_2 insulator, can in contrast be generalized to three spatial dimensions

[37, 38, 39]. Considering *only* time reversal symmetry, one can then define four \mathbb{Z}_2 invariants $(\nu_0, \nu_1, \nu_2, \nu_3)$. Specifically, the ν_0 invariant entails the generalization of the two dimensional invariant and amounts to whether the Fermi surface encloses an even or odd number of Kramers degenerate points. When this is the case ($\nu_0 = 1$) the system is commonly referred to as a 'strong' topological insulator. This is an intrinsically nontrivial state, just as its two-dimensional counterpart. The remaining three invariants, on the other hand, then pertain to Miller indices reflecting the two dimensional cuts of the Brillouin zone in which the Kramers pairs switch partners. These indices hence refer to the position of the Dirac cone in the strong case, but also lead to notion of the 'weak' topological insulator. In that case the system is imagined to be a stacking of spin Hall effects in the direction of the vector formed by the weak indices, although the total invariant ν_0 equates to zero. However, as this procedure does not define a generic topological state protected by time reversal symmetry, a 'weak' topological insulator is prone to disorder and has no protected surface states. More importantly, since one is assuming a specific stacking and consequently an extra translational symmetry, this raises the fundamental question whether these invariants are actually physically relevant in the light of space group symmetries that classify lattice symmetries unambiguously. We will in fact address this question in detail in the subsequent chapters.

\mathbb{Z}_2 topological band insulators are not only a interesting display of topological notions in free fermion systems. Indeed, although the spin orbit coupling term in graphene is relatively weak, the spin Hall effect has been proposed [40] and observed [41] in HgTe/CdTe quantum wells. In addition, angle-resolved photo emission spectroscopy (ARPES) experiments identified the first three dimensional topological insulator $\text{Bi}_x\text{Sb}_{1-x}$ [42] in 2008. This initiated the search search for topological insulators made out of heavy elements, showing relatively strong spin-orbit interactions and small band gaps, and culminated in the discovery of the 'second generation' topological insulating bismuth/antimony alloys, like Bi_2Se_3 , Bi_2Te_3 and Sb_2Te_3 [43, 44, 45]. These experimental realizations as such then provide for one of the more consequential motives that drive and signify the active field of topological band theory.

1.1.4 General perspective and the tenfold way

The \mathbb{Z}_2 topological band insulator crucially depends on time reversal symmetry, as its presence allows for distinct topological maps from the Brillouin zone into the Bloch space of Hamiltonians. The generality of this analysis is elegantly reflected in a more universal framework describing free fermion matter, referred to as the "tenfold way". Concretely, specifying Hamiltonians in terms of their time reversal, particle hole and chiral symmetries, one obtains ten different classes [46]. Application of the mathematical machinery of K theory [47] or the consideration of the associated topological field theory and the resulting surface states [48, 49] then allows for the determination of the number of distinct topological phases for each of these classes in spatial dimension d , resulting in the anticipated classification scheme. This periodic table (Table 1.1) thus in particular signifies that the \mathbb{Z}_2 topological band insulator (AII, $d=2,3$) should be regarded as a particular instance of a topological phase that arises by virtue of symmetry.

From a broader perspective, the classification of such symmetry protected topological (SPT) phases has emerged as an actual prominent research theme and has also entered the domain of interacting boson systems. In particular, it has been coined that the topological order of $d + 1$ dimensional systems can be classified in terms of their underlying symmetry group SG by the respective cohomology $H^{d+1}(SG, U(1))$ [50, 51]. These ideas were subsequently generalized to cases entailing a total symmetry group G , where the symmetry group is extended with a gauge group GG as a direct product $G = SG \times GG$ [52]. Moreover, similar efforts have also been taken to lift these constructions to so-called super cohomology groups in order to address interacting fermion systems [53]. To a significant extend these notions are all similar and on a very heuristic level the cohomology group arguments actually pertain to the number of ways there exist to thread magnetic fluxes into a manifold such that the underlying symmetry group is respected [54]. More concretely, these ideas find their inspiration in the well-known Dijkgraaf-Witten invariants classifying topological field theories with a compact gauge group [55], as they directly convey the topological meaning of the cohomology groups by linking them to topological geometry of the underlying manifold. As such these computations are on a firm footing. Nonetheless, in the condensed matter context the connection to physical systems is in fact so far only made explicit in terms of exactly solvable models, rendering the *general* completeness and universal validity still in the dark. It is evident, however, that due to their robustness topological classification tools

based on symmetry are very powerful. This therefore reinforces to a certain extent the interest in quantum Hall states and \mathbb{Z}_2 topological band insulators, where the topological considerations are directly traceable to experiments.

AZ	Θ	Ξ	Π	1	2	3	4	5	6	7	8
A	0	0	0	0	\mathbb{Z}	0	\mathbb{Z}	0	\mathbb{Z}	0	\mathbb{Z}
AIII	0	0	1	\mathbb{Z}	0	\mathbb{Z}	0	\mathbb{Z}	0	\mathbb{Z}	0
AI	1	0	0	0	0	0	\mathbb{Z}	0	\mathbb{Z}_2	\mathbb{Z}_2	\mathbb{Z}
BDI	1	1	1	\mathbb{Z}	0	0	0	\mathbb{Z}	0	\mathbb{Z}_2	\mathbb{Z}_2
D	0	1	0	\mathbb{Z}_2	\mathbb{Z}	0	0	0	\mathbb{Z}	0	\mathbb{Z}_2
DIII	-1	1	1	\mathbb{Z}_2	\mathbb{Z}_2	\mathbb{Z}	0	0	0	\mathbb{Z}	0
AII	-1	0	0	0	\mathbb{Z}_2	\mathbb{Z}_2	\mathbb{Z}	0	0	0	\mathbb{Z}
CII	-1	-1	1	\mathbb{Z}	0	\mathbb{Z}_2	\mathbb{Z}_2	\mathbb{Z}	0	0	0
C	0	-1	0	0	\mathbb{Z}	0	\mathbb{Z}_2	\mathbb{Z}_2	\mathbb{Z}	0	0
CI	1	-1	1	0	0	\mathbb{Z}	0	\mathbb{Z}_2	\mathbb{Z}_2	\mathbb{Z}	0

Table 1.1: *Considering time reversal symmetry Θ , charge conjugation symmetry Ξ and chiral symmetry $\Pi = \Xi\Theta$, one can discern ten so-called Altland-Zirnbauer classes [46]. The absence of these symmetries is indicated with 0, whereas the presence of a symmetry is denoted with the value that the associated operator squares to. For each class the defining topological invariant is enlisted. Particular examples include the \mathbb{Z} invariant describing the (anomalous) IQHE ($A, d = 2$) and the \mathbb{Z}_2 invariants pertaining to the \mathbb{Z}_2 topological band insulators ($AII, d=2, 3$).*

1.2 Topics of this thesis

This thesis rests on two intricately related subjects. The first revolves around the fundamental question whether time reversal symmetry fully characterizes the \mathbb{Z}_2 topological band insulator. Exemplifying a symmetry protected topological (SPT) state, the introduction of additional symmetries can generally be expected to yield new insights. In particular, one *should* contemplate the role of the underlying lattice symmetries, as the existence of Bloch states necessitates the breaking of translational symmetry to a dis-

crete subgroup. These underlying crystal symmetries are adequately addressed in the mathematical language of space groups and we will demonstrate that the notion of space group symmetries can indeed be incorporated in the characterization of \mathbb{Z}_2 topological band insulators. Moreover, we will elucidate the physical consequences of the resulting space group classification by examining its interplay with defects, which entails the major theme of this thesis.

Of central interest in this venture is the prominent role of crystal dislocations, being point-like objects in two dimensions and lines in three spatial dimensions. A dislocation (Fig. 1.4) can effectively be understood following the Volterra process. In this construction the lattice imperfection is apprehended as a relative mismatch in the arrangement of the crystal. Specifically, the misalignment is attained by cutting the perfect crystal along an imaginary plane and then gluing back the pieces with a twist or translation such that away from the resultant defect core, arising at the end of the imaginary plane, the two pieces are coordinated. The resulting defining property is that *any* loop drawn around the defect core suffers a discontinuity and corresponds to a purely translational (rotational) defect in case of a dislocation (disclination). Consequently, disclinations and dislocations exhaust the elementary possible topological lattice defects [56, 57].

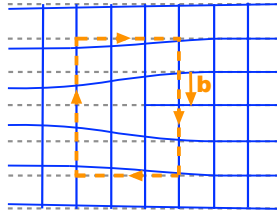


Figure 1.4: *Dislocation in a square lattice. The original lattice is indicated with dashed lines. The extra row of atoms results in a non-closure of any loop drawn around the defect in the new lattice as quantified by the Burgers vector \mathbf{b} .*

The non-closure of a original loop of the undistorted lattice by a lattice vector, the Burgers vector, can be shown to correspond to an induced torsion in the effective Riemann-Cartan geometrical description of the lattice [57, 58, 59, 60]. Of topical interest, however, are the ramifications for the associated electronic states. As the non-closure property prevails for arbitrary sizes of the loop, the effect of a dislocation can adequately be captured by imposing nontrivial boundary conditions on the wave functions encircling the defect. In particular, the low energy effective Dirac fermion theories,

encountered in previous section, are resultantly augmented by a $U(1)$ gauge field due to the Aharonov-Bohm analysis [61], which is in this sense deeply rooted in the underlying topological description [25]. That is, the action on the wave functions is that of a $U(1)$ Berry holonomy, being the same phase that lies at the heart of the first Chern number.

The fact that dislocations are the unique generalized "flux" probes corresponding with the translational symmetry breaking of the lattice heuristically accounts for the intimate connection to the space group classification. Nonetheless, the study of defects in symmetry protected topological phases harbors interesting physics also in its own right. Indeed, monodromy defects that twist boundary conditions by a symmetry transformation along cuts in SPT phases, are directly linked to intriguing subjects of nontrivial braiding statistics and fractionalized quantum numbers [62, 63]. A particular consequential example is that of Majorana zero-modes bound to such kind of defects in topological superconductors, which represent promising candidates for practical implementation of these concepts in the form of topological quantum computation [64, 65, 66, 67]. We will uncover that in the case of \mathbb{Z}_2 topological band insulators reminiscent physics is at work, culminating in the formation of mid-gap states that also feature fractionalized quantum numbers. These modes subsequently form the building blocks of various physical relevant scenarios of which we will detail the underlying mechanisms.

Finally, we also mobilize the obtained physical insights by considering arrays of dislocations as can be realized in grain boundaries, being interfaces of misaligned pieces of crystal due to an angular mismatch. Most importantly, we will demonstrate that such grain boundaries in specific types of topological insulators host Weyl semi-metallic states, which can be regarded as generalized isospinless realizations of graphene, exhibiting exciting distinct physical features. This then closes in some sense the circle as the simple graphene model played such a major role in development of the concept of the topological insulator.

1.3 This thesis

The rest of this thesis is organized in the following manner.

In Chapter 2, we further substantiate the introduced physical concepts from a phenomenological perspective. Specifically, we will detail the generic mechanism underlying topological insulators in the explicit setting of concrete models. These models will serve similar use in the reminder.

Subsequently, in Chapter 3, we introduce the universal observables that probe the non-trivial \mathbb{Z}_2 bulk topology of the quantum spin Hall phase; dislocations and π -fluxes. In particular, we analytically demonstrate that a π -flux vortex binds a *single* Kramers pair of mid gap modes, exponentially localized to the vortex core, in the quantum spin Hall phase. The formation of these modes directly hangs together with the nontrivial entity of the bulk and hence provides for an alternative classification route of characterizing the underlying \mathbb{Z}_2 topology. Moreover, we then set these results in further physical motion by considering the relation to dislocations. Namely, we uncover that dislocations result in a similar response, but only in specific \mathbb{Z}_2 topological insulators. In addition to physically signifying the π -flux results, this above all indicates the existence of a subclassification within the tenfold way.

We then formalize these ideas in Chapter 4, resulting in the space group classification of topological band insulators. As a central result, this general formulation demonstrates that in fact there are three broad classes of \mathbb{Z}_2 topological insulating states: (a) Γ states robust against general time-reversal invariant perturbations; (b) Translationally-active states protected from elastic scattering, but susceptible to topological crystalline disorder; (c) Valley or crystalline topological insulators sensitive to the effects of non-topological and crystalline disorder. Furthermore, as the crystalline symmetries distinguish the resulting phases within these classes, we show that these categories give in turn rise to 18 different two-dimensional, and, at least 70 three-dimensional TBIs. Lastly, as a sidestep, these notions are also corroborated from a complementary viewpoint. That is, we show that a non-trivial bulk gives rise to zeros in the Green's function structure associated with codimension-1 and codimension-2 surfaces, the results of which in the former case then directly relate to the space group classification.

Accordingly, in Chapter 5, we revert to the remaining physical responses signifying the space group classification and address the criteria governing the formation of propagating dislocation-line modes in $3 + 1$ dimensional \mathbb{Z}_2 topological band insulators. Most

interestingly, the obtained $\mathbf{K}\text{-}\mathbf{b}\text{-}\mathbf{t}$ rule then directly reconfirms the introduced classification framework from a complementary point of view, unveiling that the exact existence conditions in fact arise by virtue of a rather intricate interplay between the lattice topology, represented by dislocation lines having orientation direction \mathbf{t} and Burgers vector \mathbf{b} , and the electronic-band topology, characterized by the band-inversion momenta \mathbf{K}_{inv} . As a striking implication, these general principles moreover identify that, in certain specified scenarios, this conspiracy culminates in the formation of directionally independent topologically-protected metallic states, that bind to arbitrarily orientable dislocation defects. These findings are evidently experimentally consequential, as dislocation defects are ubiquitous in any crystal hosting a topological insulating state.

Finally, in Chapter 6, we exemplify the physical content of the obtained insights by demonstrating that regular arrays of the outlined dislocation modes, which can be realized in the form of extended defects such as grain boundaries, naturally host time reversal symmetric semi-metals akin to graphene. Nonetheless, by virtue of the deep rooting of their emergence in the topology of the parent \mathbb{Z}_2 topological insulator, these states in fact do not require any fine-tuning, thereby providing for a novel and experimentally viable route towards topological semi-metals. In further analogy to the familiar edge states, these grain boundary spinon metals also exhibit distinct response features upon the introduction of externally applied electromagnetic fields. In particular, the $1 + 1$ dimensional variant is characterized by a parity anomaly per spin component resulting in a valley anomaly for the total system, whereas the $2 + 1$ dimensional realization displays an odd-integer quantum Hall effect. Given the generality of these results, we therefore anticipate that the sketched perspective on topological insulating states may find additional bearing in the form of unexplored states of matter appearing generically in translationally active topological insulators.

1.A Adiabatic curvature and Chern numbers

This Appendix reviews some of the topological concepts introduced in the above physical setting following Ref. [25].

Adiabatic curvature

The first concept we need is that of adiabatic curvature or Berry curvature resulting from a connection [68]. Berry noticed that the phase acquired due to adiabatic evolution of the wave functions in fact has a relation with geometry; the angular mismatch can be thought of as a result of local intrinsic curvature.

To make this concrete, consider a Hilbert space parameterized by $\mathbf{R} = R^\mu$, $\mu = 1 \dots M$, with corresponding Hamiltonian and normalized eigenfunctions

$$H(\mathbf{R})|m(\mathbf{R})\rangle = \varepsilon_m(\mathbf{R})|m(\mathbf{R})\rangle. \quad (1.9)$$

The associated connection can subsequently be evaluated in the usual way by considering eigenstates at two infinitesimally close points and defining

$$\exp(iA_m^\mu(\delta R_\mu)) = \frac{\langle m(\mathbf{R})|m(\mathbf{R} + \delta \mathbf{R})\rangle}{|\langle m(\mathbf{R})|m(\mathbf{R} + \delta \mathbf{R})\rangle|}, \quad (1.10)$$

which is expanded to first order. Canceling δR_μ on both sides and using the normalization condition of the wave function, this procedure then directly results in the well-known Berry connection

$$iA_m^\mu = \langle m(\mathbf{R}) | \frac{\partial m(\mathbf{R})}{\partial R_\mu} \rangle. \quad (1.11)$$

Accordingly, one can easily calculate the accumulated phase upon completing a closed contour \mathcal{C} in the parameter space, resulting in the so-called Berry phase

$$\exp(i \oint_{\mathcal{C}} A_m^\mu dR_\mu). \quad (1.12)$$

We note, however, that the eigenstates $|m(\mathbf{R})\rangle$ are only defined up to a phase factor, i.e they are representatives of a ray. Hence, we should take into account the local $U(1)$ gauge freedom

$$|m(\mathbf{R})\rangle \longrightarrow \exp(i\phi_m(\mathbf{R})) \quad A_m^\mu(\mathbf{R}) \longrightarrow A_m^\mu(\mathbf{R}) + \frac{\partial \phi_m(\mathbf{R})}{\partial R_\mu}, \quad (1.13)$$

conveying an evident relation with electrodynamics. This correspondence can be made even more explicit by rewriting equation (1.12), using the theorem of Stokes, as

$$\exp(i \oint_{\mathcal{C}} A_m^\mu dR_\mu) = \exp(i \int_{\mathcal{A}} dR_\mu \wedge dR_\nu f_m^{\mu\nu}(\mathbf{R})) \quad \partial \mathcal{A} = \mathcal{C}, \quad (1.14)$$

where

$$f_m^{\mu\nu}(\mathbf{R}) = \frac{\partial A_m^\nu(\mathbf{R})}{\partial R_\mu} - \frac{\partial A_m^\mu(\mathbf{R})}{\partial R_\nu} \quad (1.15)$$

is the gauge field tensor, known as the Berry curvature.

Interplay with topology

In order to understand the interplay with topology, it is useful to consider the Gauss-Bonnet theorem which relates the geometry of surfaces to topology. Concretely, it states that

$$\int_M K dA = 2\pi\chi(M),$$

where M is a manifold without boundary, K is the local curvature and $\chi(M)$ is the Euler characteristic. Here, $\chi(M)$ equates to $2 - 2g$, with g the genus which essentially counts the number of 'handles'. The right hand side is manifestly quantized and topological in the sense of the manifold. Therefore this can be viewed as a topological index theorem.

It turns out that the Gauss-Bonnet theorem is indeed a particular instance of a broader framework that connects specific topological invariants to specific classes of vector bundles. Specifically, Chern generalized the Gauss-Bonnet theorem by looking at so-called Chern classes of vector bundles of smooth manifolds. These characteristic classes are associated with topological invariants called Chern characters or Chern numbers [25] and essentially imply that the integral of the Berry curvature (the first Chern class) over a surface without a boundary yields an integer. Heuristically speaking, in the case of the Gauss-Bonnet theorem one integrates the local curvature and the underlying mathematical characterization can be viewed as an elementary example of a fibre bundle (tangent bundle). Namely, one can assign a total structure that regards each point as the local product of two manifolds, being the base manifold and the tangent space. Subsequent generalization of the tangent space then allows for the definition of general fibre bundles, or vector bundles when restricted to vector spaces, over the base manifold. These fibre bundles can similarly be equipped with a connection and in case of a complex vector bundle, the corresponding curvature then results in the well-known Chern invariant that measures the topological twisting of the bundles when local pieces are patched together globally.

Concretely, in case of the parameter space in equation (1.9) entailing the two dimensional reciprocal space of a translationally invariant crystal, the above thus results

in

$$\int_{BZ} f_m^{xy}(\mathbf{k}) dk_x dk_y = 2\pi \mathcal{C}_m^1, \quad (1.16)$$

where the integral is over the first Brillouin zone and \mathcal{C}_m^1 is the first Chern character. This essentially pertains to the winding number of the Berry phase, picked up by a state when it completes the contour in the Brillouin zone.

Second Chern number

The first Chern character associated with the Abelian field strength (1.15) manifests itself physically as the quantized Hall conductance. However, higher Chern classes produce similar invariants and, as will be shown below, especially the second Chern invariant actually pertains to an analogous physical interpretation. Let us therefore conclude by explicit evaluation of the second Chern number in the concrete setting of band models. In this case the non-Abelian phase gauge field $f_{ij}^{\alpha\beta}$ and resulting second Chern number \mathcal{C}^2 take the simple form

$$f_{ij}^{\alpha\beta} = \partial_i a_j^{\alpha\beta} - \partial_j a_i^{\alpha\beta} + i[a_i, a_j]^{\alpha\beta}, \quad (1.17)$$

$$a_i^{\alpha\beta} = -i \langle \alpha, \mathbf{k} | \frac{\partial}{\partial k_i} | \beta, \mathbf{k} \rangle, \quad (1.18)$$

$$\mathcal{C}^2 = \frac{1}{32\pi^2} \int d^4 k \epsilon^{ijkl} \text{Tr}[f_{ij} f_{kl}], \quad (1.19)$$

with $i, j = 1, 2, 3, 4$ and α, β denoting the filled bands. This form finds direct use in $4+1$ dimensions [69] in models of the type

$$H(\mathbf{k}) = d^a \gamma_a \quad d^a = (M + c \sum_i \cos(k_i), \sin(k_x), \sin(k_y), \sin(k_z), \sin(k_w)), \quad (1.20)$$

where the γ -matrices obey the Clifford algebra and i refers to the four momenta. Indeed, in the case of two filled bands one can define a $SU(2) \times U(1)$ connection and the Chern character can be expressed as

$$\mathcal{C}^2 = \frac{3}{8\pi^2} \int d^4 k \epsilon^{abcde} \hat{d}_a \frac{\partial}{\partial k_x} \hat{d}_b \frac{\partial}{\partial k_y} \hat{d}_c \frac{\partial}{\partial k_z} \hat{d}_d \frac{\partial}{\partial k_w} \hat{d}_e \quad (1.21)$$

in terms of the five-component vector $\hat{d}_a(\mathbf{k}) = d_a(\mathbf{k})/|d(\mathbf{k})|$. This second Chern number then directly sets the coefficients of the nonlinear response, just as the first Chern character sets the coefficient of the linear response term in the $2+1$ dimensional quantum Hall effect, and thereby reconfirms the physical significance of the Chern invariants.

Chapter 2

Phenomenology of topological band insulators

In this Chapter we highlight the concepts underlying topological insulating states from a phenomenological point of view and introduce some of the models that will be of use in the subsequent parts. This will entail a bulk and a complementing edge state perspective.

2.1 Bulk perspective

2.1.1 Anomalous quantum Hall and quantum spin Hall models

The conceptual treatment presented in the previous Chapter already indicated the intricate relation between topological band theory and the fermion doubling theorem [33, 34]. This can however be made more explicit by considering the simple lattice regularized Hamiltonian

$$H(k_x, k_y) = A \sin(k_x) \tau_x + A \sin(k_y) \tau_y + [M - 2B(2 - \cos(k_x) - \cos(k_y))] \tau_z, \quad (2.1)$$

in terms of the Pauli matrices τ , natural units and model parameters A , B and M [70]. Furthermore, we have adopted the convention to trivially suppress the creation and annihilation operators for such Hamiltonians in momentum space. A crucial observation regarding the above Hamiltonian then pertains to the fact that the mass term can change sign throughout the Brillouin zone as function of the parameter M/B , revealing the defining property that lies at heart of the nonzero Hall conduction of the model. This is particularly easily motivated by expanding Eq. (2.1) around the momenta $(0, 0)$, $(\pi, 0)$, $(0, \pi)$ and (π, π) and examining the response to an electromagnetic $U(1)$ gauge potential A_μ .

Switching to Lagrangian formalism it is evident that such a procedure results in four two-component Dirac or Weyl equations of the type

$$\mathcal{L} = \bar{\Psi}(i\gamma^\mu \partial_\mu - \gamma^\mu A_\mu - \hat{M})\Psi, \quad (2.2)$$

where $\bar{\Psi} = \Psi^\dagger \tau^z$, $\gamma^0 = \tau^z$, $\gamma^1 = i\tau^y$, $\gamma^2 = -i\tau^x$, and the relative signs as well as the mass terms \hat{M} depend on the specific momentum points. Correspondingly, obtaining the associated polarization tensor $\Pi_{\mu\nu}$ from the current-current correlation function encompasses a standard result [71, 72] and renders, in addition to the Maxwell part, the well-known topological Chern-Simons term [73]

$$S_{SC} \sim \mathcal{C}^1 \int dx dy \int dt \varepsilon^{\mu\nu\rho} A_\mu \partial_\nu A_\rho \quad \mu, \nu, \rho \in \{0, 1, 2\}. \quad (2.3)$$

The result (2.3) for the Lagrangian (2.2) then finds a natural physical understanding by virtue of the assumed lattice regularization. Indeed, the $(0,0)$ and (π, π) flavors contribute a Hall conductivity $\sigma_{xy} = \mathcal{C}^1 = \text{sign}(\hat{M})$, whereas the other two points contribute $\sigma_{xy} = -\text{sign}(\hat{M})$ in units of $\frac{e^2}{2h}$. Hence, we observe the direct significance of the role of the mass term by simply summing the Hall conductivities. Namely, only when the mass term attains different signs at the different momenta, the *total* Hall conductivity can acquire a nonzero value and the presence of the Chern-Simons term is assured. Since this term breaks the parity invariance $\tau_x H(k_x, -k_y) \tau_x = H(k_x, k_y)$ per fermion flavor even in the parity invariant limit $m \rightarrow 0$, the presence of the Chern-Simons term for the total system is somewhat more commonly referred to as a parity anomaly. The appearance of this anomaly consequently discloses the essential feature underlying the anomalous Hall effect and we note that, apart from subtleties such as the different symmetries of the free graphene model and its number of Dirac flavors, the Haldane model [27] relates to the exact same mechanism.

Accordingly, these considerations can be verified by explicit calculation of the first Chern number (Appendix 1.A) of the associated complex bundle. This procedure reduces for a model of the form

$$H(k_x, k_y) = \mathbf{d}(\mathbf{k}) \cdot \boldsymbol{\tau}, \quad (2.4)$$

to the particular simple expression

$$\mathcal{C}^1 = \frac{1}{4\pi} \int dk_x dk_y \varepsilon^{abc} \hat{\mathbf{d}}_a \frac{\partial \hat{\mathbf{d}}_b}{\partial k_x} \frac{\partial \hat{\mathbf{d}}_c}{\partial k_y}, \quad (2.5)$$

in terms of the unit vector $\hat{\mathbf{d}}$. We notice that in this case the quantization is rather manifest; the integrand is nothing but the Jacobian of a mapping of the map $\hat{\mathbf{d}}(\mathbf{k}) : T^2 \rightarrow S^2$. Hence, integration results in the image of the Brillouin zone on the two sphere, which is a topological (Pontryagin) winding number of quantized value $4\pi\nu$, $\nu \in \mathbb{Z}$. Explicit evaluation of the Hamiltonian (2.1) then shows that indeed

$$\mathcal{C}^1 = \begin{cases} 0, & 0 > \frac{m}{B} \text{ or } \frac{m}{B} > 8 \\ 1, & 0 < \frac{m}{B} < 4 \\ -1, & 4 < \frac{m}{B} < 8 \end{cases}, \quad (2.6)$$

conforming the above continuum results.

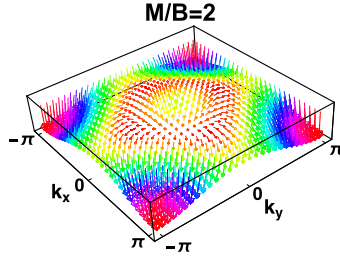


Figure 2.1: A particular illustrative way to visualize the topological non-trivial phases of the Hamiltonian (2.1) is by plotting the vector field $\hat{\mathbf{d}}(\mathbf{k})$ over the Brillouin zone. This reveals a skyrmion centered around $\mathbf{k} = 0$ for $0 < M/B < 4$, whereas the skyrmion is centered around $\mathbf{k} = (\pi, \pi)$ for $4 < M/B < 8$.

The relation between the anomalous quantum Hall effect and the quantum spin Hall effect, as illustrated in the previous Chapter with the Haldane and Kane-Mele model [31, 32], can subsequently be exploited to define an analogous model exhibiting a \mathbb{Z}_2 topological phase. Combining two time reversed copies of Eq.(2.1), the Hamiltonian attains the form

$$\mathcal{H}(k_x, k_y) = \begin{pmatrix} H(\mathbf{k}) & 0 \\ 0 & H^*(-\mathbf{k}) \end{pmatrix} = A \sin(k_x) \gamma_x + A \sin(k_y) \gamma_y + M(\mathbf{k}) \gamma_0, \quad (2.7)$$

with $M(\mathbf{k}) = M - 2B(2 - \cos(k_x) - \cos(k_y))$, $\gamma^0 = \tau_z \otimes \sigma_0$, $\gamma^1 = \tau_x \otimes \sigma_z$, $\gamma^2 = \tau_y \otimes \sigma_0$ and the Pauli spin matrices σ acting in the spin space. As the spin Hall conductivity $\sigma_{xy}^s = (\sigma_{xy}^\uparrow - \sigma_{xy}^\downarrow)$, a \mathbb{Z}_2 topological phase is expected for $0 < M/B < 4$ and $4 < M/B < 8$. This simple argumentation can be shown to be profound. Specifically, the \mathbb{Z}_2 invariant

ν is explicitly given by $(-1)^\nu = \prod_{\Gamma_i} \text{sign}(M(\Gamma_i))$, in terms of the time reversal invariant (TRI) momenta Γ_i comprising $(0,0)$, $(\pi,0)$, $(0,\pi)$ and (π,π) [38], verifying the \mathbb{Z}_2 topological entity of the above parameter regimes also in the presence of $\langle S_z \rangle$ breaking perturbations that do not close the gap. As a matter of fact, the above simple model pertains to the effective description introduced by Bernevig, Hughes and Zhang [40] used to describe the actual experimental viable realization of the quantum spin Hall effect in CdTe/HgTe/CdTe quantum wells [41] and finds its origin in the same regularization considerations as above.

2.1.2 Three dimensional \mathbb{Z}_2 topological band insulators

The generic form of the $2+1$ dimensional Hamiltonian (2.7) can readily be generalized to three spatial dimensions, resulting in

$$\mathcal{H}(k_x, k_y, k_z) = A_1 \sin(k_x) \gamma_x + A_1 \sin(k_y) \gamma_y + A_2 \sin(k_z) \gamma_z + M(\mathbf{k}) \gamma_0. \quad (2.8)$$

Where in the above, it is assumed that the above Dirac matrices γ satisfy the Clifford algebra and are odd (even) under time reversal for the odd (even) momentum terms. As in the two dimensional case, the topological properties are determined by the momentum depended mass term. Taking $M(\mathbf{k}) = M - 2B(3 - \cos(k_x) - \cos(k_y) - \cos(k_z))$, for example, calculation of the \mathbb{Z}_2 invariant still amounts to multiplying the signs of the mass terms at the TRI points, which in this case constitute the vertices of the first octant of the cubic Brillouin zone, and confirms the existence of the non-trivial phases for the gapped parameter regimes $0 < M/B < 4$, $4 < M/B < 8$ and $4 < M/B < 12$. Strikingly, the simple model (2.8) also meets its lower dimensional counterpart in terms of application to physical systems, as its form encompasses the lattice regularized version of the effective continuum description of the topological phases in the second generation Bi_2Se_3 family of materials [43, 44, 45].

2.1.3 Field theories of \mathbb{Z}_2 topological band insulators

Although the outlined mechanism can directly be employed to construct the above models of \mathbb{Z}_2 topological band insulators, an elegant reminiscent procedure provides for a route of also addressing the effective field theory [69]. This description is rooted in the generalization of the $2+1$ dimensional integer quantum Hall effect (IQHE) to a $4+1$ dimensional time reversal invariant analogue [74, 75], the origin of which can actually

be understood from a geometrical argument [76] that is closely related to the Hopf maps [77]. Specifically, the $2 + 1$ dimensional IQHE can be apprehended by mapping the problem to the two-sphere S^2 , with a Dirac monopole at its center [78]. Topological non-trivial configurations then arise as the $U(1)$ gauge potentials extending from the North and South pole are matched non-trivially at the equator, which is in fact possible due to the natural isomorphism between the circle S^1 and the gauge group $U(1)$. This geometrical coincidence occurs similarly in the case of the four-sphere S^4 , where the equator S^3 is isomorphic to the gauge group $SU(2)$ and, on a heuristic level, the IQHE in four spatial dimensions can effectively be regarded as the $SU(2)$ variant of the familiar $2 + 1$ dimensional quantum Hall effect.

Correspondingly, the above analysis concerning the $2 + 1$ dimensional IQHE can directly be translated. In particular, Eq. (2.3) finds its generalization in

$$S_{cs} \sim \mathcal{C}^2 \int d^4x \int dt \epsilon^{\mu\nu\rho\sigma\tau} A_\mu \partial_\nu A_\rho \partial_\sigma A_\tau \quad \mu, \nu, \rho, \sigma, \tau \in \{0, 1, 2, 3, 4\}. \quad (2.9)$$

Here, the second Chern Chern number \mathcal{C}^2 , associated with the non-Abelian Berry's phase field, plays the exact same role as the the first Chern character (Appendix 1.A), arising similarly in the context of the electromagnetic response of models of the type as in Equations (2.7) and (2.8). More importantly, the $4 + 1$ dimensional Chern-term can subsequently be subjected to a fundamental procedure known as dimensional reduction, resulting in the effective response theory governing $(2+1)$ and $(3+1)$ dimensional \mathbb{Z}_2 topological band insulators. Basically, retaining momentum in one direction results in a parameter family of dimensionally reduced Hamiltonians, which are connected due to the von Neumann-Wigner theorem [79]. In this specific gauge, the reduced action then exactly reproduces the Laughlin argument. Indeed, the momentum gets shifted by the gauge field and defines a periodic interpolation parameter $\theta(x, t)$, which is directly related to the charge polarization $P[\theta(x, t)]$ during such a cycle [20, 21]. Resultantly, the effective action can be written as

$$S_{3D} = \frac{1}{4\pi} \int d^3x \int dt \epsilon^{\mu\nu\sigma\tau} P[\theta(x, t)] \partial_\mu A_\nu \partial_\sigma A_\tau \quad \mu, \nu, \sigma, \tau = \{0, 1, 2, 3\}. \quad (2.10)$$

Time reversal symmetry then dictates that the difference in second Chern character of any two continuous interpolations (Laughlin cycles) associated with such descended Hamiltonians is even and hence defines two different classes, characterized by the parity of the second Chern number [69]. This is in direct accordance with the underlying \mathbb{Z}_2 classification. In fact, time reversal invariance actually constraints the value of P

to a constant, characterizing the topological and trivial insulating classes by $P = 0, \frac{1}{2}$, respectively. Finally, its presence also allows for a similar topological distinction for the reminiscent $2 + 1$ dimensional response theory, as can be obtained by utilizing the extra possible reduction step.

The action (2.10) finds a direct physical motive, as it provides for the condensed matter realization of the axion Lagrangian or θ -vacuum, familiar in the context of quantum chromodynamics [80, 81], with θ playing the role of the axion field. Essentially, the surface between the topological vacuum and the trivial vacuum provides for an axion domain wall structure, as detailed in the next section. Moreover, as the θ -term couples the magnetic and electric field, a magnetic field then induces a charge polarization, resulting in the so-called topological magneto-electric effect (TME). As a result, \mathbb{Z}_2 topological insulators thus also provide for a physical setting in which these exotic field theories might find an application [82], possibly culminating in striking features such as for example dyons and the Witten effect [69, 83].

2.2 Edge state perspective

We conclude this introductory part by accentuating the above notions from the perspective of the edge states, being the very signature of topological band structures. Specifically, this perspective motivates the manifestation of the underlying concept of anomalies in Dirac field theories and their relation to nontrivial states of free fermion matter directly in the context of domain walls. This basic mechanism finds its conceptual origin in the rather surprising context of the $1 + 1$ dimensional effective field theory of polyacetylene. Hence, we will first step back a dimension to revisit the well-known Su-Schrieffer-Heeger model.

2.2.1 Jackiw-Rebbi solitons in the Su-Schrieffer-Heeger model

The Su-Schrieffer-Heeger (SSH) model [84, 85, 86], introduced as an effective description of the conducting polymer polyacetylene, turns out to host all the necessary ingredients for the rich concepts of fermion number fractionalization and domain wall states [87, 88]. Consider a ring of (trans)polyacetylene consisting of N monomers of mass M (Figure 2.2). Assuming that the relevant degree of freedom is the displacement u of the monomers, a Peierls tight-binding model including electron-phonon coupling to

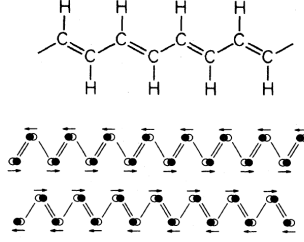


Figure 2.2: *Chemical notation of (trans) polyacetylene. The conducting polymer undergoes at half-filling a Peierls instability into a dimerized state. Nonetheless, there are two topologically distinct vacua, which resultantly allow for interpolating domain wall configurations.*

the lowest order is readily obtained [86]. A calculation, resembling the mean-field theory of conventional superconductivity and its quasiparticle spectrum [89], then shows that at half-filling the system subsequently has two separate dimerized ground state configurations, associated with spontaneous symmetry breaking (Figure 2.2). Moreover, similar to 1 + 1 dimensional sine-Gordon theory or ϕ^4 theory, the system subsequently allows for soliton configurations interpolating between this so-called A phase and B phase; introducing an order parameter

$$\phi_j = (-1)^j u_j, \quad (2.11)$$

taking values $\langle \phi_j \rangle = \pm \eta$ in the A/B phase, numerical calculations [84, 85] show that there is a phonon field configuration $\phi_j \approx \eta \tanh((j - j_0)/\xi)$ approaching the A (B) phase when $j \rightarrow \pm\infty$.

Of topical interests are the consequences for the electronic states, the relevant physics of which can be addressed by expanding the bands around the Fermi energy. In particular, such an expansion results in two spin-degenerate linear dispersing branches (\pm), which are coupled by virtue of the dimerization wave number $2k_f$ (being a consequence of the doubling of the unit cell), and therefore results in the real space Hamiltonian

$$H(x) = \Psi(x)^\top (\tau_z(-i\partial_x) + \phi(x)\tau_x)\Psi(x), \quad (2.12)$$

with $\Psi(x) = (\psi(x)_+, \psi(x)_-)^\top$. Focussing on the soliton back ground configuration, it is easy to see that Eq. (2.12) admits a *single* normalizable "Jackiw-Rebbi" zero-

energy solution of the form $\Psi_0(x) \sim \phi_+ e^{-\int_0^x dx' m(x')}$ [90, 91], where $\tau_y \phi_{\pm} = \pm \phi_{\pm}$ and it is assumed that the mass profile exhibits a sign change from negative to positive at $x = 0$. The appearance of this zero energy state is in fact the epitome of the profound interplay of topology and Dirac fermionic states as formalized by the Atiyah-Singer index theorem [92, 93], which directly relates the number of zero-energy modes to the topological index of the elliptic differential operator (2.12).

The single domain wall mode subsequently leads to the notion of fractionalized quantum numbers as a result of the crucial presence of the apparent charge conjugation symmetry, generated by the anti-commuting τ_y matrix. Introducing a full Dirac sea, to assure that the spectrum is bounded from below, it is straightforward to calculate the density $\rho_s(E)$ of single-particle states in the presence of the soliton relative to the vacuum $\rho(E)$. Exploiting the completeness relation, the change in the charge of the ground state is found to be

$$Q = -\frac{1}{2} \int_0^{\infty} dE (\rho_s(E) - \rho_s(-E)), \quad (2.13)$$

revealing that due to the spectral symmetry only the zero modes contributes half a charge. More generally, one can show that for a traceless Hermitian operator Q , representing a constant of motion, the ground state average $\langle Q \rangle$ is given by

$$\langle Q \rangle = \frac{1}{2} \left(\sum_{\text{occupied}} \Psi_E^{\dagger} Q \Psi_E - \sum_{\text{unoccupied}} \Psi_E^{\dagger} Q \Psi_E \right), \quad (2.14)$$

where the sum has the interpretation of an integral when the spectrum is continuous and $\{\Psi_E\}$ is the complete set of eigenstates of the Hamiltonian with energy E . Taking into account the spin degeneracy and assuming that S_z is a good quantum number, this form immediately exposes the spin-charge separation. Namely, populating one of the modes leads to two types of spinons, having spin $S_z = \pm \frac{1}{2}$ but no net relative charge $Q = 0$, whereas unoccupied or doubly occupied configurations result in chargons or holons, characterized by $S_z = 0$ and $Q = \pm 1$. Physically, in the case of the polyacetylene ring, a soliton and anti-soliton are obviously created in pairs. The valence band experiences a depletion of one state for each pair and thus, by charge conjugation symmetry, the conduction band then also loses a total of one state. These states form two pairs located at mid gap when the solitons are separated by large distances as compared to the characteristic length.

Although it is evident that the SSH model exemplifies a 1 + 1 dimensional topological band insulator, where the role of protecting symmetry is now played by the charge

conjugation symmetry, we finally note that the connection to the above notions can be made even more explicit by obtaining the quantum numbers via an alternative approach. Basically, coupling the Dirac fermions to a slowly varying complex field that represents the soliton, the response is readily calculated using the Golstone-Wilczek formula [94]. This procedure then shows that response theory is of the same form as Eq. (2.10). Accordingly, the polarization can similarly be obtained from dimensionally reducing the $2 + 1$ dimensional quantum Hall effect, while imposing charge conjugation symmetry [69].

2.2.2 Two dimensional topological band insulators

The Jackiw-Rebbi solitons in the Su-Schrieffer-Heeger model provide for a particularly accessible illustration of the conceptual mechanism of the formation of zero-modes bound to domain walls. However, such constructions have been a subject of extensive study in field theory and find straightforward generalizations in higher dimensions in the form of the so-called Callan-Harvey effect [95]. This line of reasoning then directly provides for the effective description of the surface states, characterizing nontrivial band structures. In particular, it is straightforward to see that a Dirac Hamiltonian with a mass profile that changes sign from positive to negative at $x = 0$

$$H(x, k_y) = -i\tau_x \partial_x + k_y \tau_y + m(x) \tau_z, \quad (2.15)$$

has a normalizable domain wall solution of the form $\Psi_0(x) \sim \phi_+ e^{ik_y y} e^{-\int_0^x dx' m(x')}$, where $\tau_y \phi_\pm = \pm \phi_\pm$. This directly signifies the correspondence between the existence of spatially localized edge states and the topological characterization of the vacua on either sides of the interface $x = 0$, as signaled by the sign change of the mass. Moreover, these surface states have a definite chirality. Namely, as an actual system will have two edges, the non-normalizable solution, with an overall sign in the exponent, is also part of the spectrum and represents the normalizable solution at the *opposite* surface.

This general mechanism finds immediate application in the concrete setting of the anomalous Hall model (2.1). Breaking the translational invariance in Eq. (2.1) in one direction and solving the spectrum as function of the projected momentum k readily reveals the edge states. For $0 < M/B < 4$, the spectrum features two low-energy states that transverse the band gap forming a Dirac cone at $k = 0$, whereas for $4 < M/B < 8$ this cone is located at $k = \pi$ (Figure 2.3). These states can explicitly be shown to

be of the anticipated chiral nature in accordance with the Chern numbers (2.6). That is, for $0 < M/B < 4$ the surface states propagate clockwise along the perimeter of the system, while for $4 < M/B < 8$ the direction is reversed. More interestingly, the solitonic configuration of the mass for the specific value of k also exposes the manifestation of the anomaly at the edge. Focussing on one edge, the coefficient of response term (2.3) is set by the sum of the topological charges, being $\pm 1/2$ depending on the mass of each flavor. Across the interface the mass term changes sign inducing a similar anomalous term that cancels the bulk anomaly. This anomaly-cancellation argument lies at heart of the effective understanding of the integer as well as fractional quantum Hall effect [96], and in essence entails the Callan-Harvey effect [95].

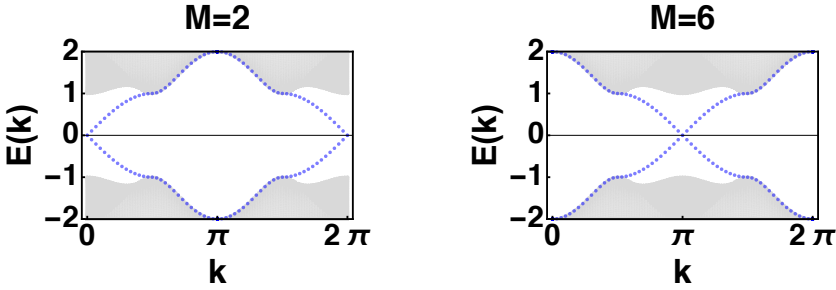


Figure 2.3: Spectra of Eq.(2.1) on a cylinder. Specifically, periodic boundary conditions were imposed in the \hat{y} -direction, whereas the \hat{x} -direction featured open boundary conditions. Due to the C_4 symmetry the result with the boundary conditions interchanged is equivalent. The edge states traverse the gap forming a Dirac cone. As the two states are localized to opposite surfaces, the total system features chiral edge states.

The translation to the spin Hall effect subsequently amounts to a routine procedure, exploiting the physical perspective. Specifically, in case of S_z conservation, each spin copy of the model (2.7) is characterized by one surface state culminating in a total system that features a pair of counter propagating helical or spin filtered edge states. Generally speaking, the usual Luttinger liquid theory [97, 98] describing the chiral edge states of a quantum Hall system is hence modified to

$$H(k) = \int \frac{dk}{2\pi} (\psi_{k,\uparrow} v k \psi_{k,\uparrow} - \psi_{k,\downarrow} v k \psi_{k,\downarrow}) + H_{\text{pert}}, \quad (2.16)$$

where v is the effective velocity. The edge state perspective directly exposes the crucial role of time reversal symmetry (TRS), as it prohibits backscattering terms opening a gap

in Eq. (2.16) for each individual edge. This then conveys the persistence of the edge states in more general scenarios that include spin-conservation breaking perturbation terms and signifies the bulk-boundary correspondence in a rather concrete manner.

2.2.3 Three dimensional \mathbb{Z}_2 topological band insulators

The protection mechanism based on the spatial separation of the surfaces and the resultant role of time reversal symmetry finds an immediate generalization to $3 + 1$ dimensions, providing for the edge state perspective on the existence of the three dimensional \mathbb{Z}_2 topological band insulator. Let us for concreteness derive the anticipated edge states explicitly in case of the above model (2.8) in a continuum setting. Expanding the model around $\mathbf{k} = 0$, the Hamiltonian attains the form

$$\mathcal{H}_{\text{eff}}(k_x, k_y, k_z) = A_2 k_x \gamma^1 + A_2 k_y \gamma^2 + A_1 k_z \gamma^3 + M(\mathbf{k}) \gamma^0, \quad (2.17)$$

where in analogy to [45] it is assumed that $M(\mathbf{k}) = M - B(k_x^2 + k_y^2 + k_z^2)$ and the Γ matrices are specified by $\gamma^0 = \tau_z \otimes \sigma_0$, $\gamma^1 = \tau_x \otimes \sigma_x$, $\gamma^2 = \tau_x \otimes \sigma_y$, $\gamma^3 = \tau_x \otimes \sigma_z$. Considering the Hamiltonian in a half-plane geometry for $z > 0$, it is readily verified that the defining equation for the anticipated $k_x, k_y = 0$ edge states

$$\mathcal{H}(0, 0, -i\partial_z) \Psi(z) = [-iA_1 \gamma^3 \partial_z + \gamma^0 (M + B\partial_z^2)] \Psi(z) = 0, \quad (2.18)$$

admits solutions of the form

$$\Psi_{\downarrow}(z) = \begin{pmatrix} 0 \\ \psi(z) \end{pmatrix} \quad \Psi_{\uparrow}(z) = \begin{pmatrix} \psi(z) \\ 0 \end{pmatrix}. \quad (2.19)$$

Specifically, the full solution for $\psi(z)$ is given by

$$\psi_0(z) = (\alpha e^{\lambda_+ z} + \beta e^{\lambda_- z}) \phi_+ + (\zeta e^{\lambda_+ z} + \eta e^{\lambda_- z}) \phi_-, \quad \alpha, \beta, \zeta, \eta \in \mathbb{C}, \quad (2.20)$$

where $\lambda_{\pm} = \frac{-A_1 \pm \sqrt{4MB + A_1^2}}{2B}$ and $\tau_y \phi_{\pm} = \pm \phi_{\pm}$. Crucially, the normalization condition $\text{Re}[\lambda_{\pm}] < 0$ (taking $\eta, \zeta = 0$) or $\text{Re}[\lambda_{\pm}] > 0$ (taking $\alpha, \beta = 0$) can only be satisfied when the band inversion condition $MB > 0$ is met. This criterium is again in direct correspondence with the nontrivial characterization of Eq. (2.17). That is, for $MB > 0$ the continuum description is in the inverted regime and associated with the topological phase, whereas for $MB < 0$ the system is in the trivial regime [45].

Finally, the obtained surface states can also be exploited to project the Hamiltonian onto the subspace spanned by $|\Psi_\uparrow(z)\rangle$ and $|\Psi_\downarrow(z)\rangle$, resulting in a surface Hamiltonian that yet another time illustrates the general principles. Concretely, the result in leading order in \mathbf{k} is

$$\mathcal{H}_{\text{surface}}(k_x, k_y) = \begin{pmatrix} 0 & A_2(k_x - ik_y) \\ A_2(k_x + ik_y) & 0 \end{pmatrix} \quad (2.21)$$

and provides for an adequate description of the experimentally observed edge states in the second generation materials, such as for example Bi_2Se_3 [43, 44]. Coupling the system to a magnetic field $\mathbf{B} = B\mathbf{e}_z$ then reveals the manifestation of the Callan-Harvey mechanism. Taking the specific gauge $A_z = 0$, the Hamiltonian (2.21) becomes

$$\mathcal{H}(k_x, k_y) = \sigma_x(k_x + A_x) + \sigma_y(k_y + A_y) - gB\sigma_z, \quad (2.22)$$

where the Zeeman term now acts as the effective mass. Consequently, the relativistic Landau levels come in the standard form

$$\epsilon_{n,\sigma_3} = \pm[(2n+1)B - \sigma_3 B + (gB)^2]^{\frac{1}{2}} \quad n = 0, 1, 2, 3, \dots, \quad \sigma_3 = \pm 1. \quad (2.23)$$

The symmetry of the spectrum in conjunction with the fact that $\epsilon_{0,1}$ only carries half of the degeneracy of the other levels explicitly indicates the relation with the above solitons, showing that the surface similarly accumulates charge and spin. More interestingly, as gB acts the effective mass a familiar consideration shows that, in case of two opposite surfaces, the two edges of the system feature an opposite Hall conductivity $\sigma_{xy} = \frac{1}{2}\text{sign}(gB)$, in units of e^2/h . Hence, the total response term including both surfaces can be written as

$$S_{\text{eff}} = \frac{1}{4\pi} \left[\int_{S_1} dx dy \int dt \epsilon^{\mu\nu\rho} A_\mu \partial_\nu A_\rho - \int_{S_2} dx dy \int dt \epsilon^{\mu\nu\rho} A_\mu \partial_\nu A_\rho \right], \quad (2.24)$$

where we have reverted to natural units ($\hbar = e = c = 1$), $\mu, \nu, \rho \in \{0, 1, 2\}$ and S_1, S_2 denote the two relevant surfaces. Expressing Eq. (2.24) as a volume integral then explicitly demonstrates the bulk-boundary correspondence. Specifically, the θ -term (2.10)

$$S_{3D} = \frac{1}{4\pi} \int d^3x \int dt \epsilon^{\mu\nu\sigma\tau} \theta \partial_\mu A_\nu \partial_\sigma A_\tau \quad (2.25)$$

with $\theta = \frac{1}{2}$ is clearly a total derivative and integrates to the above boundary theory, reconfirming the intricate relation between the topological bulk characterization and its manifestation on the edge. That is, on the closed manifold the response is governed

by the action (2.10) and the polarization P only takes the distinguishable time reversal invariant values 0 or $\frac{1}{2}$, as the additional integer part is associated with gauge transformations and does not represent a physical quantity [69]. Correspondingly, in the case of a system with open boundaries, the domain wall structure of the polarization is in direct accordance with this topological term and resultantly physically signifies the topological distinction of the two vacua on either side of the boundary.

Chapter 3

Universal bulk probes of the \mathbb{Z}_2 topological insulator

The salient physical feature of \mathbb{Z}_2 topological band insulators (TBI) is that they are fully gapped in the bulk while possessing gapless propagating modes protected by time reversal symmetry (TRS) on their boundary. Although the presence of TRS ultimately underlies the topological description, it nonetheless constraints, fundamentally and especially experimentally, the availability of robust probes of this bulk-boundary correspondence or anomalous responses. In particular, for $2 + 1$ dimensional TBIs the charge Hall response vanishes, and instead a much more involved TRS invariant quantum spin Hall (QSH) effect characterizes the topological phase. It has been shown, however, through numerical studies that a π -flux vortex, which actually preserves TRS, can play the role of a \mathbb{Z}_2 bulk-probe in a QSH insulator through the appearance of topologically protected mid-gap modes. [99, 100, 101, 102]

In this Chapter, we introduce the π -flux vortex as the bulk probe of the 2+1 dimensional \mathbb{Z}_2 topological band insulator and show that such a vortex binds a single Kramers pair of modes. Specifically, we analytically study the formation of these mid-gap states and show that their existence is intimately related to the non-trivial background. This analysis reveals that such vortices resultantly indicate an alternative classification route for the non-trivial characterization of the QSH phase. Most interestingly, we then bring these results to life by linking them to response of dislocations. Namely, dislocations are shown to provide for an effective π -flux problem, but only in specific \mathbb{Z}_2 topological insulating phases. This latter condition is physically relevant as this distinction turns

out to be intricately tied to the lattice topology and ultimately implies the existence of additional classification beyond the ten fold way. Finally, we corroborate these results with numerical calculations, which confirm the anticipated robustness of these modes.

The general way by which we achieve these results is by employing the $M - B$ model (2.7), initially constructed to describe the HgTe quantum well QSH insulator [40, 41]. The striking and universal feature of the low-energy (continuum) version of this model is that it describes a topological phase transition between a trivial and non-trivial \mathbb{Z}_2 topological phase, through a massive Dirac-Schrödinger theory. This field theory, especially in the presence of a $U(1)$ vortex, has not been widely studied in its own right. A peculiar property of this theory is that the presence of both linear and quadratic kinetic terms *together* with the ordinary Dirac mass term allows for the gap-closing transition which changes the Chern number of the bands and the \mathbb{Z}_2 invariant. From a broader perspective, the relationship of the π -flux modes to the QSH phase and the question of their protection can therefore also be regarded in the general context of zero-energy fermionic modes bound to topological defects, which in fact comprises a rich literature [103, 104, 105, 90, 91, 106].

3.1 Zero-modes bound to a π -flux vortex

We here derive the analytic form of the zero-modes in the continuum version of the $M - B$ model (2.7). In particular, let us focus on the non-trivial regime $0 < M/B < 4$, meaning that the Dirac cone formed by the surface states is associated with the Γ point in the Brillouin zone (Figure 2.3), and set the expansion parameter A to unity. Taking the continuum, i.e. large wavelength limit ($|\mathbf{k}| \ll 1$), we arrive at a Dirac Hamiltonian which besides the ordinary Dirac mass term (M) contains a Schrödinger kinetic term (B)

$$H_{\text{eff}}(\mathbf{k}) = i\gamma_0\gamma_i k_i + (M - B\mathbf{k}^2)\gamma_0. \quad (3.1)$$

Here, the four-dimensional γ -matrices satisfy the canonical anticommutation relations $\{\gamma_\alpha, \gamma_\beta\} = 2\delta_{\mu\nu}$ and are given by $\gamma_0 = \tau_3 \otimes \sigma_0$, $\gamma_1 = \tau_2 \otimes \sigma_3$, $\gamma_2 = -\tau_1 \otimes \sigma_0$. Furthermore, the Pauli matrices $\{\sigma_0, \sigma_\mu\}$ act in the spin space, with τ_0, σ_0 representing the 2×2 identity matrices.

Considering the effect of the magnetic π -flux, it is sufficient to focus on a single spin projection, since the two spin projections are related by the time-reversal operator $T = -i\sigma_2 K$, with K being the complex conjugation. In the lattice model this π -flux can

then readily be incorporated using a Peierls substitution, which amounts to the minimal coupling $\mathbf{k} \rightarrow \mathbf{k} + \mathbf{A}$ in its continuum counterpart. As result, the Hamiltonian (3.1) for the spin up part assumes the form

$$H_{\text{eff}}(\mathbf{k}, \mathbf{A}) = \tau_i(k_i + A_i) + [M - B(\mathbf{k} + \mathbf{A})^2] \tau_3, \quad (3.2)$$

where the vector potential

$$\mathbf{A} = \frac{-y\mathbf{e}_x + x\mathbf{e}_y}{2r^2} \quad (3.3)$$

represents the magnetic vortex carrying the flux $\Phi = \pi$.

The remainder of this section is dedicated to showing that the above Hamiltonian possesses precisely one bulk zero-energy state with spin up. Expressing the Hamiltonian (3.2) in polar coordinates (r, φ) , taking into account that $\mathbf{A} = (1/2r)\mathbf{e}_\varphi$, we obtain

$$\begin{aligned} H_{\text{eff}} &= -ie^{-i\varphi} \left[\partial_r - \frac{i}{r} \tilde{\partial}_\varphi \right] \tau_+ - ie^{i\varphi} \left[\partial_r + \frac{i}{r} \tilde{\partial}_\varphi \right] \tau_- \\ &+ \left[M + B \left(\partial_r^2 + \frac{1}{r} \partial_r + \frac{1}{r^2} \tilde{\partial}_\varphi^2 \right) \right] \tau_3, \end{aligned} \quad (3.4)$$

where $\tilde{\partial}_\varphi \equiv \partial_\varphi + i/2$, and $\tau_\pm \equiv (\tau_1 \pm i\tau_2)/2$. It is easy to see that in case of an arbitrary flux Φ , the Hamiltonian (3.2) also acquires the form (3.4), but with the operator $\tilde{\partial}_\varphi = \partial_\varphi + i\Phi/2\pi$. In the presence of a vortex carrying a π flux, we can exploit the well-defined angular momentum and seek for solutions of the form

$$\Psi(r, \varphi) = \sum_l c_l \Psi_l(r, \varphi), \quad (3.5)$$

where

$$\Psi_l(r, \varphi) = \begin{pmatrix} e^{il\varphi} u_l(r) \\ e^{i(l+1)\varphi} v_{l+1}(r) \end{pmatrix}, \quad l \in \mathbb{Z}. \quad (3.6)$$

As a result, the functions u, v are subjected to the following equations

$$\Delta_{l+\frac{1}{2}} u_l(r) - i \left(\partial_r + \frac{l+\frac{3}{2}}{r} \right) v_{l+1}(r) = 0 \quad (3.7)$$

$$i \left(\partial_r - \frac{l+\frac{1}{2}}{r} \right) u_l(r) + \Delta_{l+\frac{3}{2}} v_{l+1}(r) = 0. \quad (3.8)$$

Here the operator Δ_l is defined as

$$\Delta_l \equiv M + B \left(\partial_r^2 + \frac{1}{r} \partial_r - \frac{l^2}{r^2} \right) \equiv M + B O_l. \quad (3.9)$$

Acting on Eq. (3.7) with the operator $\Delta_{l+\frac{3}{2}}$, and using the identity

$$[\Delta_l, \partial_r + \frac{l}{r}] = -(2l-1)\frac{B}{r^2} \left(\partial_r + \frac{l}{r} \right), \quad (3.10)$$

we can eliminate the function $v_{l+1}(r)$ from the same equation to obtain

$$\left(\Delta_{l+\frac{3}{2}} \Delta_{l+\frac{1}{2}} - O_{l+\frac{1}{2}} + \frac{2B(l+1)}{r^2} \Delta_{l+\frac{1}{2}} \right) u_l(r) = 0. \quad (3.11)$$

After some algebra, the above equation can then be rewritten as

$$\left[M^2 + (2MB-1)O_{l+\frac{1}{2}} + B^2 O_{l+\frac{1}{2}}^2 \right] u_l(r) = 0. \quad (3.12)$$

This result may also be obtained by noting that if the spinor in Eq. (3.6) is an eigenstate with the zero eigenvalue of the Hamiltonian (3.2), then it is also an eigenstate with the same eigenvalue of the square of this Hamiltonian. Using Eq. (3.2), one then readily obtains

$$H_{\text{eff}}(\mathbf{k}, \mathbf{A})^2 = B^2(\tilde{\mathbf{k}}^2)^2 + (1-2MB)\tilde{\mathbf{k}}^2 + M^2, \quad (3.13)$$

with $\tilde{\mathbf{k}} \equiv \mathbf{k} + \mathbf{A}$, and the operator $\tilde{\mathbf{k}}^2$ after acting on the angular part of the upper component of the spinor (3.6) yields Eq. (3.12). Similarly, it may be shown that the function $v_l(r)$ in the spinor given by Eq. (3.6) obeys an equation of the same form as (3.12) with $l \rightarrow l+1$. From Eq. (3.12) we conclude that the function $u_l(r)$ is an eigenfunction of the operator $O_{l+1/2}$ with a *positive* eigenvalue

$$O_{l+\frac{1}{2}} u_l(r) = \lambda^2 u_l(r), \quad (3.14)$$

since the operator $\tilde{\mathbf{k}}^2$ when acting on a function with the angular momentum l is equal to $-O_{l+1/2}$, and the eigenstates of the operator $\tilde{\mathbf{k}}^2$ with a *negative* eigenvalue are localized. Eqs. (3.12) and (3.14) therefore imply

$$\lambda_{\pm} = \frac{1 \pm \sqrt{1-4MB}}{2B}, \quad (3.15)$$

and, accordingly, solutions of the form $u_l(r) \sim I_{l+\frac{1}{2}}(\lambda r)$, where $I_l(x)$ is the modified Bessel function of the first kind. However, from the above solutions the only square-integrable ones are those associated with $l-1$ since $I_l(x) \sim x^{-|l|}$ as $x \rightarrow 0$. Furthermore, only the linear combination $I_{1/2}(x) - I_{-1/2}(x) \sim x^{-1/2}e^{-x}$ has the asymptotic behavior at infinity consistent with a finite norm of the state.

As a result, we only find square-integrable zero-energy solutions in presence of the π -flux vortex. Indeed, there are no normalizable solutions in the absence of the vortex, due to the asymptotic behavior of the modified Bessel functions. However, introducing the π -flux shifts the angular momentum l of the solutions (3.6) by a half, resulting in two square integrable zero-energy solutions in the zero angular momentum channel, being the localized $l = -1$ solutions. In order to make these solutions more explicit, we should distinguish two regimes of parameters, $0 < MB < 1/4$ and $MB > 1/4$, for which the argument of the square-root is positive and negative, respectively. For $0 < MB < 1/4$, since the argument of the square-root in the above equation is positive, we obtain two zero-energy solutions

$$\Psi_{\pm}(\mathbf{r}) = \frac{e^{-\lambda_{\pm}r}}{\sqrt{2\pi\lambda_{\pm}^{-1}r}} \begin{pmatrix} e^{-i\varphi} \\ i \end{pmatrix}, \quad (3.16)$$

with $\lambda_{\pm} > 0$ because of the square-integrability. On the other hand, when $MB > 1/4$, up to a normalization constant, the solutions have the form

$$\begin{aligned} \Psi_1(\mathbf{r}) &= \frac{e^{-r\sqrt{\frac{M}{B}}\cos\theta} \cos\left(r\sqrt{\frac{M}{B}}\cos\theta\right)}{\sqrt{r}} \begin{pmatrix} e^{-i\varphi} \\ i \end{pmatrix}, \\ \Psi_2(\mathbf{r}) &= \frac{e^{-r\sqrt{\frac{M}{B}}\cos\theta} \sin\left(r\sqrt{\frac{M}{B}}\cos\theta\right)}{\sqrt{r}} \begin{pmatrix} e^{-i\varphi} \\ i \end{pmatrix}, \end{aligned} \quad (3.17)$$

where

$$\theta = \frac{1}{2} \arctan \frac{\sqrt{|1-4MB|}}{1-2MB}. \quad (3.18)$$

However, since the identity

$$\sqrt{x} \cos\left(\frac{1}{2} \arctan \frac{\sqrt{|1-4x|}}{1-2x}\right) = \frac{1}{2} \quad (3.19)$$

holds for $1/4 < x < 4$, the localization length of the zero-modes for $MB > 1/4$ is actually just a constant independent of M, B , namely Eq. (3.17) becomes

$$\begin{aligned} \Psi_1(\mathbf{r}) &= \frac{e^{-\frac{r}{2B} \cos\left(\frac{r}{2B}\right)} \cos\left(\frac{r}{2B}\right)}{\sqrt{r}} \begin{pmatrix} e^{-i\varphi} \\ i \end{pmatrix}, \\ \Psi_2(\mathbf{r}) &= \frac{e^{-\frac{r}{2B} \sin\left(\frac{r}{2B}\right)} \sin\left(\frac{r}{2B}\right)}{\sqrt{r}} \begin{pmatrix} e^{-i\varphi} \\ i \end{pmatrix}. \end{aligned} \quad (3.20)$$

Therefore, we conclude that the Hamiltonian (3.2) possesses zero-energy modes in the entire range of parameters M and B for which the system is in the topologically non-trivially phase, $0 < M/B < 4$.

Notice also that in the regime when $0 < MB < 1/4$, there are two characteristic length scales associated with the midgap modes, $\xi_{\pm} \sim \lambda_{\pm}^{-1}$. Of course, after a short-distance regularization is imposed, only a linear combination of the two states survives. The physical interpretation of the two length scales depends on the form of the superposition of the state after the regularization has been imposed, as it may be easily seen from the form of the states (3.16). In the regime $MB > 1/4$, the zero-energy states are characterized by a single length-scale $\xi_{\text{loc}} \sim 2B$, which is at the same time the localization length and characterizes the oscillations of the exponentially decaying state.

Furthermore, although the bulk system does not feature normalizable zero-energy solutions, the edge states are closely related to the zero modes bound to the vortex. A derivation analogous to the one in subsection 2.2.3 reveals that by imposing open boundary conditions on the wave-functions at one of the edges of the system, for instance the one perpendicular to the x -axis, the obtained surface states for $k_y = 0$ feature a penetration depth given by exactly the same expression as the localization length for the zero-energy modes bound to the π -flux vortex. This signals that the bulk-boundary correspondence may thus be probed by inserting a π -flux vortex in the quantum spin Hall system.

We observe, nonetheless, that the zero-energy modes, given by Eqs. (3.16) and (3.20), form an overcomplete basis. This is a consequence of the fact that the Hamiltonian (3.2) is not self-adjoint due to the singularity of the vortex vector potential (3.3) at the origin. In order to overcome this apparent inconsistency, the gauge potential has to be regularized. Essentially, the regularization procedure then fixes the physical solution as a particular linear combination of the two basis states. This procedure is discussed in the subsequent subsection.

3.1.1 Self-adjoint extension

The simplest possible regularization is provided by considering the vortex with the flux concentrated in a thin annulus of a radius R . Let us first consider the Hamiltonian in the range of parameters $0 < MB < 1/4$. The zero-energy state of the Hamiltonian outside the annulus is then a linear combination of the modes Ψ_{\pm} given by Eq. (3.16). Inside

the annulus the vector potential $\mathbf{A} = 0$, and hence the zero-energy modes are

$$\Psi_{<}(\mathbf{r}) = C_1 \begin{pmatrix} e^{-i\varphi} I_{-1}(\lambda_+ r) \\ i I_0(\lambda_+ r) \end{pmatrix} + C_2 \begin{pmatrix} e^{-i\varphi} I_{-1}(\lambda_- r) \\ i I_0(\lambda_- r) \end{pmatrix}, \quad (3.21)$$

with λ_{\pm} given by Eq. (3.15), and $C_{1,2}$ being complex constants. By matching these solutions at $r = R$, and taking $R \rightarrow 0$, we obtain, up to a normalization constant, the zero-energy state

$$\Psi(\mathbf{r}) = \frac{e^{-\lambda_+ r} - e^{-\lambda_- r}}{\sqrt{r}} \begin{pmatrix} e^{-i\varphi} \\ i \end{pmatrix}. \quad (3.22)$$

Notice that this zero-energy state is regular at the origin which is a consequence of the regularity at the origin of the solutions (3.21) of the vortex-free problem. Similarly, one can readily show that when $MB > 1/4$ the zero-energy mode is given by the spinor Ψ_2 in Eq. (3.17) which is resultantly also regular at the origin and behaving $\sim r^{1/2}$ when $r \rightarrow 0$. Finally, an identical evaluation for the trivial regime $MB < 0$ shows that there are no square integrable combinations, that are also regular at the origin. This confirms that the modes are also intricately related to the non-trivial \mathbb{Z}_2 nature of the bulk system.

Although the above regularization results in concrete solutions, we should consider the self-adjoint extension of the corresponding Hamiltonian (3.2) in a more general manner by specifying the proper Hilbert space. Specifically, the application of the standard theory of self-adjoint extensions (SAE) [107, 108, 109, 110] prescribes that we need to ensure that the massive Dirac Hamiltonian (a differential operator) becomes Hermitian (self-adjoint) only after choosing the proper Hilbert space (i.e. domain of functions) on which it is allowed to act. Using von Neumann's construction by looking directly at the conditions under which the Hamiltonian is Hermitian when acted on arbitrary square integrable functions, we can then obtain the coefficients of the linear combination $C_1 \Psi_+ + C_2 \Psi_-$ unambiguously.

Rescaling the eigenfunctions (3.6) by $\psi_l(r, \varphi) = \frac{1}{\sqrt{r}} \tilde{\psi}_l(r, \varphi)$, the radial part of the Hamiltonian containing the singularity assumes the form

$$\tilde{H}_r^l(r) = \begin{pmatrix} m + B[\partial_r^2 + \frac{l(l+1)}{r^2}] & -i(\partial_r + \frac{l+1}{r}) \\ -i(\partial_r - \frac{l+1}{r}) & -m - B[\partial_r^2 + \frac{(l+1)(l+2)}{r^2}] \end{pmatrix}. \quad (3.23)$$

The hermiticity requirement then imposes the following condition

$$\begin{aligned}
0 &= \langle \tilde{\chi}_l | \tilde{H}_r^l - (\tilde{H}_r^l)^\dagger | \tilde{\psi}_l \rangle \\
&= \int dr \tilde{\chi}_l(r)^* \tilde{H}_r^l(r) \tilde{\psi}_l(r) - \left(\int dr \tilde{\psi}_l(r)^* \tilde{H}_r^l(r) \tilde{\chi}_l(r) \right)^* \\
&= B \{ \tilde{w}^* \partial_r \tilde{u} - (\partial_r \tilde{w}^*) \tilde{u} - \tilde{x}^* \partial_r \tilde{v} + (\partial_r \tilde{x}^*) \tilde{v} \} \Big|_0^\infty - i \{ \tilde{w}^* \tilde{v} + \tilde{x}^* \tilde{u} \} \Big|_0^\infty \\
&= \left[B(\tilde{\alpha}^* \sigma_3 \partial_r \tilde{\beta} - (\partial_r \tilde{\alpha}^*) \sigma_3 \tilde{\beta}) - i \tilde{\alpha}^* \sigma_1 \tilde{\beta} \right] (r=0), \tag{3.24}
\end{aligned}$$

on the arbitrary wave functions $\chi_l(r, \varphi)$ and $\psi_l(r, \varphi)$, which vanish at infinity and take the form defined in Eq.(3.6) in terms of the radial components

$$\chi_l(r) \equiv \begin{pmatrix} w_l(r) \\ x_{l+1}(r) \end{pmatrix} \equiv \alpha(r) \quad \text{and} \quad \psi_l(r) \equiv \begin{pmatrix} u_l(r) \\ v_{l+1}(r) \end{pmatrix} \equiv \beta(r). \tag{3.25}$$

The above requirement (3.24) results in a continuous family of restrictions on the behavior of square-integrable functions at the origin, the corresponding parametrization of which is obtained by exploiting its linearity. Namely, we can define two linear surjective maps Γ_1, Γ_2 from the domain $\mathcal{D}(\tilde{H}^\dagger)$, being arbitrary functions, onto their value at the boundary. These operators are defined by Eq. (3.24)

$$\left[B(\tilde{\alpha}^* \sigma_3 \partial_r \tilde{\beta} - (\partial_r \tilde{\alpha}^*) \sigma_3 \tilde{\beta}) - i \tilde{\alpha}^* \sigma_1 \tilde{\beta} \right] (0) \equiv \langle \Gamma_2 \tilde{\alpha}, \Gamma_1 \tilde{\beta} \rangle - \langle \Gamma_1 \tilde{\alpha}, \Gamma_2 \tilde{\beta} \rangle. \tag{3.26}$$

In particular, we may choose the following explicit form

$$\begin{aligned}
\Gamma_1 \tilde{\beta} &= B \sigma_3 \partial_r \tilde{\beta}(0) - i \frac{\sigma_1}{2} \tilde{\beta}(0), \\
\Gamma_2 \tilde{\beta} &= \tilde{\beta}(0),
\end{aligned} \tag{3.27}$$

showing that the boundary space indeed becomes $\mathcal{H}_b = \mathbb{C}^2$, as any vector in this space is the image of some wavefunction under Γ_i .

The most general relation that has to be satisfied by a wavefunction such that (3.24) holds is now parametrized by unitary mappings U in \mathcal{H}_b :

$$\mathcal{D}(\tilde{H}_U) = \{ \psi | (U - \sigma_0) \Gamma_1 \psi + i(U + \sigma_0) \Gamma_2 \psi = 0 \}, \tag{3.28}$$

with σ_0 the 2x2 identity matrix, and \mathcal{D} denoting the domain of operator. One can directly understand from (3.26) that forcing arbitrary linear combinations of a general $\tilde{\beta}(0)$ and $\partial_r \tilde{\beta}(0)$ to zero will still preserve the condition (3.24), due to the linearity and the anti-symmetric nature of the form of this expression. Eq. (3.28) thus gives us a precise recipe

and parametrization of the fact that this is the most general restriction that needs to be made on the wavefunctions $\tilde{\boldsymbol{\beta}}(r)$, i.e. on the $\boldsymbol{\psi}(r)$.

The form of Γ_i can now directly be used to explore the allowed boundary conditions on the wavefunctions and, in particular, to determine whether there is a self-adjoint extension \tilde{H}_U with the previously found zero energy states in its domain. For concreteness we will concentrate on the case that $MB < 1/4$, although the procedure is completely general. Since \mathcal{H}_b is \mathbb{C}^2 , the relevant mappings $U \in U(2)$ can be parametrized as

$$U = \frac{1}{d} \sum_{\mu} m_{\mu} q_{\mu}, \quad m_{\mu} \in \mathbb{R}, \quad \sum_{\mu} m_{\mu}^2 = 1, \quad d \equiv \begin{pmatrix} e^{i\eta} & 0 \\ 0 & 1 \end{pmatrix}, \quad \eta \in [0, 2\pi), \quad (3.29)$$

relative to the quaternion basis $q_{\mu} = (\sigma_0, i\vec{\sigma})$. Focussing first on the case $\eta = 0$, the condition (3.28) results in

$$\{B \sum_{\mu} \zeta_{\mu} q_{\mu}\} \partial_r(\sqrt{r}\psi_0)|_{r=0} = \{\sum_{\mu} \eta_{\mu} q_{\mu}\} \sqrt{r}\psi_0|_{r=0}, \quad (3.30)$$

where

$$\begin{aligned} \zeta_{\mu}^{\top} &= (-im_3, -im_2, im_1, i(m_0 - 1)), \\ \eta_{\mu}^{\top} &= \left(\frac{m_1}{2} + i(1 + m_0), \frac{1 - m_0}{2} + im_1, \frac{m_3}{2} + im_2, -\frac{m_2}{2} + im_3\right). \end{aligned} \quad (3.31)$$

Moreover, since

$$\sqrt{r}\psi_0|_{r=0} = \begin{pmatrix} C_1 + C_2 \\ i(C_1 + C_2) \end{pmatrix} \quad \text{and} \quad \partial_r(\sqrt{r}\psi_0)|_{r=0} = -\begin{pmatrix} C_1\lambda_- + C_2\lambda_+ \\ i(C_1\lambda_- + C_2\lambda_+) \end{pmatrix}, \quad (3.32)$$

with λ_{\pm} the positive solutions of Eq. (3.15), we obtain a relation between C_1 and C_2 as function of the particular self-adjoint extension m_{μ} . In this case, m_{μ} parameterizes the hypersphere S^3 and can correspondingly be rewritten in terms of angular coordinates

$$m_{\mu} = (\cos \psi, \sin \psi \cos \theta, \sin \psi \sin \theta \cos \varphi, \sin \psi \sin \theta \sin \varphi), \quad (3.33)$$

where $\psi \in [0, \pi]$, $\theta \in [0, \pi]$, and $\varphi \in [0, 2\pi)$. Given the parameters M and B , Eq. (3.30) thus results in a parameterized family of restrictions on the solutions, specifying the self-adjoint domain.

We notice that $\det(\sum_{\mu} \zeta_{\mu} q_{\mu}) = \sum_{\mu} \zeta_{\mu}^2 = 2(m_0 - 1)$. Let us therefore consider the case $m_0 = 1$ explicitly. Setting m_0 to unity immediately implies $m_{\mu \neq 0} = 0$ and hence results in $0 = i\sigma_0 \tilde{\psi}(0) = i\sigma_0 \sqrt{r}\psi(0)$. This then yields $C_1 = -C_2$ and thus pertains to

the zero energy solution (3.22) found with the thin solenoid regularization. In fact, a detailed analysis [111] shows that this self adjoint extension, determined by $\eta = \psi = 0$, is the *only* possible extension which allows for the existence of a zero energy state that is *both* localized and regular (vanishing) at the origin. Moreover, the SAE procedure similarly applies to the other regime, thereby reconfirming the above intuitive approach. This then finally concludes the proof that the spin projected Hamiltonian (3.2) hosts a single zero-energy mode in the topological regime $0 < M/B < 4$.

3.2 Quantum numbers of the zero-energy modes

The above derived zero-energy modes can be associated with the same spin-charge separated quantum numbers appertaining to the Jackiw-Rebbi solitons in the Su-Schieffer-Heeger model. To make this concrete, we consider the continuum 4×4 Hamiltonian (3.1) coupled to the $U(1)$ vector potential

$$H = i\gamma_0\gamma_i(k_i + A_i) + (M - B(\mathbf{k} + \mathbf{A})^2)\gamma_0 \quad (3.34)$$

where the vector potential \mathbf{A} given by Eq. (3.3). We note that the unitary matrices $\gamma_3 = \sigma_2 \otimes \tau_2$ and $\gamma_5 = \sigma_2 \otimes \tau_1$ anticommute with the gamma-matrices γ_α , $\alpha = 0, 1, 2$. Therefore, the Hamiltonian anticommutes with the matrices $\Gamma_3 \equiv i\gamma_0\gamma_3$ and $\Gamma_5 \equiv i\gamma_0\gamma_5$ which then generate chiral (spectral) symmetry relating states with positive and negative energies, i.e., if $H|E\rangle = E|E\rangle$, then, for instance, $\Gamma_5|E\rangle = |-E\rangle$, and the matrix Γ_5 reduces in the zero-energy subspace of the Hamiltonian. As a result, we can straightforwardly apply Eq. (2.14),

$$\langle Q \rangle = \frac{1}{2} \left(\sum_{\text{occupied}} \Psi_E^\top Q \Psi_E - \sum_{\text{unoccupied}} \Psi_E^\top Q \Psi_E \right), \quad (3.35)$$

to obtain the same ground state quantum numbers $\langle Q \rangle$ characterizing the polyacetylene case. Namely, when both states are occupied or empty the charge is $+e$ or $-e$ and the spin quantum number is zero, whereas single occupied modes are characterized by a spin quantum number $-1/2$ or $1/2$ and a net charge zero. These results can additionally be understood from a physical perspective [99]. Since a π -flux is equivalent to a $-\pi$ -flux, there are four different adiabatic processes that result in the same final flux configuration. That is, for each spin projection $\uparrow (\downarrow)$ the flux can adiabatically be increased from 0 to $\pm\pi$. Considering a loop around the vortex, Faraday's law of induction then implies that

during such an adiabatic process a tangential electric field is induced along the loop. Accordingly, the quantized Hall conductivity per sub block thus results in a net charge transfer per spin component along the loop that simply amounts to $\Delta Q_{\uparrow(\downarrow)} = \mp e/2$ for the $\pm\pi$ -flux process. Combining the four different scenarios $\phi_{\uparrow,\downarrow} = \pm\pi$, we then readily obtain the net relative charge $\Delta Q = Q_{\uparrow} + Q_{\downarrow}$ and spin $\Delta S_z = Q_{\uparrow} - Q_{\downarrow}$ for each case, culminating in the outlined quantum numbers.

3.3 π -fluxes as a bulk classification tool

Although the discrepancy in spatial dimensions allows for the spin-charge separated quantum numbers of the vortex zero-modes, we notice that the characterization of the modes is nevertheless rather reminiscent of the edge state description. Of topical interest in this regard is the question to what extent the above indicated relation between the existence of the zero-modes and the non-trivial topological characterization of the bulk system, formalized by the bulk-boundary correspondence in the case of the surface states, translates to a profound entity. Interestingly, it turns out that the π -flux modes are indeed intricately tied to the \mathbb{Z}_2 topological nature of the quantum spin Hall phase [99, 100], making them versatile probes of the non-trivial order. Let us now make this somewhat more concrete.

Concerning the topological stability of the mid gap states, being the stability under continuous deformations of the vector potential, it is well-known that both the Dirac and Schrödinger Hamiltonian are characterized by an index theorem [103, 104]. However, as the continuum theory (3.1) entails a combination of the two, a definite index theorem mathematically relating the number of zero-modes to the non-triviality of the defining differential operator is yet to be established. Moreover, it is evident that in the above treatment the description of the zero-modes coincides with the manifest chiral symmetry of the $M - B$ model (2.7), which in the generic context amounts to an artifact rather than a fundamental symmetry. Fortunately, the generality of the Laughlin argument allows nonetheless for an explicit verification of the intricate relation between the π -flux modes and the QSH phase also in absence of the additional spin $U(1)_s$ symmetry.

As a first step it is important to realize that actually only TRS is needed to define spin-charge separated modes, as the time reversal operator T acts differently on integer and half-integer spin states. Specifically, denoting the electron number operator

as N , one can generalize the concept of spinons to arbitrary quantum states satisfying $(-1)^N|\psi_s\rangle = |\psi_s\rangle$ and $T^2|\psi_s\rangle = -|\psi_s\rangle$. Correspondingly, states transforming as $(-1)^N|\psi_c\rangle = -|\psi_c\rangle$, $T^2|\psi_c\rangle = |\psi_c\rangle$ define chargeons and holons. These concepts subsequently allow for the construction of an explicit invariant that quantifies the non-trivial \mathbb{Z}_2 order of the assumed unique ground state. Namely, consider the adiabatic process of π -flux threading represented by the matrix Γ , as function of the interpolating parameter $\theta \in [0, \pi]$. In the case of a lattice model the hoppings along some cut ending on the vortex are then altered as $t_{ab} \rightarrow t_{ab}e^{i\theta(t)\Gamma}$, whereas in the continuum setting this amounts to an evident redefinition of the gauge potential. Crucially, for *any* time reversal odd matrix Γ , satisfying $(-1)^{i\pi\Gamma} = -1$, one can then show that such an adiabatic process results in the pumping of an integer N_Γ amount of charge to the flux tube, proving that $(-1)^{N_\Gamma}$ defines a \mathbb{Z}_2 invariant [99, 112].

The arguments underlying these facts find their foundation in the Laughlin argument. In particular, as the resulting state after spin flux threading can similarly be obtained by charge flux threading we can consider the closed path $l = l_c^{-1}l_\Gamma$ in parameter space [112]. Here l_c, l_Γ refer to adiabatic paths associated with charge and spin flux threading, respectively. As the ground state is unique and the response during the charge threading process equates to zero by virtue of time reversal symmetry, we immediately conclude that an integer amount of charge is pumped to the flux tube by the spin flux threading process. Moreover, for two different adiabatic processes Γ_1 and Γ_2 , the closed path $l_{\Gamma_2}^{-1}l_{\Gamma_1}$ has to result in the transport of an even multiple of charge, as it must map the unique ground state (e.g. a Kramers singlet) to itself (again a Kramers singlet). This shows that the invariant $(-1)^{N_{\Gamma_{1,2}}}$ is independent of $\Gamma_{1,2}$.

As a result, we see that the adiabatic π -flux threading is thus directly related to a concrete invariant characterizing the \mathbb{Z}_2 phase. Only in the case of a non-trivial \mathbb{Z}_2 invariant, an odd multiple of charge is transported to the flux tube for the appropriate Γ . Moreover, using the explicit occupation relation between the chargeons/holons and spinons in conjunction with Kramers theorem, we conclude that the *formation* of the mid gap modes bound to the π -flux vortex is in direct correspondence with the topological non-triviality of the bulk system. In the specific context of the previous subsection, we may, for example, consider the process associated with $\phi_\uparrow = -\phi_\downarrow = \pi$ represented by the matrix $\Gamma = \sigma_z \otimes \tau_0$, creating the chargeon state in the non-trivial regime. Due to the outlined arguments the associated mid gap modes are then stable to perturbations that do not close the gap, although in the absence of spectral symmetry they are no longer

pinned to zero-energy.

From a heuristic point of view, the transition maps of the vector bundle structure associated with the non-trivial \mathbb{Z}_2 phase imply that during a full Laughlin cycle the many body energy levels cross an odd number of times. As noted before, insertion of half a quantum flux, i.e. a π -flux, thus results in a change in degeneracy for the edges of the system, characterizing the physical significance of the \mathbb{Z}_2 invariant (Figure 1.3). Accordingly, we see that a similar mechanism lies at heart of the appearance of a *single* Kramers pair of mid-gap modes at the π -flux vortex, the formation of which then mimics the usual bulk-boundary correspondence. Notice in this regard that in case of periodic boundary conditions the effective spin transfer is then associated with the two time reversed Kramers pairs of mid gap modes at the two different defects. Similarly, for a single defect in an open boundary system this process has to be identified with a spectral flow on the edge due to charge neutrality, conforming the intricate relation between the defect modes and the surface states.

3.4 Dislocations as probes of the physics beyond the tenfold way

As shown, the π -flux modes represent universal topological observables that intricately relate to the \mathbb{Z}_2 topological status of the bulk. However, the derived notions come to live in the context of dislocations. In particular, as the piercing of π -fluxes through elementary plaquettes of the size of the lattice constant is far from experimentally viable, experimental ubiquitous defects that effectively amount to flux probes are obviously consequential in this regard. Numerical simulations have already hinted that dislocations can act as pseudo-magnetic fluxes [113], and we will exploit their prominent role in detail in the remainder.

Most importantly, as dislocations are the unique topological defects associated with the transitional symmetry breaking of the underlying lattice, these results in turn expose a route to an additional classification scheme that incorporates the lattice symmetries. Namely, the tenfold way, based on time-reversal symmetry and particle-hole symmetry, relies on the spatial continuum limit while TBIs actually necessitate a crystal lattice that breaks the translational symmetry. The simple $M - B$ model (2.7),

$$\mathcal{H}(k_x, k_y) = \begin{pmatrix} H(\mathbf{k}) & 0 \\ 0 & H^*(-\mathbf{k}) \end{pmatrix} = A \sin(k_x) \gamma_x + A \sin(k_y) \gamma_y + M(\mathbf{k}) \gamma_0, \quad (3.36)$$

already gives away a generic wisdom in this regard. Depending on its parameters, this model describes topological phases which are in a thermodynamic sense distinguishable: their topological nature is characterized by a Berry phase skyrmion lattice (SL) in the extended Brillouin zone (BZ), where the sites of this lattice coincide with the reciprocal lattice vectors (“ Γ -phase”) or with the TRS points (π, π) (“ M -phase”).

Concretely, rewriting the spin projected sub blocks of the simple M - B model (2.7) in the compact form of Eq. (2.4),

$$H(k_x, k_y) = \mathbf{d}(\mathbf{k}) \cdot \boldsymbol{\tau}, \quad (3.37)$$

we observe (Figure 3.1) that in the topologically non-trivial Γ -phase the band-structure vector field $\hat{\mathbf{d}}(\mathbf{k}) \equiv \mathbf{d}(\mathbf{k})/|\mathbf{d}(\mathbf{k})|$ forms a skyrmion centered around the Γ -point in the BZ, with corresponding skyrmion density $s(\mathbf{k}) \equiv \hat{\mathbf{d}}(\mathbf{k}) \cdot (\partial_{k_x} \hat{\mathbf{d}}(\mathbf{k}) \times \partial_{k_y} \hat{\mathbf{d}}(\mathbf{k}))$. Here $s(\mathbf{k})$ tracks the position of minimal bandgap in the BZ, coinciding with it where $\hat{\mathbf{d}}(\mathbf{k}) \parallel \partial_{k_x} \hat{\mathbf{d}}(\mathbf{k}) \times \partial_{k_y} \hat{\mathbf{d}}(\mathbf{k})$. In the 2D extended BZ, this skyrmion structure forms a lattice which respects point group symmetry of the original square lattice. Moreover, in the M -phase, the skyrmion is centered at the M point in the BZ. The position of the corresponding skyrmion lattice relative to the extended BZ is therefore different than in the Γ -phase, although the skyrmion lattice still respects the point group symmetry of the square lattice. On the other hand, in the topologically trivial phase, the vector field \mathbf{d} forms no skyrmion in the BZ, consistent with the vanishing of topologically invariant spin Hall conductance $\sigma_{xy}^S = (4\pi)^{-1} \int_{BZ} d^2\mathbf{k} s(\mathbf{k})$. The position of the skyrmion lattice relative to the extended BZ thus encodes translationally active topological order which, as we now show, is probed by the lattice dislocations.

Let us first analytically motivate, using the elastic continuum theory, that a lattice dislocation effectively amounts to the above magnetic π -flux problem in the M phase. We consider a dislocation with Burgers vector \mathbf{b} , and expand the Hamiltonian (3.37) around the M -point in the BZ. As a next step, the dislocation introduces an elastic deformation of the medium described by the distortion $\{\boldsymbol{\varepsilon}_i(\mathbf{r})\}$ of the (global) Cartesian basis $\{\mathbf{e}_i\}$, $i = x, y$, in the tangent space at the point \mathbf{r} [114]. Consequently, the momentum in the vicinity of the M -point reads

$$k_i = \mathbf{E}_i \cdot (\mathbf{k}_M - \mathbf{q}) = (\mathbf{e}_i + \boldsymbol{\varepsilon}_i) \cdot (\mathbf{k}_M - \mathbf{q}), \quad (3.38)$$

where $\mathbf{k}_M = (\pi, \pi)/a$, \mathbf{q} is the momentum of the low-energy excitations, $|\mathbf{q}| \ll |\mathbf{k}_M|$, and we have restored the lattice constant a . The corresponding continuum Hamiltonian after this coarse graining [115] then assumes the form

$$H_{\text{eff}}(\mathbf{k}, \mathbf{A}) = \tau_i(k_i + A_i) + [\tilde{M} - \tilde{B}(\mathbf{k} + \mathbf{A})^2] \tau_3, \quad (3.39)$$

in terms of the redefinitions $\mathbf{q} \rightarrow \mathbf{k}$, $\tilde{M} \equiv M - 8B$, $\tilde{B} \equiv -B$, and $A_i \equiv -\boldsymbol{\varepsilon}_i \cdot \mathbf{k}_M$. The form of the distortion $\boldsymbol{\varepsilon}_i$ is determined from the dual basis in the tangent space at the point \mathbf{r} which in the case of a dislocation with $\mathbf{b} = a\mathbf{e}_x$ entails $\mathbf{E}^x = (1 - \frac{ay}{2\pi r^2})\mathbf{e}^x + \frac{ax}{2\pi r^2}\mathbf{e}^y$, $\mathbf{E}^y = \mathbf{e}^y$ [116]. Using that $\mathbf{E}_i \cdot \mathbf{E}^j = \delta_i^j$, we obtain the distortion field to the leading order in a/r , $\boldsymbol{\varepsilon}_x = \frac{ay}{2\pi r^2}\mathbf{e}_x$, $\boldsymbol{\varepsilon}_y = -\frac{ax}{2\pi r^2}\mathbf{e}_y$. This form of the distortion yields the vector potential

$$\mathbf{A} = \frac{-y\mathbf{e}_x + x\mathbf{e}_y}{2r^2} \quad (3.40)$$

in Eq. (3.39), demonstrating that the dislocation in the M -phase acts as a magnetic π -flux. On the other hand, in the Γ -phase, the continuum Hamiltonian has the generic form (3.39), with $\tilde{M} = M$ and $\tilde{B} = B$. However, the action of the dislocation in this case is trivial, since the bandgap is located at zero momentum rendering $\mathbf{A} = 0$. Applying the above results, we conclude that a dislocation must bind a Kramers pair mid gap modes in the M -phase, while having no effect in the Γ -phase.

These notions can readily be corroborated by numerical means. We find that a dislocation only binds a Kramers pair of zero-energy states in the M -phase, confirming that the dislocation acts as a π -flux in this phase. Moreover, we can show the robustness of these modes in the bulk gap when we introduce a random chemical potential, and thus break PHS. To this end we perform a numerical analysis on the tight-binding $M - B$

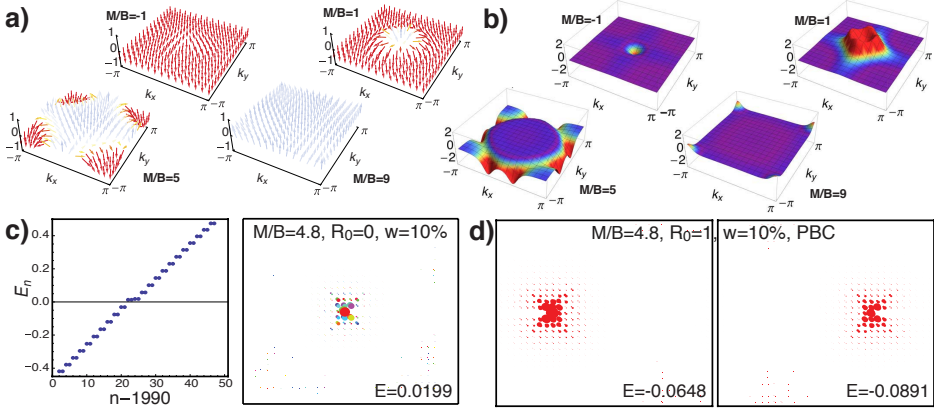


Figure 3.1: *Model of Eq. (3.36) in the BZ: (a) Band-structure $\hat{d}(\mathbf{k})$. (b) Skymion density $s(\mathbf{k})$. Mid-bulkgap localized dislocation states in 33×30 unit-cell $M - B$ tight-binding lattice with disorder. The Kramers degenerate pair states are omitted. (c) Dislocation in the center. Offset disks represent the amplitude of $s \uparrow, p \uparrow$ states, and the color their phase. (d) Total wavefunction amplitude in a periodic system (necessitating two dislocations), with Rashba coupling (R_0) mixing spins.*

model in real space

$$H_{TB} = \sum_{\mathbf{R}, \boldsymbol{\delta}} \left(\Psi_{\mathbf{R}}^{\dagger} \left[T_{\boldsymbol{\delta}} + i \frac{R_0}{2} (\tau_0 + \tau_3) \mathbf{e}_z \cdot (\boldsymbol{\sigma} \times \boldsymbol{\delta}) \right] \Psi_{\mathbf{R}+\boldsymbol{\delta}} + \Psi_{\mathbf{R}}^{\dagger} \frac{\varepsilon}{2} \Psi_{\mathbf{R}} + H.c. \right), \quad (3.41)$$

where $\Psi_{\mathbf{R}} = (s_{\uparrow}(\mathbf{R}), p_{\uparrow}(\mathbf{R}), s_{\downarrow}(\mathbf{R}), p_{\downarrow}^*(\mathbf{R}))$ annihilates the $\sim |s\rangle$ type, and $\sim |p_x + ip_y\rangle$ type orbitals at site \mathbf{R} and nearest neighbors $\boldsymbol{\delta} \in \{\mathbf{e}_x, \mathbf{e}_y\}$. Furthermore, we set

$$T_{\boldsymbol{\delta}, \uparrow\uparrow} = \begin{pmatrix} \Delta_s & t_{\boldsymbol{\delta}}/2 \\ t'_{\boldsymbol{\delta}}/2 & \Delta_p \end{pmatrix}$$

and $T_{\boldsymbol{\delta}, \downarrow\downarrow} = T_{\boldsymbol{\delta}, \uparrow\uparrow}^*$, with $t_x = t'_x = -i$, $t_y = -t'_y = -1$, $\Delta_{s/p} = \pm B + D$ and on-site energies $\varepsilon = [(C - 4D)\tau_0 + (M - 4B)\tau_3] \otimes \sigma_0$. This reproduces Eq. (3.37) when $C = D = 0$, implying vanishing chemical potential. Finally, the R_0 term is the nearest neighbor Rashba spin-orbit coupling [117] which induces a breaking of the $z \rightarrow -z$ reflection symmetry and resultantly the PHS symmetry.

Our numerical analysis of H_{TB} pertains to various system shapes and sizes, with varying disorder strengths given by multiplication of the parameters for each $\mathbf{R}, \boldsymbol{\delta}$ by

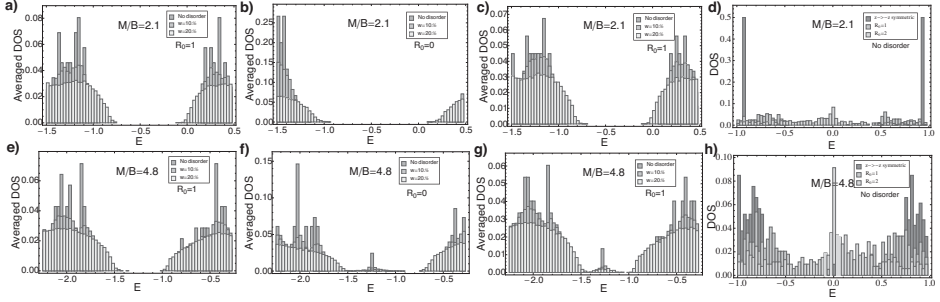


Figure 3.2: Comparison of Γ (a-d) and M (e-h) phases. The density of states of 21×18 lattice (100 disorder realizations averages), with $C \equiv 0.2|t|$, $D \equiv 0.3|t|$ setting the chemical potential, and R_0 the Rashba coupling. (a) and (e) In absence of dislocation. (b,f) Robust midgap dislocation modes are present only in M -phase; (c,g) Same is true upon spin mixing through R_0 . (d,h) Strong Rashba coupling closes the topological bulkgap.

Gaussian random variables of width w , while preserving TRS. Fig. 3.1(c) demonstrates the spectrum and the wavefunction at $w = 10\%$ disorder. Localization (even by weak disorder) decouples dislocation states from edges and possible edge roughness effects.

In the presence of the Rashba coupling ($R_0 \neq 0$, but not large enough to close the topological bulk gap [32]), the spins are mixed, but the Kramers pairs remain localized (Fig. 3.1(d)). Fig. 3.2 demonstrates the robustness of dislocation modes within the topological bulk gap, through the Rashba coupling perturbed and disorder averaged density of states (DOS) of H_{TB} in a periodic lattice, contrasted between the Γ and the M phase.

These findings are obviously consequential in the view of experimental verification. Dislocations are ubiquitous in any real crystal, for instance in the form of small angle grain boundaries, and we thus predict that their cores should carry zero modes, which should be easy to detect with scanning tunneling spectroscopy. As a matter of fact, the real experimental challenge lies in the realization of non- Γ TIs that are also easily accessible to spectroscopic measurements.

Moreover, we note that although the above considerations pertain to a simple toy model, that should be regarded in that sense, the characterization of the π -fluxes is completely general, as is the reminiscent principle concerning the dislocations. Hence, on a fundamental level the above results indicate the existence of a further subclassification, besides the “translationally trivial” Γ -type TBIs that are completely classified by

the tenfold way. In this specific case this characterization corresponds to the locus of the Berry phase skyrmion lattice in the extended BZ, however a more general classification method is highly desirable. This forms the subject of the next Chapter.

3.5 Conclusions

In conclusion, we have shown that the appearance of a pair of zero-modes bound to a magnetic π -flux is a generic feature of the $M - B$ model in the topologically non-trivial phase. In the continuum setting, these modes can analytically be derived and directly be related to the a particular self-adjoint extension of the continuum Hamiltonian. More generally, the existence of these mid gap states results in profound physical consequences. In particular, they provide for a two-dimensional realization of spin-charge separated quantum numbers. Of topical interest, however, is the deep relation between these special mid gap modes and the \mathbb{Z}_2 topological characterization of the bulk. Namely, the modes bound to the π -flux can directly be used to classify \mathbb{Z}_2 topological band insulators. These notions become physically profound in the context of dislocations. Specifically, dislocations act as π -fluxes, thereby binding similar mid gap modes, but only in certain \mathbb{Z}_2 topological insulators. This signals that there is a further subclassification, within the tenfold way.

Chapter 4

The space group classification of topological band insulators

The theoretical prediction and experimental realization of the \mathbb{Z}_2 -invariant topological band insulator (TBI) provided for a crucial boost in the revival of prominent interest in topological aspects of condensed matter systems and topological band theory in particular. As discussed in the introductory Chapters, these advancements found their foundation in the connection of the two a priori unrelated concepts of symmetry and topology, culminating in the construction of the tenfold periodic table. The role of the crystal lattice in this classification is to provide a unit cell in the momentum space, the Brillouin zone (BZ), topologically equivalent to the d -dimensional torus, over which the electronic Bloch wavefunctions are defined. The tenfold classification then follows by assuming that all the unitary symmetries of the corresponding Bloch Hamiltonian have been exhausted, rendering time reversal symmetry and particle hole symmetry as the only remaining anti-unitary symmetries due to Wigner’s theorem.

In three spatial dimensions (3D), however, by considering a \mathbb{Z}_2 TBI as a stack of two-dimensional (2D) ones, thus assuming a layered 3D lattice, additional three “weak” invariants associated with the discrete translation symmetry have been found [39]. Similarly, it has been realized that topological states protected just by inversion, can exist in 3D [38, 118, 119, 120, 121, 122]. Moreover, we demonstrated in the previous Chapter the existence of dislocation susceptible states that are protected by *both* TRS and the lattice C_4 rotational symmetry. Nonetheless, the generic role of the space group symmetries in the physics of topological states has remained elusive, in spite of these explicit

indications.

In this Chapter, we bridge this gap and provide for the complete classification of TBIs protected not only by TRS, but also by space group lattice symmetries. Using this general formulation, that naturally incorporates the crystalline symmetries, we then identify three general classes of \mathbb{Z}_2 topological insulating states: (a) Γ states robust against general time-reversal invariant perturbations; (b) Translationally-active states protected from elastic scattering, but susceptible to topological crystalline disorder; (c) Valley or crystalline topological insulators sensitive to the effects of non-topological and crystalline disorder. These three classes give in turn rise to 18 different two-dimensional, and, at least 70 three-dimensional TBIs, opening up a route for the systematic search for new types of TBIs.

4.1 Classification scheme and general principles

As a starting point, we depart from the construction by Fu and Kane [37, 38, 123] to compute the \mathbb{Z}_2 invariant in terms of the matrix of overlaps

$$w_{mn} = \langle u_m(-\mathbf{k}) | \vartheta | u_n(\mathbf{k}) \rangle, \quad (4.1)$$

where ϑ is the time-reversal operator and $|u_n(\mathbf{k})\rangle$ is the n -th occupied Bloch wavefunction. The quantities of central significance are

$$\delta_i = \frac{\sqrt{\det[w(\Gamma_i)]}}{\text{Pf}[w(\Gamma_i)]}, \quad (4.2)$$

evaluated at the points Γ_i in the BZ where the Hamiltonian commutes with the time-reversal operator. Since the matrix w is antisymmetric at the points Γ_i , the Pfaffian is well-defined at these points and $\det[w(\Gamma_i)] = (\text{Pf}[w(\Gamma_i)])^2$. The topological \mathbb{Z}_2 invariant, ν , is then given by $(-1)^\nu = \prod_{\Gamma_i} \delta_i$, and its non-triviality implies a topological obstruction for defining the wavefunctions through the entire BZ with an even number of band inversions. Heuristically, the above definition is thus yet another characterization of the fact that the mathematical vector bundle structure of a \mathbb{Z}_2 topological insulator features an odd number of non-trivial local transition maps, patching the wavefunctions globally in a topologically distinct manner over the Brillouin zone [25]. Notice also that the evaluation of the topological invariant in terms of the signs of the Pfaffian does not depend on the dimensionality but only on the fact that the Hamiltonian possesses TRS.

As a next step, the generality of Eq. (4.1) in conjunction with its momentum dependence can directly be exploited to signify the natural role of the underlying crystal symmetries. First, notice that the set of Γ_i points at which the Hamiltonian commutes with the time-reversal operator is in fact fixed by the space group of the lattice, see Table 4.1. Second, it is evident that we may choose the overall phase of the Bloch wavefunctions so that a unique phase, which we dub the “ Γ ” phase, has $\delta_\Gamma = -1$ at the Γ -point in the BZ and $\delta_i = 1$ at all the other high symmetry points. The crucial observation then pertains to the fact that *the distribution* of signs of the Pfaffian, δ_i , at the points Γ_i , and not only their product, resultantly encodes for additional topological structure. To show this, we first consider how the matrix of overlaps transforms under a lattice symmetry operation represented by a unitary operator U

$$w_{mn}(\mathbf{k}) = \langle u_m(-\mathbf{k}) | \vartheta | u_n(\mathbf{k}) \rangle = \langle u_m(-U\mathbf{k}) | U \vartheta U^\dagger | u_n(U\mathbf{k}) \rangle = w_{mn}(U\mathbf{k}). \quad (4.3)$$

As a consequence, when some of these high symmetry points are related by a point-group symmetry of the lattice, their signs of the Pfaffian have to be equal. Therefore, it is sufficient to consider a subset, Γ_a , of representative, inequivalent high symmetry points that are also *not related* by any symmetry. This leads to the following rule that allows for determination of all the topological phases given the space group and the corresponding high symmetry points, Γ_i : each phase is obtained by selecting a single representative high-symmetry point Γ_a and setting $\delta_{\Gamma_a} = -1$, which automatically sets $\delta_{\Gamma_b} = -1$ at all the high-symmetry points Γ_b related by point group symmetry to Γ_a . Such phases are separated by a topological quantum phase transition that involves a bulk bandgap closing which then changes the values of δ_i ’s.

This simple classification principle can be illustrated by an elementary 2D example. We start with the Γ phase on a square lattice, $\delta_\Gamma = -1$, and $\delta_X = \delta_Y = \delta_M = 1$ where X , Y , and M are the time-reversal invariant (TRI) momenta in the BZ. By applying our rule, we immediately see that, besides the Γ phase, we obtain an “ M ” phase with $\delta_M = -1$, and $\delta_\Gamma = \delta_X = \delta_Y = 1$ (Table 4.1). This phase is disconnected from the Γ phase through a topological quantum phase transition with the band gap closing at the X and Y points and pertains to the “translationally-active” phase encountered in the previous Chapter. Recall that this phase is also protected by TRS, but exhibits, in contrast to the Γ phase, susceptibility to dislocations. Furthermore, since the X and the Y points are related by a C_4 rotation, there can exist a phase with $\delta_X = \delta_Y = -1$, and $\delta_\Gamma = \delta_M = 1$. The product of the δ_i ’s at all TRI momenta then yields a trivial Z_2 invariant, $\nu = 0$. However, in this

Bravais Lattice (PG)	WpG	Γ_i	δ_i	Index (Phase)
Square (D_4)	$p4mm$	(Γ, M, X, Y)	$(-1, 1, 1, 1)$	$T-p4mm$ (Γ)
	$p4gm$		$(1, -1, 1, 1)$	$T-p4$ (M)
	$p4$		$(1, 1, -1, -1)$	$p4$ (X - Y -valley)
Rectangular (D_2)	$p2mm$	(Γ, M, X, Y)	$(-1, 1, 1, 1)$	$T-p2mm$ (Γ)
	$p2mg$		$(1, -1, 1, 1)$	$T-p2m_M$ (M)
	$p2gg$		$(1, 1, -1, 1)$	$T-p2m_X$ (X)
	pm, pg		$(1, 1, 1, -1)$	$T-p2m_Y$ (Y)
Rhombic (D_2)	$c2mm$	$(\Gamma, M_0, M_{-1}, M_1)$	$(-1, 1, 1, 1)$	$T-c2mm$ (Γ)
	cm		$(1, -1, 1, 1)$	$T-c2m$ (M_0)
			$(1, 1, -1, -1)$	$c2m$ (M -valley)
Oblique (C_2)	$p2$	$(\Gamma, M_0, M_{-1}, M_1)$	$(-1, 1, 1, 1)$	$T-p2$ (Γ)
	$p1$		$(1, -1, 1, 1)$	$T-p2_{M_0}$ (M_0)
			$(1, 1, -1, 1)$	$T-p2_{M_{-1}}$ (M_{-1})
			$(1, 1, 1, -1)$	$T-p2_{M_1}$ (M_1)
Hexagonal (hexagonal – D_6)	$p6mm$	$(\Gamma, M_0, M_{-1}, M_1, K_-, K_+)$	$(-1, 1, 1, 1, 1, 1)$	$T-p6mm$ (Γ)
	$p6$		$(1, -1, -1, -1, 1, 1)$	$T-p6$ (M)
			$(1, 1, 1, 1, -1, -1)$	$p6$ (K -valley)
Hexagonal (rhombohedral – D_3)	$p3m1$ $p31m, p3$	$(\Gamma, M_0, M_{-1}, M_1)$	$(-1, 1, 1, 1)$	$T-p3m1$ (Γ)

Table 4.1: Table of the topological phases in two dimensions. For each of the lattice structures, the corresponding point-group (PG) symmetry and the relevant wallpaper group (WpG), i.e. space group, are given. The corners of the square and rectangle are denoted by M , whereas in the triangular Bravais structure they are indicated by K . Additionally, the centers of the edges are denoted by X and Y in both the square and rectangular case and by M in the other lattices [124]. The resulting phases are characterized by the distribution of δ_i at the Γ_i points consistent with the WpG symmetry. Phases cluster in Bravais lattices, with the hexagonal structure being the only exception. In this case the WpGs containing six-fold and three-fold rotational symmetries relate the high symmetry points in different ways. As a result, the Hamiltonian does not commute with the time-reversal operator at the K points in the latter case. The obtained phases are ultimately protected by TRS (whenever $v = 1$), WpG symmetry, or both, and are accordingly indexed. The index (last column) describes the part of wallpaper group that leaves the subset Γ_i having $\delta_i = -1$ invariant, while the additional label 'T' denotes TRS protection. In the column denoted "Phase" we introduce a convenient but imprecise shorthand notation.

case the C_4 rotational symmetry protects this phase, since it pins the band inversions at the X and Y points, and therefore represents a “valley” or “crystalline” [119] insulator – a phase trivial tenfold way-wise but protected by the lattice symmetries. Correspondingly, this new phase, which we dub the “ X - Y ” phase, can similarly be realized in an extension of the M - B model for a quantum spin Hall insulator when next-nearest neighbor hopping terms are incorporated, as shown in Fig. 4.1. Moreover, in accordance with the results of the previous Chapter, such a phase also responds non-trivially to dislocations and can therefore analogously be distinguished from the other phases due to the vectorial entity of the Burgers vector, see Appendix 4.B. When the C_4 rotational symmetry is reduced to C_2 , the X and Y points are no longer related by symmetry, and therefore the symmetry constraint on δ_X and δ_Y is no longer present. We then expect the X - Y phase to be unstable, and to yield instead non-trivial phases with $\delta_X = -1$ or $\delta_Y = -1$, and $\delta_i = 1$ at all other TRI momenta. Our calculations indeed confirm this within the M - B tight-binding model. In general, an even number of TRI momenta related by symmetry thus yields a valley or crystalline phase, protected by crystal symmetry while having $v = 0$, whereas in absence of this symmetry such a configuration renders a trivial phase.

Let us now elaborate on the role of the space group of the underlying lattice in this classification, since this symmetry group defines the relation between the high symmetry points. The difference in phases found on rectangular and rhombic lattices serves as a clear illustration. Both these lattices have D_2 point-group symmetry, but different wallpaper groups (space groups in 2D). The rhombic case has two inequivalent TRI momenta related by a point group symmetry and hence a valley phase, see Table 4.1. On the other hand, in the rectangular case all D_2 symmetry operations map any TRI momentum to its equivalent, thus no crystalline phase is possible. From Table 4.1 it is seen that in 2D the phases, as related to space groups, cluster in Bravais lattice classes, with one exception: the hexagonal lattice. We will see that this clustering is less generic in 3D. In turn, the primitive Bravais hexagonal (triangular) lattice ($p6mm$) is invariant under the C_6 rotational symmetry around a lattice site, as opposed to the non-primitive hexagonal lattice ($p3m1$) realized in graphene. Based on our rule, we conclude that in the latter case only the Γ phase is possible, which is in fact realized in the Kane-Mele model [31, 32]. In contrast, on the former lattice (triangular), the points K_+ and K_- are related by a C_6 symmetry and thus each of these points becomes TRI. The number of TRI momenta is henceforth increased, ultimately yielding a possibility of additional translationally-active and valley phases, as shown in Table 4.1 and Appendix 4.A.

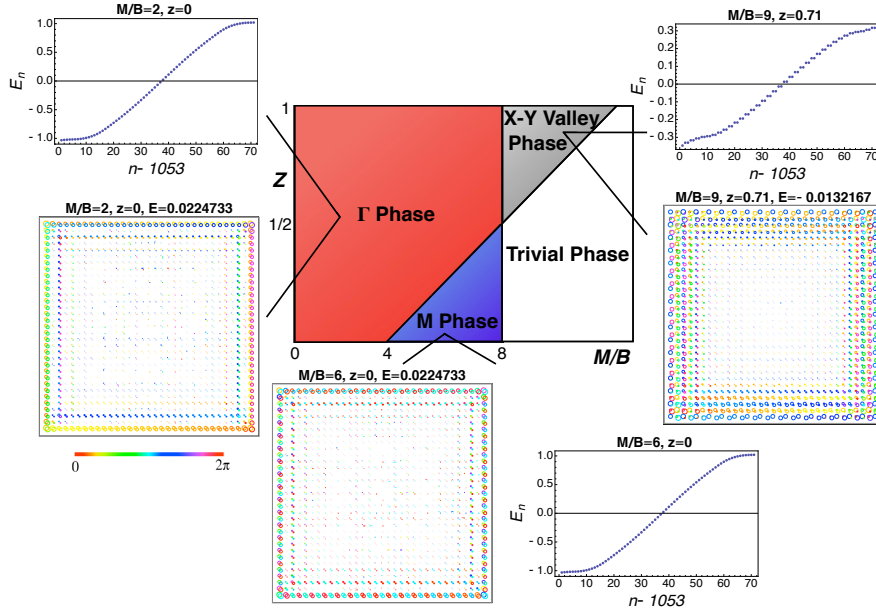


Figure 4.1: Phase diagram of the extended $M - B$ tight-binding model. As function of the model parameters M/B and $z = \tilde{B}/B$, where B (\tilde{B}) is the (next) nearest-neighbor hopping parameter and M the difference in on-site energies (Appendix 4.A), the different distributions of δ_i are obtained with the corresponding phases enlisted in Table 4.1. Furthermore, the spectra of edge states per spin component are displayed for the non-trivial phases, demonstrating that the valley X-Y phase exhibits a pair of Kramers pairs of metallic edge states. The real space localization of these edge states is also presented, where the radii of the circles represent the magnitude of the wave function and the colors indicate the phases as shown on the left.

The above rule allows us to completely classify and index the topological phases as conveyed by the last entry in Table 4.1. The set of BZ high-symmetry points Γ_i at which there is band inversion, i.e., $\delta_{\Gamma_i} = -1$, is invariant under the operations of a subgroup of the lattice space group. This symmetry subgroup therefore protects, and labels, the topological phase. The other element in this indexing is the protection by TRS (T), existing when the Z_2 invariant $\nu = 1$, giving, for instance $T - p4mm$ as the Γ phase on the square lattice. When the protecting symmetries coincide between phases, we explicitly label Γ_i (lower index), as, e.g., for $T - p2m_X$, $T - p2m_Y$ and $T - p2m_M$ phases on the rectangular lattice. This leads to the list of topological phases in 2D presented in Table 4.1 conveying 18 distinct topological phases. As our general result, we thus obtain two additional broad classes of topological states protected by TRS or crystalline symmetries, besides the class of states robust against general TRS perturbations (Γ -states): translationally-active states protected both by TRS and lattice symmetry, responding to dislocations, and valley insulators which are tenfold-way-wise trivial but protected by space group symmetry and also susceptible to dislocations.

Bravais Lattice	PGS	SG	Γ_i	δ_i	Index (Phase)
Primitive Cubic	O_h	$pm\bar{3}m$	(Γ, R, X, M)	$(-1, 1, 1, 1)$	$T-pm\bar{3}m (\Gamma)$
		$pn\bar{3}n$		$(1, -1, 1, 1)$	$T-p3(4)_R (R)$
		$pn\bar{3}m$		$(1, 1, -1, 1)$	$T-p3(4)_X (XYZ)$
		$pm\bar{3}n$		$(1, 1, 1, -1)$	$T-p3(4)_M (MX'Y')$
Hexagonal	C_{6v}	$p6mm$	(Γ, M, A, L, K, H)	$(-1, 1, 1, 1, 1, 1)$	$T-p6mm (\Gamma)$
		$p6cc$		$(1, -1, 1, 1, 1, 1)$	$T-p6_M (M)$
		$p6_3cm$		$(1, 1, -1, 1, 1, 1)$	$T-p6_A (A)$
		$p6_3mc$		$(1, 1, 1, -1, 1, 1)$	$T-p6_L (L)$
				$(-1, 1, 1, 1, 1, -1)$	$T-p6_{\Gamma H} (\Gamma H)$
				$(1, -1, 1, 1, 1, -1)$	$T-p6_{HM} (MH)$
				$(1, 1, -1, 1, -1, 1)$	$T-p6_{KA} (KA)$
				$(1, 1, 1, -1, -1, 1)$	$T-p6_{LK} (LK)$
				$(1, 1, 1, 1, -1, 1)$	$p6_K (K\text{-valley})$
				$(1, 1, 1, 1, 1, -1)$	$p6_H (H\text{-valley})$
Face Centered Cubic	O_h	$fm\bar{3}m$	(Γ, X, L, U, W)	$(-1, 1, 1, 1, 1, 1)$	$T-fm\bar{3}m (\Gamma)$
		$fm\bar{3}c$		$(1, -1, 1, 1, 1, 1)$	$T-f3(4) (X)$
		$fd\bar{3}m$		$(1, 1, -1, 1, 1, 1)$	$f3(4) (L\text{-valley})$
		$fd\bar{3}c$		$(1, 1, 1, -1, 1, 1)$	$f43_U (U\text{-valley})$
				$(1, 1, 1, 1, -1, 1)$	$f43_W (W\text{-valley})$
Rhombohedral	D_{3d}	$r\bar{3}m$	$(\Gamma, L, F, Z, P, K, B)$	$(-1, 1, 1, 1, 1, 1, 1)$	$T-r\bar{3}m (\Gamma)$
		$r\bar{3}c$		$(1, -1, 1, 1, 1, 1, 1)$	$T-r\bar{3}_L (L)$
				$(1, 1, -1, 1, 1, 1, 1)$	$T-r\bar{3}_F (F)$
				$(1, 1, 1, -1, 1, 1, 1)$	$T-r\bar{3}_Z (Z)$
				$(1, 1, 1, 1, -1, 1, 1)$	$r\bar{3}_P (P\text{-valley})$
				$(1, 1, 1, 1, 1, -1, 1)$	$r\bar{3}_K (K\text{-valley})$
				$(1, 1, 1, 1, 1, 1, -1)$	$r\bar{3}_B (B\text{-valley})$

Table 4.2: Topological phases anticipated in 3D for some specific point group (PG) symmetries. Bravais lattices with same PG symmetries have different space groups (SG). We point out that, in contrast to the 2D case, the phases do not cluster in Bravais lattice structures. For example, the fourfold rotational symmetry crucial for the $f43_U$ and $f43_W$ phases is not contained in every space group associated with the face centered cubic lattice. As δ_i 's attain the same value at the points Γ_i related by lattice symmetry or a reciprocal lattice vector, only one representative is given from each set of such points. We note that the rhombohedral $T-r\bar{3}_L$ phase is observed in Bi_xSb_{1-x} [42, 125], while the $T-r\bar{3}m$ phase is found in Bi_2Se_3 [43] and Bi_2Te_3 [44]. Moreover, the $fm\bar{3}m - f3(4)$ phase has recently been observed in Pb-doped SnTe [126, 127].

4.1.1 Three spatial dimensions

Our procedure can be applied in the same way in 3D, albeit becoming more involved given the 230 space groups and the large number of high-symmetry points. We find at least 70 different phases. Here we will illustrate matters for a number of simple crystal structures (Table 4.2) which include those of TBIs that are of present empirical relevance [42, 43, 44, 125]. In particular, consider the primitive cubic lattice (Table 4.2) with the familiar eight TRI points (Fig. 4.2A). Crucially, the points (X, Y, Z) are related by a three-fold rotation, as well as the points (X', Y', M) . Consequently, we obtain four TRS protected phases. We notice that this is quite different from the indexing procedure introduced by Moore and Balents [39]. For instance, our $T - pm\bar{3}m(\Gamma)$ and $T - p3(4)_R$ (R) phases correspond with their $(1; 0, 0, 0)$ and $(1; 1, 1, 1)$ indices, respectively. Their latter two indices would, however, also correspond with the $T - p3(4)_M$ and $T - p3(4)_X$ phases. The other possibilities in their classification are either coincident with our four TBIs, or represent a 3D phase not protected by crystal symmetries due to implicit dimensional reduction (e.g. layered 3D lattice); see Figs. 4.2A,B.

The power of the space group classification becomes further manifest for non-cubic lattices. Consider the 3D hexagonal lattice which consists of two hexagonal layers with the wallpaper group $p6mm$ stacked on top of each other. The TRI momenta comprise two copies of the ones on the 2D hexagonal lattice, separated by a perpendicular translation. Accordingly, the phases can easily be obtained by considering the $k_z = 0$ plane (Table 4.1), which contains the Γ , M and K points, and those of the other translated plane associated with the points A , L and H , respectively (Table 4.2). Consequently, there are eight TRS protected phases resulting from the combinations of a TRS protected phase in one plane and a trivial or a valley configuration in the other plane. Additionally, there are two valley phases which are configurations with one plane featuring a valley phase and the other a trivial configuration. Notice that a potential double valley phase with a valley phase in each of the planes is not protected by a 3D crystal symmetry and is therefore trivial. We again point out in this regard that the truly 3D crystalline phase is determined by a three-dimensional point group, i.e., the one whose action cannot be reduced to the 2D case.

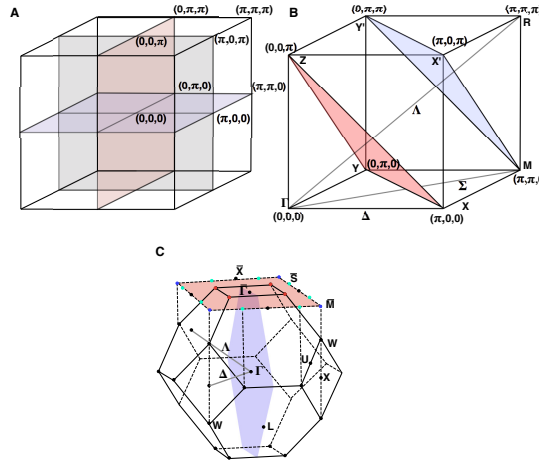


Figure 4.2: *Illustration of the role of lattice symmetries in the classification of topological states. (A) The eight TRI momenta in the Brillouin zone of the primitive cubic lattice. When only TRS is considered the sign of any quadruple of δ_i 's within a plane connecting them can be changed, leaving their product the same. As a result one obtains, in addition to the 'strong' invariant, three weak invariants corresponding to the orthogonal planes. (B) The constraints on the δ_i 's arising from the lattice symmetries. The high symmetry axes Δ , Λ and Σ represent axes of four-, three- and two-fold rotations, respectively; these transform the TRI points in the colored planes into each other, and thus constrain the corresponding δ_i 's to be equal. (C) The Brillouin zone of the face centered cubic lattice with high symmetry points and a mirror plane that projects onto the $\bar{\Gamma}-\bar{X}-\bar{\Gamma}$ line in the (001) plane. The W-valley phase features Dirac cones along $\bar{\Gamma}-\bar{M}-\bar{\Gamma}$ and $\bar{\Gamma}-\bar{S}-\bar{\Gamma}$ lines, but not along $\bar{\Gamma}-\bar{X}-\bar{\Gamma}$ lines.*

4.2 Topological signatures in the Greens function structure

As an intriguing sidestep, we remark that in the explicit context of the above simple lattice regularized Dirac Hamiltonians, the \mathbb{Z}_2 topological order can be characterized from a complementary point of view, that reflects the fundamental bulk-boundary correspondence and in turn signifies the general space group classification. Specifically, it turns out that the local in-gap Green's functions $\mathbf{G}_0(\varepsilon, \mathbf{k}_\parallel, \mathbf{r}_\perp = 0)$, with \mathbf{r}_\perp the position perpendicular to a codimension-1 or -2 surface, only attains zeros in the topological regime. These zeros are a direct consequence of the fact that the systems features a band inversion and thus characterize the non-trivial \mathbb{Z}_2 order. Moreover, by taking projections of the Green's function onto different codimension-1 surfaces, one can then readily deduce the bulk TRI momentum at which the band inversion occurs, pertaining directly to the δ_i configuration of the space group classification.

To make this concrete, we revert to the models of the form of Equations (2.7) and (2.8),

$$H_0 = d_\mu(\mathbf{k})\gamma^\mu, \quad (4.4)$$

where Γ^μ are the 4×4 Dirac matrices with the σ and τ Pauli matrices acting in the spin and orbital space, respectively, and $\mu = 0, 1, 2, 3$. Specifically, we choose $\gamma^0 = \sigma_0 \otimes \tau_3$ and $\gamma^i = \sigma_i \otimes \tau_1$. Recall, that time reversal symmetry (TRS) then implies that $d_0(\mathbf{k})$ must be an even and $d_i(\mathbf{k})$ must be an odd function of momentum. Focusing on the cases that $d_0(\mathbf{k}) = M - 2B\sum_i(1 - \cos(k_i))$ and $d_i(\mathbf{k}) = \sin(k_i)$, we then retrieve the familiar $M - B$ models in two and three spatial dimensions.

As a next step, consider a codimension-1 surface, having only one perpendicular direction $r_\perp = 0$. The corresponding simple real frequency Green's function in the gap,

$$\mathbf{G}_0(\omega, \mathbf{k}) = \frac{1}{\omega - d_\mu(\mathbf{k})\gamma^\mu} = \frac{\omega \mathbf{1}_4 + d_\mu(\mathbf{k})\gamma^\mu}{\omega^2 - |d(\mathbf{k})|^2}, \quad (4.5)$$

is then readily integrated over the associated perpendicular momentum. Moreover, the according result can subsequently be decomposed in terms of

$$g_\mu(\varepsilon, \mathbf{k}_\parallel) = \int \frac{dk_\perp}{2\pi} \frac{d_\mu(\mathbf{k}_\parallel, k_\perp)}{\varepsilon^2 - |d(\mathbf{k}_\parallel, k_\perp)|^2} \quad (4.6)$$

and

$$g(\varepsilon, \mathbf{k}_\parallel) = \int \frac{dk_\perp}{2\pi} \frac{\varepsilon}{\varepsilon^2 - |d(\mathbf{k}_\parallel, k_\perp)|^2}, \quad (4.7)$$

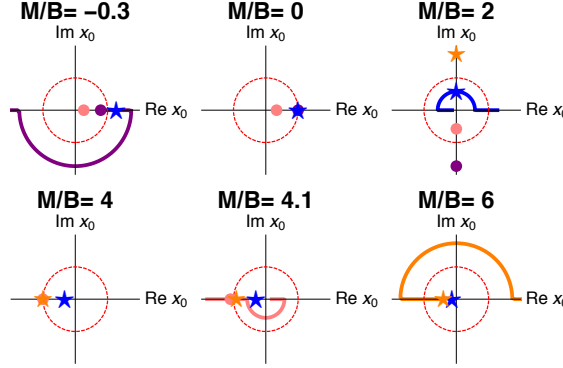


Figure 4.3: The flow of the poles of Eq. (4.9) as function of M/B . The two negative residue poles are indicated with a dot, whereas the stars mark the poles having a positive residue. In the trivial system, two poles with either positive or negative residue are located inside the red unit circle. For $M/B = 0, 4$ there are two poles with opposite residue located on the unit circle, signaling the transition. The topological phase is characterized by two poles of opposite residue in the unit circle. Finally, the solid lines illustrate the curves of the poles for increasing M/B .

so that $\mathbf{G}_0(\varepsilon, \mathbf{k}_{\parallel}, r_{\perp} = 0) = g(\varepsilon, \mathbf{k}_{\parallel})\mathbf{1} + g_{\mu}(\varepsilon, \mathbf{k}_{\parallel})\gamma^{\mu}$. This form shows that for any TRI point of the parallel momentum, for example $\mathbf{k}_{\parallel} = 0$ or $\mathbf{k}_{\parallel} = \pi$, the g_{\parallel} components equate to zero. As a result, since the g_{\perp} term also vanishes by virtue of the integrand being an odd function of k_{\perp} , we thus conclude that we only need to evaluate the projections g_0 and g at TRI points. Moreover, it is noteworthy to observe that these considerations still hold in the presence of, for example, Rashba spin orbit coupling terms, that are odd functions of the momentum. In particular, as such Rashba terms remove the particle hole symmetry of the original Hamiltonian and similar terms can be introduced to eliminate the inversion symmetry, the subsequent results can therefore also be verified in the absence of any other symmetry but time reversal symmetry.

Let us now show that the eigenvalues of the in-gap Green's functions $\mathbf{G}_0(\varepsilon, \mathbf{k}_{\parallel}, r_{\perp} = 0)$ only comprise zeros in the topological regime. As a first step, we note that the denominator in the integrand, $\varepsilon^2 - |d|^2$, is always negative. In the trivial phase $d_0(\mathbf{k})$ does not change sign throughout the Brillouin zone, implying that $g_0(\varepsilon)$ does not change sign. Additionally, since $\varepsilon < |d_0(\mathbf{k})|$, we furthermore deduce that $g(\varepsilon) + |g_0(\varepsilon)| > 0$ and $g(\varepsilon) - |g_0(\varepsilon)| < 0$. Hence, it is evident that the boundary Green's function

$\mathbf{G}_0(\varepsilon, \mathbf{k}_\parallel, r_\perp = 0)$ never has an eigenvalue equal to zero for all momenta \mathbf{k}_\parallel and energies ε in the trivial phase. On the other hand, in the topological phase, when \mathbf{k}_\parallel equates to the projection \mathbf{k}_S of the TRI point Γ_I hosting a band inversion in the sense of the above classification principle, the Green's function satisfies $\mathbf{G}_0(\varepsilon = 0, \mathbf{k}_\parallel = \mathbf{k}_S, r_\perp = 0) = 0$. To prove this, we evaluate

$$\begin{aligned} g_0(0, \mathbf{k}_S) &= - \int_{-\pi}^{\pi} \frac{dk}{2\pi} \frac{d_0(k, \mathbf{k}_S)}{|d^2(k, \mathbf{k}_S)|} \\ &= - \int_{-\pi}^{\pi} \frac{dk}{2\pi} \frac{\hat{M}(\mathbf{k}_S) - 2B(1 - \cos k)}{\sin^2 k + (\hat{M}(\mathbf{k}_S) - 2B(1 - \cos k))^2}, \end{aligned}$$

where $\hat{M}(\mathbf{k}_S) = M - 2B \sum_{i=1}^{D-1} (1 - \cos(k_i))$, in terms of the coordinates \mathbf{k}_S and the spatial dimension D . Substituting $x = e^{ik}$, the integral turns into a contour integral over the unit circle of the form

$$\frac{1}{2\pi i} \oint_{|x|=1} dx \frac{B + (\hat{M} - 2B)x + Bx^2}{f(x)}, \quad (4.8)$$

with $f(x) = (\frac{1}{2} + 6B^2 - 4B\hat{M} + \hat{M}^2)x^2 + 2B(\hat{M} - 2B)x(x^2 + 1) + (B^2 - \frac{1}{4})(x^4 + 1)$, the resulting expression of which can directly be solved upon application of the Cauchy residue theorem. Specifically, the poles are located at, see Fig. (4.3),

$$x_0 = \frac{2B - \hat{M} \pm \sqrt{1 - 4B\hat{M} + \hat{M}^2}}{2B \pm 1}. \quad (4.9)$$

When the system becomes gapless for $\hat{M} = 0$ or $\hat{M} = 4B$, we find that there are two zero's located *on* the unit circle. Consequently, from the analytic structure of the integral we already infer that the regime $0 < \hat{M} < 4B$ is topologically distinct from $\hat{M} < 0$ and $4B < \hat{M}$. Focusing on the topological phase $0 < \hat{M} < 4B$, a straightforward evaluation shows that the residues of the two zeroes $x_{0,\pm} = \frac{2B - \hat{M} \pm \sqrt{1 - 4B\hat{M} + \hat{M}^2}}{2B \pm 1}$ located inside the unit circle cancel,

$$\text{Res}(x_{0,+}) + \text{Res}(x_{0,-}) = 0, \quad (4.10)$$

revealing that $g_0(\varepsilon = 0) = 0$ in the topological phase. Accordingly, when $\hat{M} < 0$ or $4B < \hat{M}$, representing the trivial regimes, the integral never equates to zero and together with the universal divergence of the both $g(\varepsilon)$ and $g_0(\varepsilon)$ at the band edges (see Appendix 4.C), we arrive at the generic description as shown in Fig. 4.4.

We thus observe that the number of zeros in the boundary Green's function relates to the underlying topological characterization. That is, the odd number of crossings per spin branch of $\mathbf{G}_0(\varepsilon, \mathbf{k}_\parallel, r_\perp = 0)$ with the zero eigenvalue axis is a topological property

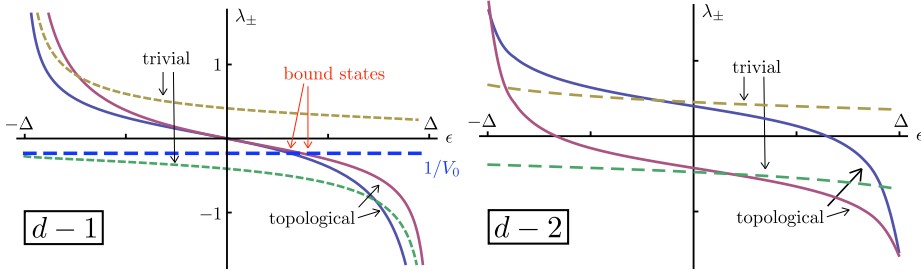


Figure 4.4: The eigenvalues of the local Green's function $\mathbf{G}_0(\epsilon, k_{\parallel} = 0, r_{\perp} = 0)$ in the M/B model corresponding with codimension-1 (left panel) and codimension-2 (right panel) surfaces. In the trivial system (dashed lines, $M/B = -1$) the eigenvalues λ_{\pm} are nonzero. In the topological system (solid line, $M/B = 1$) the eigenvalues are zero for some in-gap energy and hence in-gap bound states on codimension-1 and codimension-2 impurities always exist. The dashed line $1/V_0$ in the left panel graphically marks these bound state solutions of codimension-1 impurities.

[128, 129, 130, 131]. It reflects that in the non-trivial regime the system has an odd number of Kramers degenerate edge states on either side of the surface and hence may be regarded as a consequence of the bulk-boundary correspondence. In particular, the bulk TRS \mathbb{Z}_2 invariant for the above simple models is given by the product $\prod_{\Gamma_i} \xi_i$ of the parity γ_0 eigenvalues ξ_i over the TRI points in the Brillouin zone [38] and the two relevant poles have the same residues but multiplied by the sign of the mass, i.e. the parity γ_0 eigenvalues. For that reason, only if the choice \mathbf{k}_S in the projected plane is associated with two masses of opposite sign, meaning that this cut features a band inversion, the poles cancel in the above integral rendering a zero eigenvalue. This is in direct accordance with the space group classification.

For example, the two dimensional variant of Equation (4.4) exhibits a Γ ($T - p4mm$) phase for $0 < M/B < 4$ and a M ($T - p4$) phase for $4 < M/B < 8$. From the above considerations we find that \hat{M} has to satisfy $0 < \hat{M} < 4$ for $\mathbf{G}_0(\epsilon, k_{\parallel}, r_{\perp} = 0)$ to develop zero eigenvalues. Taking subsequently projections along the k_x and k_y directions and using that $\hat{M}(k_S) = M - 2B(1 - \cos(k_S))$, we thus conclude that in the Γ phase the k_S values exhibiting a zero eigenvalue correspond to projections of the inversion momentum $\Gamma_I = \Gamma$, whereas in the M phase they are associated with a bulk inversion $\Gamma_I = M$. We stress that this analysis still holds if we add Rashba terms, or other TRS perturbation

terms that are odd functions of momentum. Similarly, when we add the next nearest neighbor term (Appendix 4.A) to the Hamiltonian and tune the system into the $X - Y$ ($p4$) topological crystalline phase, the inversion momenta correspond with $\Gamma_I = X$ and $\Gamma_I = Y$ as conveyed by Table (4.1). An identical calculation then shows that the projections along k_x and k_y feature indeed zero eigenvalues of $\mathbf{G}_0(\varepsilon, k_{\parallel}, r_{\perp} = 0)$ for *both* $k_S = 0$ and $k_S = \pi$. These principles are exemplified in the three dimensional instances in the exact same fashion. Considering for example a Γ ($T - pm\bar{3}m$) phase featuring an inversion at $\Gamma_I = \Gamma$ for $0 < M/B < 4$, it is evident that \mathbf{k}_S corresponds with $(0, 0)$ in any of the planes normal to the principle axes.

The above results on the structure of the eigenvalues of $\mathbf{G}_0(\varepsilon, k_{\parallel}, \mathbf{r}_{\perp} = 0)$ in the codimension-1 case can similarly be extended to codimension-2 surfaces (Fig. (4.4)). Specifically, also in the latter instance the associated local in-gap Green's function only attains zeros if and only if the system is in the topological phase, as detailed in the Appendix 4.C. Although, these zeros are no longer in direct correspondence with the space group classification due to second integration procedure, this result does provide for another experimental signature of the TRS induced \mathbb{Z}_2 invariant in the context of impurity bound states. Concretely, for an impurity defect that preserves translational symmetry along the parallel directions \mathbf{r}_{\parallel} , the defining eigenvalue equation determining the existence of in-gap bound states is given by [132, 133]

$$\det [\mathbf{G}_0(\varepsilon, \mathbf{k}_{\parallel}, \mathbf{r}_{\perp} = 0) \mathbf{V}_0 - \mathbf{1}] = 0, \quad (4.11)$$

where V_0 is the specific form of the impurity. As a result, considering an impurity of the form

$$V(\mathbf{r}) = \mathbf{V}_0 \delta_{\mathbf{r}_{\perp}=0}^n, \quad (4.12)$$

we observe that in the topological phase a codimension-1 or -2 impurity will always result in a in-gap bound state, whereas in the trivial regime this depends on the details [133]. Accordingly, one could imagine a two-dimensional insulator, where at one isolated point a tunable gate voltage is applied, serving as the impurity potential V . Then using tunneling spectroscopy, the possible bound states around this impurity can readily be identified. However, upon increasing the impurity potential V , the energies of the bound states will shift and for a trivial insulator one can make the bound states disappear into one of the bands for a sufficiently strong potential. In contrast, for a topological insulator the above shows that for all V there will always be two in-gap bound states (Fig. 4.5), providing for a clear indication of the non-trivial \mathbb{Z}_2 invariant.

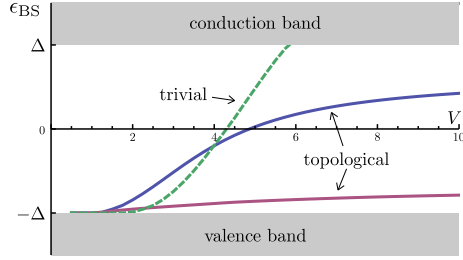


Figure 4.5: *Typical energy of impurity bound states in a two-dimensional insulator as a function of impurity strength V . Here, we discern between the topological regime (solid lines, $M/B = 1$) and the trivial regime (dashed line, $M/B = -1$). For strong V , bound states in the trivial phase have disappeared in the conduction band, whereas the bound states in the topological phase remain.*

4.3 The space group classification as an experimental guide

Let us now return to the general classification scheme and discuss its relevance in the scenery of experimentally viable TBIs. A lot of observed TBIs, including the second generation Bi-based materials Bi_2Se_3 [43] and Bi_2Te_3 [44], are of the Γ kind. Nonetheless, the compound which initiated the 3D pursuit, $\text{Bi}_x\text{Sb}_{1-x}$, is a non- Γ TBI, characterized by $r\bar{3}m - T - r\bar{3}_L$ [42, 125]. Similarly, the theoretically predicted rock-salt actinides [134] are associated with the translationally-active class and exemplify a $fm\bar{3}m - T - f3(4)$ phase. Furthermore, the predicted valley or crystalline class found recent experimental verification in the form of Pb-doped SnTe [126, 127]. Most interestingly, this latter system has the exact same space group, $fm\bar{3}m$, as the actinides. Hence, we are directly confronted with the effective working of the space group classification. Given the specific crystal symmetry group, one directly obtains the possible phases as conveyed by Table (4.2).

As a final demonstration of the general principle, let us consider the latter valley phase, indexed by $fm\bar{3}m - f3(4)$, in more detail. This system features mirror planes in the momentum space formed by the Γ and any two of the L points, which thereby relate the remaining two L points by symmetry. As a result, a mirror-symmetric crystal cut along $\bar{\Gamma} - \bar{X} - \bar{\Gamma}$ line in the (001) surface exhibits a pair of Dirac cones (a double

Dirac cone) which is therefore also protected by the same symmetry [120]. Notice that in addition we predict valley phases at the W and the U points in the Brillouin zone protected by both the four-fold and the three-fold rotational symmetries, labelled by $fm\bar{3}m - f43_W$ and $fm\bar{3}m - f43_U$, respectively. The W -phase originates from six inequivalent symmetry-related W -points in the BZ where a band inversion gives rise to a valley phase. In addition, in the same phase, the (001) surface features Dirac cones for the cut along $\bar{\Gamma} - \bar{M} - \bar{\Gamma}$ and $\bar{\Gamma} - \bar{S} - \bar{\Gamma}$ lines, but not along $\bar{\Gamma} - \bar{X} - \bar{\Gamma}$ direction, as it is the case in the $fm\bar{3}m - f3(4)$ phase, see Fig.4.2(C). Therefore, the detection of the Dirac cones in the $\bar{\Gamma} - \bar{M} - \bar{\Gamma}$ and $\bar{\Gamma} - \bar{S} - \bar{\Gamma}$ directions in ARPES experiments would be a clear signature of this valley phase.

4.4 Conclusions

In conclusion, we provided the space group classification of topological band insulators in both in two and three spatial dimensions. As a main result, this classification scheme identifies two additional broad classes of topological phases, besides the TRS protected Γ states: translationally-active phases, protected by both TRS and crystal symmetries, but susceptible to topological crystalline disorder, and valley phases solely protected by the space group symmetry, and therefore susceptible to both elastic and topological crystalline disorder. These classes correspond directly to the results of the previous Chapter and can similarly be probed by dislocations. Furthermore, a non-trivial characterization of the bulk also leads to a distinct zeros in the Green's function structure associated with codimension-1 surfaces, which in fact is a consequence of the bulk-boundary correspondence. The resulting pattern of projected zeros resultantly indicates the space group classification from a complementary perspective. Finally, our complete classification scheme based on the full 2D and 3D space groups has as most important experimental consequence that it demonstrates the potential existence of at least seventy distinct topological phases of insulating matter and we anticipate that this will be a valuable guide in the future exploration of this landscape.

4.A Verification within M-B model setting

The above general notions can directly be corroborated within the specific setting of the previous Chapters. Let us therefore for concreteness illustrate the general principles in this context. In particular, it is straightforward to generalize the $M - B$ model eq. (3.41) to the five Bravais structures in two spatial dimensions. The connection to the above characterization is then readily achieved by noting that the Pfaffian expression relates to the band-structure vector $\mathbf{d}(\mathbf{k})$ of Eq. (3.37) through $\delta_i = \text{sign}[d_3(\Gamma_i)]$.

In case of the square lattice, the C_4 rotation connects the δ_i 's and thus dictates that the values at the X and Y points have to be the same. In addition to the Γ phase and M phase, the anticipated crystalline phase can then be established by incorporating a next nearest neighbor term with the parameters defined exactly as in the nearest neighbor case. Accordingly, we obtain

$$\mathbf{d}(\mathbf{k}) = \begin{pmatrix} \sin(k_x) + \cos(k_x) \sin(k_y) \\ -\sin(k_y) - \sin(k_x) \cos(k_y) \\ M - 2B[2 - \cos(k_x) - \cos(k_y)] - 4\tilde{B}[1 - \cos(k_x) \cos(k_y)] \end{pmatrix}. \quad (4.13)$$

The gap at the TRI momenta and hence the configuration of δ_i can be tuned as function of the parameters \tilde{B}/B and M/B resulting in the phase diagram shown in Fig. 4.1. Importantly, we find that the resulting valley phase features two pairs of edge states. Connecting to the intuitive skyrmion picture, it can similarly be shown that this phase exhibits two Skyrmions located at the X and Y points and that integration of the Skyrmion density accordingly yields a winding number that equates to two per spin.

As the next step, the rectangular model is obtained by making the magnitude of the hopping parameters anisotropic, which effectively reduces the fourfold rotational symmetry to a twofold symmetry, see also Appendix 4.B, Eq. (4.18). Consequently, the oppositely valued δ_i 's can be located at any of the TRI momenta Γ, M, X, Y , and the corresponding phases can be distinguished by insertion of dislocations (Appendix 4.B). We find that by increasing the ratio r of the hopping magnitudes in the y and x directions the valley phase is lost: the system either enters a trivial state, a translationally-active X phase or a phase with $C = 2$ per spin not protected by either TRS or lattice symmetry. Namely, only the former two phases are realized when the ratio r is large enough. The two edge modes per spin in the X - Y valley phase are gapped out upon an infinitesimal breaking of C_4 symmetry, i.e. by $r > 1$. The phase diagram of the model for $r = 2$ is

shown in Fig. 4.10.

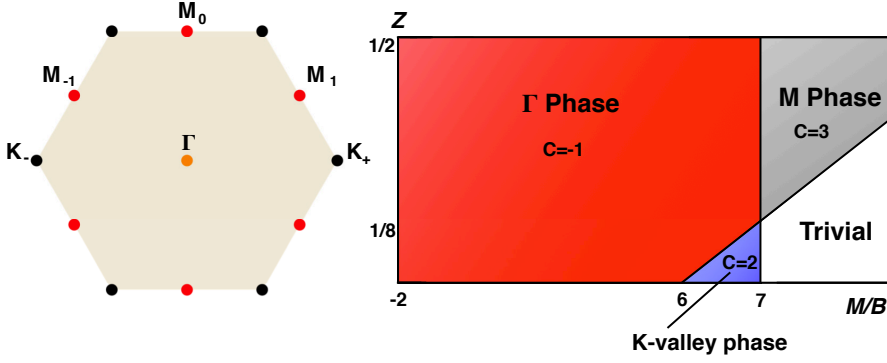


Figure 4.6: The Brillouin zone of the primitive hexagonal (triangular) lattice and the phase diagram of the M-B tight-binding model on the same lattice. High-symmetry points in the Brillouin zone at which the Hamiltonian commutes with the time-reversal operator are indicated. Additionally, the Chern number per spin block ($C = C_{\uparrow} = -C_{\downarrow}$) is shown for each phase.

In case of a primitive hexagonal (triangular) lattice with the wallpaper group $p6mm$, the nearest neighbor hopping part of the Hamiltonian is described by

$$\mathbf{d}(\mathbf{k}) = \begin{pmatrix} \sin k_x + 2 \sin(\frac{k_x}{2}) \cos(\pi/3) \cos(\frac{\sqrt{3}}{2} k_y) \\ -2 \cos(\frac{k_x}{2}) \sin(\pi/3) \sin(\frac{\sqrt{3}}{2} k_y) \\ M - 2B[2 - \cos k_x - 2 \cos(\frac{k_x}{2}) \cos(\frac{\sqrt{3}}{2} k_y)] \end{pmatrix} \quad (4.14)$$

As for the other Bravais lattices, the sign of the Pfaffian at the Γ_i points is given by $\delta_i = \text{sign}[d_3(\Gamma_i)]$ and we observe that due to the very presence of the lattice symmetry (C_6 in particular), δ_i is also well defined at the two inequivalent corners K_+ and K_- of the Brillouin zone (Fig. 4.6). Additionally, the symmetry relates the centers of the edges M and we thus expect the phases as indicated in the Table 4.1. The resulting Hamiltonian corresponding to the vector \mathbf{d} in (4.14) indeed exhibits the Γ and the K valley phase for $-2 < M/B < 6$ and $6 < M/B < 7$, respectively. The M phase can also be captured by including the next nearest neighbor hopping term

$$\tilde{\mathbf{d}}(\mathbf{k}) = \begin{pmatrix} \tilde{A} \sin(\frac{3}{2} k_x) \cos(\pi/6) \cos(\frac{\sqrt{3}}{2} k_y) \\ -\tilde{A} [\sin(\sqrt{3} k_y) - 2 \cos(\frac{3}{2} k_x) \sin(\pi/6) \sin(\frac{\sqrt{3}}{2} k_y)] \\ -2\tilde{B} [3 - \cos(\sqrt{3} k_y) - 2 \cos(\frac{3}{2} k_x) \cos(\frac{\sqrt{3}}{2} k_y)] \end{pmatrix}. \quad (4.15)$$

For strong enough next-nearest neighbor hopping, $z = \tilde{B}/B > \frac{1}{8}$, the gap closes at the K points before closing at the M points for increasing M/B and as a result the system exhibits a Γ and M phase, see Figs. 4.6 and 4.7. We note that we need *six* inequivalent high symmetry points, marked in Fig. 4.6, to capture the three observed phases within the rule presented in the main text. In contrast, the symmetry relating K_+ and K_- can readily be broken by considering a non-primitive honeycomb lattice structure, realized in graphene, which then makes K_{\pm} *related* by TRS. The Hamiltonian does not commute with the time-reversal operator at these points, and therefore, these two points no longer belong to the set Γ_i . As the M points are still related by symmetry, we expect only a Γ phase in this case. A prominent example is the Kane-Mele model [32] with the configuration of δ_i 's explicitly calculated in Ref. [38] using a rhombic unit cell. Drawing this cell in the extended BZ we observe that this configuration indeed corresponds with a Γ phase in the usual Wigner-Seitz cell. Additionally, the result can also be understood from the Skyrmion picture. Due to inversion-asymmetry the gap closes at K_{\pm} points instead of closing at the TRI momenta [135, 136]. The spin sub-blocks exhibit merons at K_+ and K_- points which can be explicitly shown by rewriting the Pontryagin index as in Ref [137].

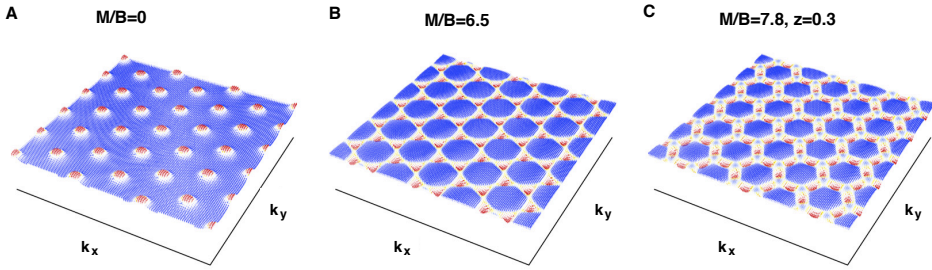


Figure 4.7: The skyrmion lattices in the extended Brillouin zone for the three topological phases on the primitive hexagonal (triangular) lattice. The locus of the Skyrmions is colored in red. (A) The Skyrmion lattice for the Γ phases within the M - B model. (B) K valley phase within the same model. (C) When next nearest neighbor hopping, $z = \tilde{B}/B$, is taken into account, the system can enter the M phase, which has the Skyrmions positioned at the M points.

Finally, we consider the oblique and rhombic Bravais structures distinguished by the presence of mirror symmetry in the latter case. This symmetry is ultimately responsible for the existence of the valley phase on the rhombic lattice. Considering the rhombic lattice, it can be readily shown that

$$\mathbf{d}(\mathbf{k}) = \begin{pmatrix} A_1 \cos(\phi_1) \sin(\tilde{k}_x) \cos(\tilde{k}_y) + A_2 \sin(r_1 k_x) \\ -A_1 \sin(\phi_1) \sin(\tilde{k}_x) \cos(\tilde{k}_y) - A_3 \sin(r_2 k_y) \\ M - 4B[1 - \cos(\tilde{k}_x) \cos(\tilde{k}_y)] + 2\tilde{B}[\tau_1^{-1} + \tau_2^{-1} - \tau_1^{-1} \cos(r_1 k_x) - \tau_2^{-1} \cos(r_2 k_y)] \end{pmatrix}, \quad (4.16)$$

where $\tilde{k}_x = e_1 \cos(\phi_1) k_x$, $\tilde{k}_y = e_1 \sin(\phi_1) k_y$, with ϕ_1 being the polar angle of the vector \mathbf{e}_1 , and $e_1 = |\mathbf{e}_1|$; see Fig. 4.8. Furthermore, A_i is the hopping between the s and the p orbitals along the vector \mathbf{e}_i , while B is the hopping between the two s orbitals along the vector \mathbf{e}_1 , and the hopping between these orbitals along the vectors $\mathbf{e}_{2,3}$ is $B_{2,3} = \tilde{B} \tau_{2,3}^{-1}$. Due to the mirror symmetry, the M_{-1} and M_1 points are connected and as a result the gap closes at these points for the same value of M/B . Consequently, tuning the gaps at the TRI momenta by varying the parameters of the model, the configurations of δ_i 's and the corresponding phases shown in Table 1 in the main text are easily obtained. The

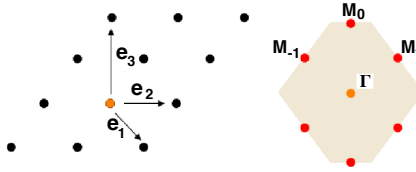


Figure 4.8: The left panel shows the real space rhombic lattice with the vectors connecting the neighbors. The right panel shows the corresponding Brillouin zone with the TRI momenta for $e_2 = |\mathbf{e}_2| = 3$ and $e_3 = |\mathbf{e}_3| = 4$ in arbitrary units. Crucially, the mirror symmetry connects the M_{-1} and M_1 points.

oblique lattice can be then treated similarly. Denoting the different connections between neighbors as indicated in Fig. 4.9, we obtain

$$\mathbf{d}(\mathbf{k}) = \begin{pmatrix} A_1 \cos(\phi_1) \sin(\mathbf{e}_1 \cdot \mathbf{k}) + A_2 \cos(\phi_2) \sin(\mathbf{e}_2 \cdot \mathbf{k}) + A_3 \cos(\phi_3) \sin(\mathbf{e}_3 \cdot \mathbf{k}) + A_4 \cos(\phi_4) \sin(\mathbf{e}_4 \cdot \mathbf{k}) \\ -A_1 \sin(\phi_1) \sin(\mathbf{e}_1 \cdot \mathbf{k}) - A_2 \sin(\phi_2) \sin(\mathbf{e}_2 \cdot \mathbf{k}) - A_4 \sin(\phi_4) \sin(\mathbf{e}_4 \cdot \mathbf{k}) \\ M - 2B[2 - \tau_1^{-1} \cos(\mathbf{e}_1 \cdot \mathbf{k}) - \tau_2^{-1} \cos(\mathbf{e}_2 \cdot \mathbf{k}) - \tau_3^{-1} \cos(\mathbf{e}_3 \cdot \mathbf{k}) - \tau_4^{-1} \cos(\mathbf{e}_4 \cdot \mathbf{k})] \end{pmatrix}, \quad (4.17)$$

where the angles ϕ_i , $i = 1, \dots, 4$, are the polar angles of vectors \mathbf{e}_i . The $s - p$ hopping along the vector \mathbf{e}_i is A_i , and the $s - s$ hopping along the same vector is $B_i = B \tau_i^{-1}$.

Again, by varying the model parameters (consequently also the shape of the BZ), it is straightforward to realize the different phases which are also visualized by the presence of a Skyrmion at either of the indicated points. More interestingly, the analysis confirms yet again the significance of the symmetry group of the underlying crystal. Essentially, the only difference between the oblique and rhombic systems is the presence of the mirror symmetry. Therefore, the same $(1, 1, -1, -1)$ configuration of δ_i 's results in a valley phase with the Chern number equal two per spin block *only* when the mirror symmetry is present, i.e., only in the case of the rhombic lattice.

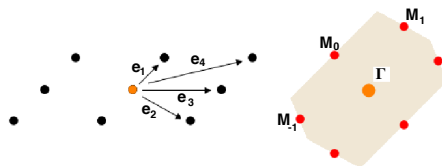


Figure 4.9: *The real space oblique lattice and its corresponding Brillouin zone. In contrast to the rhombic case, the TRI momenta are not related by a lattice symmetry. In this example, vectors \mathbf{e}_1 and \mathbf{e}_2 connect nearest-neighboring sites, while \mathbf{e}_3 and \mathbf{e}_4 connect next-nearest neighboring sites.*

4.B Probing the topologically non-trivial phases

As shown in the previous Chapter, a π -flux probes Z_2 topological order through the binding of the zero modes, while the dislocations act as universal probes of the translationally-active topological states. Although the generality of the above argument already implies analogous responses in accordance with the general space group classification, let us here demonstrate that indeed the same results hold within the extended M - B tight-binding model. In particular, focussing on the rectangular lattice model and the square lattice valley phase this then allows for motivation of the unique status of the dislocation directionality as a probe that distinguishes translationally-active and crystalline topological phases at different high symmetry points in the BZ.

The M - B tight-binding model on a rectangular lattice assumes the form (3.36) in terms of the vector

$$\mathbf{d}(\mathbf{k}) = \begin{pmatrix} \sin(k_x) + \frac{\tilde{A}}{\sqrt{1+\tau}} \cos(\varphi_r) [\sin(k_+) - \sin(k_-)] \\ -1/\tau \sin(rk_y) - \frac{\tilde{A}}{\sqrt{1+\tau}} \sin(\varphi_r) [\sin(k_+) + \sin(k_-)] \\ M - 2B[2 - \cos(k_x) - 1/r \cos(rk_y)] - 2\tilde{B}[2 - \cos(k_+) - \cos(k_-)] \end{pmatrix}, \quad (4.18)$$

where r denotes the ratio of the lattice spacing in the y and the x -direction, $\varphi_r = \arctan(r)$, $\tau = A_x/A_y = B_x/B_y$, and $k_{\pm} = \pm k_x + rk_y$. In the remainder we conveniently fix $r = \tau = 2$ and $\tilde{A} = 1$. The resulting phase diagram is presented in Fig. 4.10.

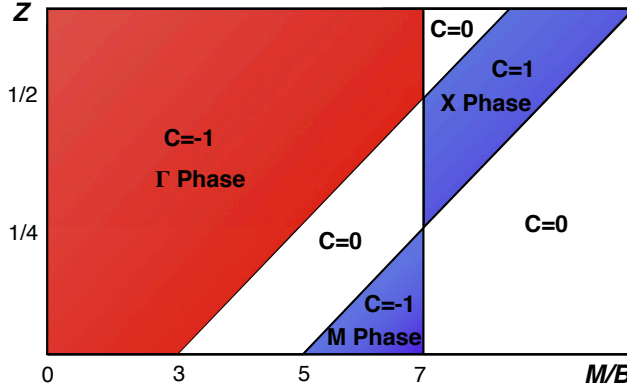


Figure 4.10: Phase diagram of the extended $M - B$ model on the rectangular lattice in Eq. (4.18) for $r = \tau = 2$ and $\tilde{A} = 1$. The non-trivial phases include the Γ , M and a X phases. Additionally, the Chern character C per spin, $C = C_{\uparrow} = -C_{\downarrow}$ is indicated.

Considering first only nearest neighbor hopping, the non-trivial phases on both the square and rectangular lattices include the Γ and M phases. Accordingly, we find that the M phase gives rise to a dislocation zero-mode, whereas a π flux results in a zero-mode in both the Γ and the M phase (Fig. (4.11)). The dislocation zero mode hybridizes with the low-energy edge states in a finite system. Separating these states by introducing weak disorder via a random chemical potential, we confirm that the edge state indeed pertains to the finite momentum $k = \pi$.

The next nearest neighbor hopping, as already shown, realizes the valley phase on the square lattice (Fig. (4.1)). As anticipated, introduction of a magnetic π flux results in a *double* Kramers pairs of zero modes in the system. More interestingly, the

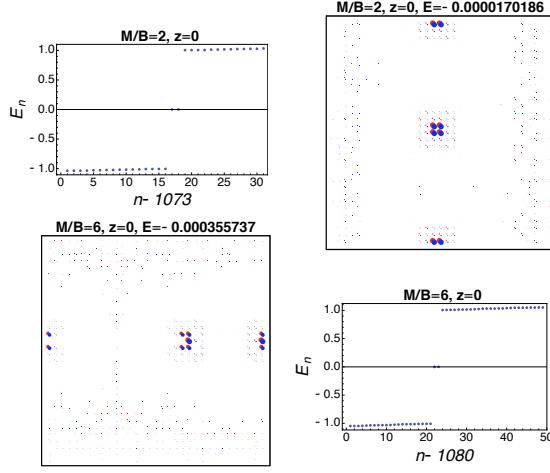


Figure 4.11: *Effect of introducing a π flux or dislocations in the Γ and M phase of the square lattice model. The top row shows two zero-modes bound to π -anti- π flux pair (periodic boundary conditions) appearing in the spectrum in case of the Γ phase and the real space localization of these modes. For convenience we only consider one spin component. The bottom row shows the effect of a dislocation-anti-dislocation pair (periodic boundary conditions) with Burgers vector $\mathbf{b} = \mathbf{e}_y$ in the M phase. The lattices contain 33×33 unit cells.*

bulk-boundary correspondence and the directional character of a dislocation result in the possibility of discriminating between the two valley points. Namely, a dislocation with Burgers vector \mathbf{b} along the \hat{x} or \hat{y} direction binds only a *single* pair of zero-energy modes. Analysis of the edge state hybridized with the dislocation zero-mode then confirms that the dislocation indeed corresponds with the valley at the momentum parallel to the direction of the Burgers vector (Fig. 4.12).

When r is increased (breaking square symmetry to rectangle), the Chern number per spin block may reduce to zero and insertion of a π -flux or a dislocation no longer results in a zero-mode in the system, confirming the intimate relation between the point group lattice symmetry and the valley phase. As the parameter r is increased, another possibility is a topological phase transition to the X phase which does not respect the fourfold symmetry and thus distinguishes the square from the rectangular lattice. This is reflected in the response of the system upon the insertion of dislocations. In addition

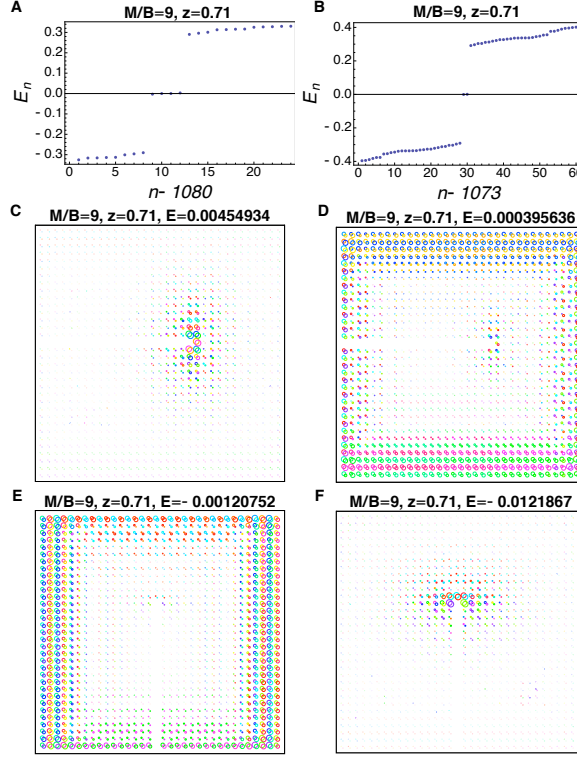


Figure 4.12: *Probing the X – Y valley phase, by considering one spin component of each Kramers pair. (A) Spectrum in presence of a π -flux and anti- π -flux in a periodic system. (B) Spectrum in case of a dislocation and anti-dislocation in a periodic system. (C) Real space localization of zero-mode resulting from a single dislocation with Burgers vector $\mathbf{b} = \mathbf{e}_y$. (D) The phase of the edge state hybridized with the dislocation zero mode displayed in (C), shows that it is a mode from the Y point, $\mathbf{k} = (0, \pi)$. Similarly, the dislocation zero-mode displayed in (F) hybridizes with edge state shown in (E), the phases of which indicate that this zero-energy state corresponds with the X point, $\mathbf{k} = (\pi, 0)$. Color-code is as in Fig. 4.1. The lattices contain 33×33 unit cells.*

to the usual zero-energy modes resulting from a π -flux vortex, the spectrum shows a Kramers pair of zero-modes resulting from dislocations only if the Burgers vector \mathbf{b} has a component in the x direction (Fig. 4.13).

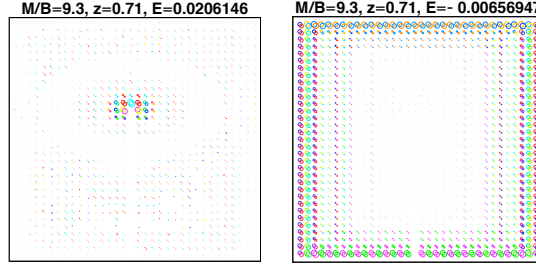


Figure 4.13: *Illustration of the zero-mode bound to a dislocation appearing in the X phase decoupled from the edge states using linear combinations (left panel). The right panel shows the edge state, the phases of which indicate that these edge states indeed correspond with the X point (color-code as in Fig. 4.1). The lattice contains 30×33 unit cells.*

Let us conclude by addressing the robustness of the zero-modes in the topological non-trivial regimes, which is related to the stability of the corresponding phase. To this end, we multiply all the model parameters by Gaussian variables of width $w = 10\%$ and also introduce Gaussian random chemical disorder, while preserving TRS. Moreover, we couple the spin-reversed sub-blocks by adding the familiar nearest neighbor Rashba spin-orbit coupling

$$H_R = i \frac{R_0}{2} \sum_{\mathbf{R}, \boldsymbol{\delta}} \Psi_{\mathbf{R}}^\dagger [(\tau_0 + \tau_3) \otimes (\boldsymbol{\sigma} \times \boldsymbol{\delta}) \cdot \mathbf{e}_z] \Psi_{\mathbf{R} + \boldsymbol{\delta}} \quad (4.19)$$

to the original Hamiltonian, which breaks the reflection symmetry $z \rightarrow -z$ about the plane. The results are displayed in Fig. 4.14. We find that finite Rashba spin orbit coupling, but not large enough to close the topological gap, preserves the real space localization of the mid gap modes. More importantly, we observe that the stability of the modes in the valley phase is significantly smaller than in the Z_2 non-trivial phases. We note that the latter phase has a smaller gap and hence would already require a weaker Rashba coupling to close the gap. However, one would expect the valley phase to be less stable independently of the gap size, as only the lattice symmetry accounts for its protection. To check this assertion, we also considered the valley phase in presence of a stronger next nearest neighbor hopping, which leads to an increase of the gap size. This analysis then confirms that the zero-modes in the valley phase are substantially less robust than those in the TRS protected phases. That is, the disordering terms close the

gap for smaller values in magnitude.

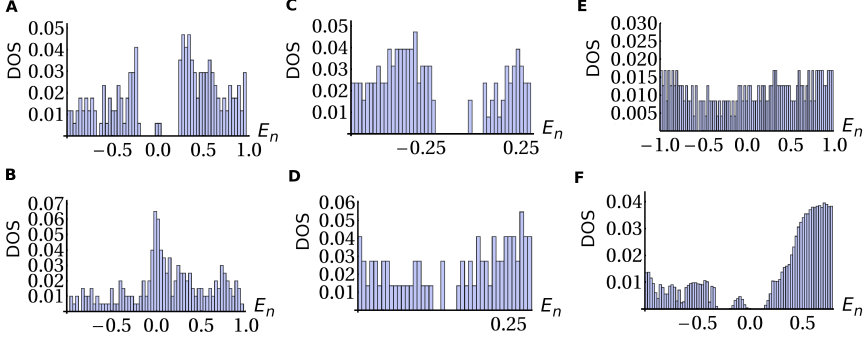


Figure 4.14: *The averaged (over 130 disorder realizations) density of states (DOS) for various values of M/B , $z = \tilde{B}/B$ and $R = R_0/B$. Panels (A)-(B) and (D)-(E) correspond to the square lattice model, whereas panel (C) corresponds to the rectangular case. The midgap modes resulting from dislocations are present even for strong Rashba coupling and disorder, as demonstrated by (A) $R = 1.5$ in the M phase, (B) $R = 0.5$ in the $X - Y$ valley phase and (C) $R = 1.5$ in the X -phase. Sufficiently strong Rashba coupling closes the topological gap, as shown for (D) $R = 2$ in the M phase (a similar result is obtained for the X -phase) and (E) $R = 1$ in the $X - Y$ valley phase. Even for comparable values of the bulk gap, the valley phase is substantially less robust to the Rashba coupling than the TRS protected M and X phases.*

4.C Topological signatures in the Greens function structure

In this Appendix, we provide some details regarding the evaluation of the Greens functions associated with codimension-1 and codimension-2 surfaces.

4.C.1 Details codimension-1 case

We have shown in the main text that $\mathbf{G}_0(\varepsilon = 0, \mathbf{k}_{\parallel} = \mathbf{k}_S, \mathbf{r}_{\perp} = 0) = 0$ only acquires zero eigenvalues in the topological regime. Here, we elaborate on the generic structure which results in the schematic representation as conveyed in Fig. 4.4. In particular, let us

address the behavior of \mathbf{G}_0 close to the band edges. First, note that $g(\varepsilon)$ is a decreasing odd function in ε , and $g_0(\varepsilon)$ is an even function in ε . Close to the band edges, both $g(\varepsilon)$ and $g_0(\varepsilon)$ will always diverge as a square root, $g \sim 1/\sqrt{\delta\varepsilon}$. Whenever the gap is located at a T -symmetric point, where $d_i(\mathbf{k}) = 0$, the strengths of the divergences in $g(\varepsilon)$ and $g_0(\varepsilon)$ are equal. To prove we first consider the regime $m < \frac{1}{2}$ where the gap is located at $\mathbf{k} = 0$. We expand $|d(\mathbf{k}_{\parallel} = 0, k_{\perp})|^2$ around that point,

$$|d(\mathbf{k}_{\parallel} = 0, k_{\perp})|^2 = m^2 + (1 - 2m)k_{\perp}^2 + \dots \quad (4.20)$$

The divergence of $g(\varepsilon)$ near the valence band edge can then be isolated by integrating over a small region $(-\alpha, \alpha)$ around the top of the valence band for small $\delta\varepsilon = \varepsilon + |m|$,

$$g(\varepsilon = -|m| + \delta\varepsilon) \approx \int_{-\alpha}^{\alpha} \frac{dk_{\perp}}{2\pi} \frac{|m|}{2|m|\delta\varepsilon + (1 - 2m)\mathbf{k}_{\perp}^2} \quad (4.21)$$

$$\approx \sqrt{\frac{|m|}{8(1 - 2m)\delta\varepsilon}} + \mathcal{O}(\delta\varepsilon^0). \quad (4.22)$$

A similar argument applies to $g_0(\varepsilon)$ close to the valence band, as the magnitude of the gap $|d_0(\mathbf{k}_{\parallel} = 0, k_{\perp} = 0)| = |m|$. Therefore $g_0(\varepsilon)$ and $g(\varepsilon)$ have exactly the same divergent behavior close to the band edge. Hence, $g + |g_0|$ only diverges close to the valence band and $g - |g_0|$ diverges close to the conduction band. Note that this analysis is valid for $m < \frac{1}{2}$, when the band gap is at $\mathbf{k} = (0, 0)$, and for $m > \frac{15}{2}$, when the band gap is at $\mathbf{k} = (\pi, \pi)$. This implies that this cancellation of divergences is present in the trivial phase (in accordance with the notion that in this phase the eigenvalues do not change sign), but also for some region in the topological phase. In the latter case, the eigenvalue beaches of \mathbf{G}_0 thus also diverge at either the valence or conduction band but do cross zero, in contrast to the trivial regime.

When $m > 1/2$ and $m < 15/2$, the gap is not located at a T -symmetric point but rather at $(0, k_G)$ or (π, k_G) . In this case, the gap satisfies $\Delta^2 = d_0(k_G)^2 + \sin^2 k_G > d_0(k_G)^2$. This last point is important, because then at any TRI point of \mathbf{k}_{\parallel} , the eigenvalues of $\mathbf{G}_0(\varepsilon, \mathbf{k}_{\parallel}^S)$ will both diverge to positive infinity at the valence band edge. To see this, we expand

$$|d(\mathbf{k})|^2 = \Delta^2 + a(k_{\perp} - k_G)^2 + \dots \quad (4.23)$$

so that the divergent parts close to the valence band edge of the Greens function terms

are

$$g(\varepsilon = -|\Delta| + \delta\varepsilon) \sim \frac{|\Delta|}{\sqrt{8a|\Delta|\delta\varepsilon}} \quad (4.24)$$

$$g_0(\varepsilon = -|\Delta| + \delta\varepsilon) \sim \frac{-d_0(0, k_G)}{\sqrt{8a|\Delta|\delta\varepsilon}}. \quad (4.25)$$

Because $|\Delta| > |d_0|$, we find that the divergences do not cancel and both eigenvalues of $\mathbf{G}_0(\varepsilon, \mathbf{k}_\parallel)$ will diverge to positive infinity at the valence band edge. This means that at the conduction band edge, both diverge to negative infinity, therefore implying an energy at which $\mathbf{G}_0(\varepsilon)$ has zero eigenvalues.

4.C.2 Details codimension-2 case

In the case of a codimension-2 surface, there are two perpendicular directions $\mathbf{k}_\perp = (k_\perp^x, k_\perp^y)$, and a similar decomposition as in the main text is given in terms of

$$\mathcal{G}_\mu(\varepsilon, k_\parallel) = \int \frac{dk_\perp^x dk_\perp^y}{(2\pi)^2} \frac{d_\mu(k_\parallel, \mathbf{k}_\perp)}{\varepsilon^2 - |d(k_\parallel, \mathbf{k}_\perp)|^2}, \quad (4.26)$$

$$\mathcal{G}(\varepsilon, k_\parallel) = \int \frac{dk_\perp^x dk_\perp^y}{(2\pi)^2} \frac{\varepsilon}{\varepsilon^2 - |d(k_\parallel, \mathbf{k}_\perp)|^2}, \quad (4.27)$$

for $\mu = 0, 1, 2, 3$. It is clear that for any of the perpendicular directions \mathcal{G}_\perp still equates to zero, as the integrand is odd. Also, for the trivial phase, it is straightforwardly seen that the eigenvalues of $\mathbf{G}_0(\varepsilon, k_\parallel, \mathbf{r}_\perp = 0)$ are again nonzero throughout the gap. This is because the two-dimensional integral can be evaluated by first integrating in one direction, which yields the results from the codimension-1 impurities, and then integrating along the second direction.

Of more interest is the question of existence of zero energy eigenvalues in the topological regime. Focusing on the two spatial dimensions, so that there are no parallel directions and we are directly probing the *local on-site Greens function*, we expect that the terms $\mathcal{G}(\varepsilon)$ and $\mathcal{G}_0(\varepsilon)$ will diverge close to the band-edge. In fact, these divergences are captured by expanding around the point where the gap is minimal, \mathbf{k}_G ,

$$|d(k^x, k^y)|^2 = \Delta^2 + a(k^x - k_G^x)^2 + b(k^y - k_G^y)^2 + \dots \quad (4.28)$$

The diverging part of the integral is then captured by the integral

$$\int -\frac{dk^x dk^y}{(2\pi)^2} \frac{1}{2\Delta\delta\epsilon + a(k^x)^2 + b(k^y)^2} \quad (4.29)$$

$$\sim -\int_0^{0+} \frac{dq}{2\pi\sqrt{ab}} \frac{q}{2\Delta\delta\epsilon + q^2} \sim \frac{\log \delta\epsilon}{4\pi\sqrt{ab}}. \quad (4.30)$$

Hence, $\mathcal{G}(\epsilon) \sim \frac{-|\Delta|\log \delta\epsilon}{4\pi\sqrt{ab}}$ and $\mathcal{G}_0(\epsilon) \sim \frac{d_0(\mathbf{k}_G)\log \delta\epsilon}{4\pi\sqrt{ab}}$ in proximity of the valence band. If the gap is not at a T -symmetric point, this automatically implies that the divergences do not cancel and we are left with eigenvalues that all diverge at both band edges, leading to the fact that the Greens functions eigenvalues have to be zero somewhere in the gap.

On the other hand, if the gap is at a symmetric point we need an extra argument to arrive at the result of the right panel of Fig. 4.4, hence consider $0 < m < \frac{1}{2}$. It is straightforwardly seen that $\mathcal{G}(\epsilon) > 0$ for $\epsilon < 0$ and $\mathcal{G}(\epsilon = 0) = 0$. At the same time, we know that both $\mathcal{G}_0(\epsilon)$ and $\mathcal{G}(\epsilon)$ have a logarithmic divergence at the valence band. However, as $d_0(k=0) > 0$, the function $\mathcal{G}_0(\epsilon)$ now goes to negative infinity. At the same time, $\mathcal{G}(\epsilon)$ goes to positive infinity because in that case the numerator is $\epsilon < 0$. Thus the two lines must cross if $\mathcal{G}_0(\epsilon = 0) > 0$, showing that there is consequently a point where \mathbf{G}_0 has zero eigenvalues.

Finally, it remains to prove that, in this construction, $\mathcal{G}_0(\epsilon = 0) > 0$ for $0 < m < \frac{1}{2}$. This actually straightforward. Since $\mathcal{G}_0(\epsilon = 0) = \int \frac{dk_{\parallel}}{2\pi} g_0(\epsilon = 0, k_{\parallel})$ we directly infer that

$$g_0(\epsilon = 0, k_{\parallel}) = (m - 4 + 2\cos k_{\parallel}) \int \frac{dk_{\perp}}{2\pi} \frac{-1}{|d(k_{\parallel}, k_{\perp})|^2} > 0 \quad (4.31)$$

for all k_{\parallel} given $m < 2$, and hence $\mathcal{G}_0(\epsilon = 0) > 0$ in the desired region $0 < m < \frac{1}{2}$.

Chapter 5

The **K-b-t** rule

The existence of physical responses distinguishing different associated orders is of central importance for the description and verification of any form of matter. The intricate relation between the appearance of mid gap dislocation modes and the space group classification of topological band insulators (TBIs), as established in the previous Chapters, directly reveals the unique status of the dislocation as the universal observable of translationally-active topological phases in this regard. In three spatial dimensions (3D), however, these results in fact impose a paradoxical conundrum from a geometrical point of view, as the characterization of the topological entity of the bulk heuristically corresponds to its specific monopole configuration in the Brillouin zone whereas dislocations in this scenario entail line-like defects. In addition, the possibility of aligning the dislocation line direction vector along the Burgers vector similarly signals a more profound interplay of the lattice topology and the electronic-band structure.

On the other hand, due to the generality of the above mechanisms, it is evident that a dislocation with a Burgers vector along the direction of a non- Γ band inversion in reciprocal space should still result in the formation of mid gap modes. Accordingly, it was demonstrated that dislocation lines in three-dimensional TBIs indeed support propagating helical modes that can probe the weak invariants [138, 39]. Nonetheless, as the weak invariants have been proven to be inadequate in the light of the general characterization of \mathbb{Z}_2 topological insulating states when the underlying crystal symmetries are taken into account, this raises the question whether the additional anticipated effects regarding the response to dislocations can emerge when the description of the accommodating TBI is appropriately generalized.

In this Chapter, we elucidate the general rule governing the response of dislocation lines in three-dimensional TBIs and uncover their role in the space group classification scheme. According to this **K-b-t** rule, the lattice topology, represented by dislocation lines oriented in the direction \mathbf{t} having Burgers vector \mathbf{b} , conspires with the electronic-band topology, characterized by the band-inversion momentum \mathbf{K}_{inv} , to produce an explicit criterium for the formation of gapless propagating modes along these line defects. Due to the indicated correspondence between the dislocation modes and the classification procedure this in turn reconfirms the introduced framework. Most interestingly, the general principles also identify that, for sufficiently symmetric crystals, this conspiracy leads to topologically-protected metallic states bound to freely deformable dislocation channels, that can be arbitrarily embedded in the parent TBI. These findings are moreover experimentally consequential as dislocation defects are ubiquitous in any real crystal.

5.1 Formulation and general principles

Although early on it was identified that in three-dimensional TBIs dislocation lines support propagating helical modes [138, 139, 140, 141], the precise role of dislocations has not been explored thoroughly. In particular, the relation between the lattice symmetry and the electronic topology, as well as the characterization of these topological states through the response of the dislocation lines has not been addressed. We here fill this void by detailing the specific mechanism in the light of the space group classification.

Dislocations in three dimensions (3D) are defects with a far richer structure than their two-dimensional counterparts. They form lines $\mathbf{l}(\tau)$ characterized by a tangent vector $\mathbf{t} \equiv d\mathbf{l}/d\tau$, with the discontinuity introduced to the crystalline order described by the Burgers vector \mathbf{b} . Both these vectors can only be oriented along the principal axes of the crystal, and screw (edge) dislocations are obtained when $\mathbf{b} \parallel \mathbf{t}$ ($\mathbf{b} \perp \mathbf{t}$), see Fig. 5.1. Moreover, the Burgers vectors are additive, and in full generality we can thus consider only dislocations with the Burgers vectors equal to Bravais lattice vectors. The crucial fact that then reconnects these notions to the classification scheme is the observation that translational lattice symmetry is preserved along the defect line for any proper dislocation probing the specific crystal geometry. Therefore, the full lattice Hamiltonian in the presence of a dislocation oriented along, for instance, the z -axis

$(\mathbf{t} = \mathbf{e}_z)$ can be written as

$$H_{3D}(x, y, z) = \sum_{k_z} e^{ik_z z} H_{\text{eff}}^{2D}(x, y, k_z). \quad (5.1)$$

Notice that the 2D lattice Hamiltonian H_{eff}^{2D} possesses the (wallpaper group) symmetry of the crystallographic plane orthogonal to the dislocation line, because the Burgers vector is a Bravais lattice vector. This directly confirms the universal status of the dislocation as the translational probe of the lattice topology and shows the compatibility of the above in the context of the full underlying space group.

Given the fundamental reduction procedure, we revert to the electronic topology of a TBI, which is characterized by the band-inversions at the time-reversal invariant (TRI) momenta \mathbf{K}_{inv} in the Brillouin zone (BZ). As a dislocation disturbs the crystalline order only microscopically close to its core, we can use the continuum theory of elasticity to describe its effect at low energies. The elastic deformation of the continuous medium is encoded by a distortion field $\boldsymbol{\epsilon}_i$ of the global Cartesian reference frame \mathbf{e}_i , $e_i^\alpha = \delta_i^\alpha$, with $i, \alpha = 1, 2, 3$ [116, 115]. The momentum of the electronic excitations near the transition from a topologically trivial to a non-trivial phase with the bandgap closing at the momentum \mathbf{K}_{inv} is accordingly given by $k_i = (\mathbf{e}_i + \boldsymbol{\epsilon}_i) \cdot (\mathbf{K}_{\text{inv}} - \mathbf{q})$, with $q \ll K_{\text{inv}} \sim 1/a$, $\epsilon \sim a/r$, a the lattice constant, and r being the distance from the defect core. Therefore the dislocation gives rise to a $U(1)$ gauge field $A_i = -\boldsymbol{\epsilon}_i \cdot \mathbf{K}_{\text{inv}}$ that minimally couples to the electronic excitations, $\mathbf{q} \rightarrow \mathbf{q} + \mathbf{A}$. Moreover, the translational symmetry then implies that the resulting gauge field only has non-trivial components in the plane orthogonal to the dislocation line, consistent with Eq. (5.1), carrying an effective flux $\Phi = \mathbf{K}_{\text{inv}} \cdot \mathbf{b}$, as we demonstrate below.

Consider for concreteness an edge and a screw dislocation both oriented along the z -axis. We use that for the edge dislocation with Burgers vector $\mathbf{b} = a\mathbf{e}_x$, the dual basis in the tangent space at the point \mathbf{r} is $\mathbf{E}^x = \left(1 - \frac{ay}{2\pi r^2}\right)\mathbf{e}^x + \frac{ax}{2\pi r^2}\mathbf{e}^y$, $\mathbf{E}^y = \mathbf{e}^y$, $\mathbf{E}^z = \mathbf{e}^z$, while for the screw dislocation with $\mathbf{b} = a\mathbf{e}_z$, we have $\mathbf{E}^x = \mathbf{e}^x$, $\mathbf{E}^y = \mathbf{e}^y$, $\mathbf{E}^z = \frac{b}{2\pi r^2}(-y\mathbf{e}^x + x\mathbf{e}^y) + \mathbf{e}^z$; $r^2 \equiv x^2 + y^2$ [116]. The corresponding distortions for both an edge and a screw dislocation are then readily verified to be $\boldsymbol{\epsilon}_x = \frac{y}{2\pi r^2}\mathbf{b}$, $\boldsymbol{\epsilon}_y = -\frac{x}{2\pi r^2}\mathbf{b}$ to leading order in a/r (see Appendix 5.B). Consequently, the corresponding gauge potential $\mathbf{A}(\mathbf{r})$ has non-trivial components in the plane orthogonal to the dislocation line, $\mathbf{A} \cdot \mathbf{t} = 0$, and

$$\mathbf{A} = \frac{-y\mathbf{e}_x + x\mathbf{e}_y}{2\pi r^2}(\mathbf{K}_{\text{inv}} \cdot \mathbf{b}) \equiv \frac{-y\mathbf{e}_x + x\mathbf{e}_y}{2\pi r^2}\Phi. \quad (5.2)$$

When this flux $\Phi \pmod{2\pi}$ is nonzero, the dislocations host propagating helical modes provided that the 2D Hamiltonian in a TRI plane orthogonal to the dislocation line, $\hat{\mathbf{t}} \equiv \mathbf{t}/|\mathbf{t}|$, is topologically non-trivial in the exact sense of the space group classification. That is, only when the projected Hamiltonian $H_{\text{eff}}^{2D}(k)$ features an odd number of *non-symmetry* related translationally-active inversion momenta, mid gap states at that momentum k are developed for non-zero Φ . The full spectrum of modes, for each k , is then protected by the lattice symmetry that relates the gauged momenta \mathbf{K}_{inv} . This is what we refer to as the $\mathbf{K}\text{-}\mathbf{b}\text{-}\mathbf{t}$ rule (see Fig. 5.1).

Finally, we note that this rule and the following descendant construction together imply that the bound states for a given $\mathbf{k} \cdot \hat{\mathbf{t}}$ momentum combine into a spectrum of propagating helical modes along the dislocation line. For $\mathbf{k} \cdot \hat{\mathbf{t}} = \mathbf{K}_{\text{inv}} \cdot \hat{\mathbf{t}}$, the system develops a Kramers pair of true zero modes $\Psi_0 \equiv (\psi_0, T\psi_0)^\top$, with T representing the time-reversal operator satisfying $T^2 = -1$. We should stress here that for this specific momentum the reduced system precisely reduces to a representative of the 2D problems considered in the previous Chapters and that the term zero mode should be interpreted in this manner. This is a consequence of the fact that by definition the \mathbf{K}_{inv} point is a TRI point hosting a band inversion. Deviating from this 'parent' momentum by $\mathbf{q} \cdot \hat{\mathbf{t}}$, the effective low-energy Hamiltonian for the propagating modes then generally develops a linear gap $H_{\text{eff}} \sim \mathbf{q} \cdot \hat{\mathbf{t}}$, to lowest order. The gapped Kramers pair of descendant states are then present as long as $H_{\text{eff}}(q)$ remains in the topological non-trivial phase and may then be captured by $H_{\text{eff}} = v_t \Sigma_3 (\mathbf{q} \cdot \hat{\mathbf{t}}) + \mathcal{O}(q^2)$. Where, the Pauli matrix Σ_3 acts in the two-dimensional Hilbert space of the dislocation modes, which are of the form $\Psi_{q_t} \equiv (\psi_0 e^{i(\mathbf{q} \cdot \hat{\mathbf{t}})(\mathbf{r} \cdot \hat{\mathbf{t}})}, (T\psi_0) e^{-i(\mathbf{q} \cdot \hat{\mathbf{t}})(\mathbf{r} \cdot \hat{\mathbf{t}})})^\top$, and v_t is the characteristic velocity, which is set by the symmetries and details of the band structure.

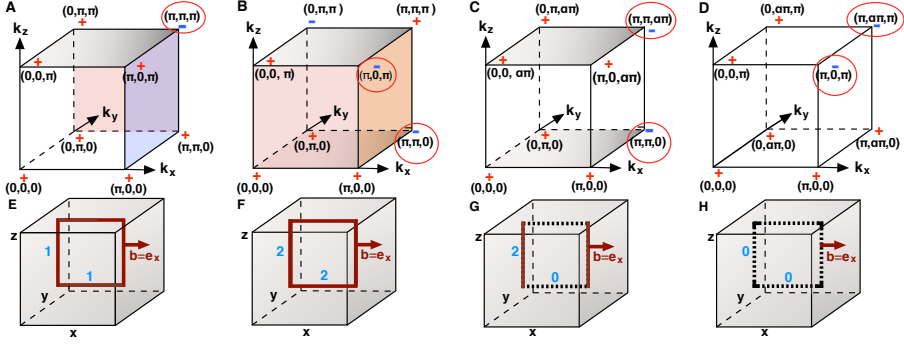


Figure 5.1: *Illustration of the \mathbf{K} - \mathbf{b} - \mathbf{t} rule relating the electronic topology in the momentum space (top panels), and the effect of dislocations in real space (bottom panels). Panels A to D show the electronic-band topology of the T - $p3(4)_R$ and T - $p3(4)_M$ phases on a simple cubic lattice and the $p4_{R,M}$ and $p4_{X',R}$ weak phases on tetragonal lattices. A dislocation with Burgers vector $\mathbf{b} = \mathbf{e}_x$ acts on the encircled TRI momenta in the planes orthogonal to the dislocation line. As a result, the colored planes host an effective π flux. The resulting number of Kramers pairs of helical modes along the edge and screw parts of the loop is indicated with the blue number. (A) The symmetric T - $p3(4)_R$ phase has a topologically non-trivial plane hosting a π flux orthogonal to any of the three crystallographic directions and hence any dislocation loop binds modes along the entire core, as shown for a loop in the $\hat{x}-\hat{z}$ plane, panel E. (B) In the T - $p3(4)_M$ phase, translationally active phases in the TRI planes orthogonal to k_z and a valley phase in $k_x = \pi$ plane host π fluxes. Hence the dislocation loop binds two pairs of modes, as displayed in panel F. These modes are symmetry-protected against mixing. (C) In the $p4_{M,R}$ phase, only the TRI planes normal to k_z host an effective π -flux and hence the same dislocation loop binds modes only to the edge-dislocation parts, as displayed in panel G. These modes are not protected against mixing. (D) The $p4_{X',R}$ phase all TRI planes orthogonal to the dislocations lines have a trivial flux, and, according to the \mathbf{K} - \mathbf{b} - \mathbf{t} rule, neither the edge nor the screw dislocation of the loop binds modes, as illustrated in panel H.*

5.2 Implications of the rule

The above formulated **K-b-t** rule demonstrates how the dislocation line **t**, the Burgers vector **b** and the TRI momenta \mathbf{K}_{inv} conspire into a precise condition determining the existence of the dislocation propagating modes in certain directions in a topologically-insulating phase, consistent with the space group classification (see Fig. 5.1). By varying **t** and **b** in all directions, the number of "parent" zero modes in any projection plane is in one-to-one correspondence with the space group classification in terms of the \mathbf{K}_{inv} momenta. Specifically, for a translational active phase with a single \mathbf{K}_{inv} momentum, edge and screw dislocations bind a single Kramers pair of helical modes if $\mathbf{K}_{\text{inv}} \cdot \mathbf{b} \neq 0$. In case of a translationally active phase or a valley phase with multiple \mathbf{K}_{inv} momenta, a projected 2D system may also result in a double pair of modes if the effective system entails a 2D valley phase. The two pairs are then protected by the symmetries relating the \mathbf{K}_{inv} momenta. Most interestingly, there is the possibility that both edge and screw dislocations bind modes in any crystal direction resulting in propagating modes along the full dislocation loops. In particular, in a completely isotropic lattice with O_h crystal symmetry a strong variant of this effect can be realized: the gapless states in the dislocation loop that propagate in a way completely oblivious to the lattice directions.

In contrast, in a weak phase characterized by the weak topological invariant **M**, protected helical modes are argued to exist only when the product $\mathbf{M} \cdot \mathbf{b} \pmod{2\pi}$ is non-trivial [138, 139, 140, 39]. This is consistent with the fact that double pairs of modes originating from two \mathbf{K}_{inv} not related by symmetry may be gapped out. However, according to the **K-b-t** rule if the \mathbf{K}_{inv} are related by symmetry such pairs in fact enjoy protection. Moreover, the **K-b-t** rule precisely reveals the condition for the formation of the mid gap modes in the case of a generic crystal group, whereas the definition of a weak invariant necessitates a layered structure. We thus observe that the appropriate generalization of the weak invariants to the general space group classification directly exposes the anticipated more elaborate dislocation response mechanism.

5.3 Exemplification

The above general statements can be illustrated by employing the familiar class of simple tight-binding models comprising two orbitals (Appendix 5.A) with different parity and two spin states [45, 142] on a simple cubic lattice with space group $pm\bar{3}m$

$$H_{nn} = A(\gamma_1 \sin k_x + \gamma_2 \sin k_y + \gamma_3 \sin k_z) + M_{nn} \gamma_0. \quad (5.3)$$

Here \mathbf{k} refers the electron momentum, the γ -matrices act in the orbital and the spin spaces, and we have used natural units ($\hbar = c = a = 1$). As usual, the topological phases of the model (5.3) can be tuned with the mass term $M_{nn} = m - 2B(3 - \cos k_x - \cos k_y - \cos k_z)$. Let us assume that the system is in the $T-p3(4)_R$ phase with the band-inversion at momentum (π, π, π) (Figures 5.1(A) and 5.2). If $\mathbf{b} = \mathbf{e}_x$ and $\mathbf{t} = \mathbf{e}_z$, the effective Hamiltonian in the $k_z = \pi$ plane reduces to the π flux problem in the two-dimensional $T - p4_M$ phase, and hence possesses zero modes. For the family of Hamiltonians (5.1) any momentum $k_z = \pi + q_z$ infinitesimally close to $k_z = \pi$ then yields the would-be zero modes in the absence of the term $\sim \gamma_3$. When included, this term gives rise to the anticipated linearly dispersing propagating modes along the dislocation line. Moreover, the **K-b-t** rule also directly conveys the number of descendent states in the spectrum, as the mass term $M_{nn}(k_z)$ sets the topological condition for the existence of the dislocation mode (see Appendix 5.B). Furthermore, the same rule implies that an edge or a screw dislocation along any Bravais lattice vector in the simple cubic lattice effectively acts as a π flux. Henceforth, when these defects are joined in a loop in the $x - z$ -plane with $\mathbf{b} = \mathbf{e}_x$, we expect propagating modes, which are indeed found in the corroborating numerical computations as detailed in the Appendix and Fig. 5.2. We note that TRS together with the crystal symmetry evidently protects the modes from backscattering in this scenario.

As a next step, we consider the system in the $T - p3(4)_M$ phase with the band-inversion located at the momenta $M \equiv (\pi, \pi, 0)$, $X' \equiv (\pi, 0, \pi)$, $Y' \equiv (0, \pi, \pi)$, which are related by the threefold rotational symmetry (Figs. 5.1(B), (5.7) and (5.12)). According to the **K-b-t** rule, for the edge-segment of the dislocation loop, both the $k_z = 0$ and $k_z = \pi$ planes host an effective π -flux, originating from the M and X' points. Additionally, the $k_x = \pi$ plane hosts a valley phase, and thus the screw-dislocation parts also host two pairs of modes. Therefore, there is a total of two Kramers pairs of gapless dislocation modes along the loop, which are *protected by symmetry*. Note that their existence crucially

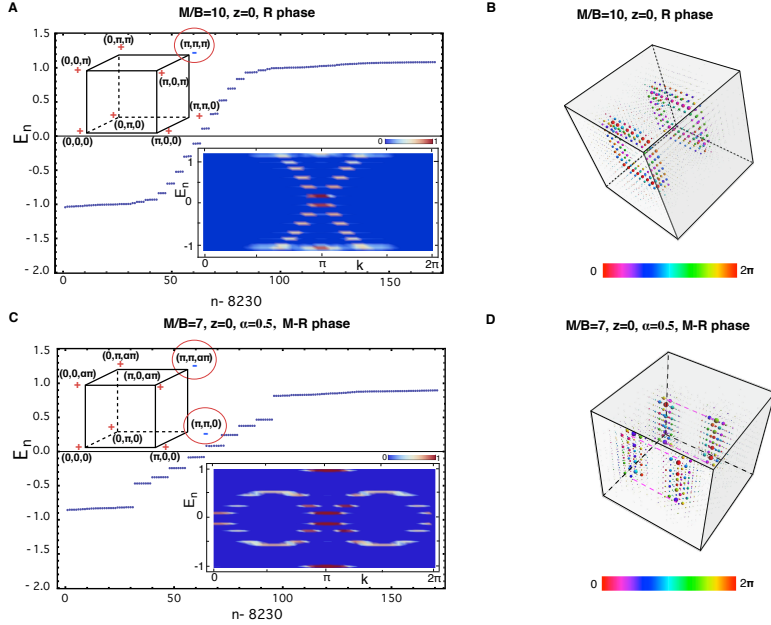


Figure 5.2: The effect of dislocation lines in 3D topological band insulators. Edge and screw dislocations with Burgers vector $\mathbf{b} = \mathbf{e}_x$ are treated simultaneously by considering dislocation loops of 8×8 sites within the tight-binding model (5.3) on the lattice with $16 \times 16 \times 16$ sites in case of periodic boundary conditions, see the Appendix for details. Panels A and C show the spectrum of the dislocation modes traversing the gap in case of the $T\text{-}p3(4)_R$ and $p4_{M,R}$ phases, with the corresponding electronic topological configurations shown in the insets on the upper left. The circles indicate the TRI momenta hosting band-inversions that yield effective π -fluxes. Additionally, the spectral density as function of the momentum \mathbf{k} , defined along the dislocation line, is displayed in the insets on the lower right. We find a single cone for the $T\text{-}p3(4)_R$ phase, and a double cone for the $p4_{M,R}$ phase, consistent with the **K-b-t** rule. The energy levels are now eight-fold degenerate as both $k_z = 0$ and $k_z = \pi$ planes are topologically non-trivial, and thus each yields propagating modes due to the effective π flux introduced by the dislocations. Panels B and D display the real space localization of the modes, where the weight of the wavefunction is indicated by the size of the circles and the color coding indicates the corresponding phase. Most importantly, the $T\text{-}p3(4)_R$ features topologically-protected propagating dislocation modes along the complete loop. In contrast, the $p4_{M,R}$ phase binds modes only along the edge-dislocation parts. In particular, we find eight energy levels in correspondence with the number of allowed momenta along the dislocation.

depends on the fact that the M and X' momenta are symmetry-related. Were this not the case, the weak index of this $T - p3(4)_M$ phase $M_i = (0, 0, 0)$ would predict no dislocation modes at all.

In contrast, let us now break the cubic symmetry by considering the $p4_{M,R}$ phase on a tetragonal lattice with $a_x = a_y = a$, $a_z = a/\alpha$, where a_i is the lattice constant in the direction \mathbf{e}_i , and $\alpha \neq 1$ is the lattice deformation parameter (Figs. 5.1(C) and 5.2). We stipulate here the subtle difference between such a weak phase and a valley phase, which has an even number of band-inversions *protected* by a 3D space group symmetry. The usual strong and weak indices [39, 37, 138] in this phase are $(\mathbf{v}; M_i) = (0; 0, 0, 1)$, and thus $\mathbf{M} \cdot \mathbf{b} = 0$. Nonetheless, the $k_z = 0$ and $k_z = \alpha\pi$ planes are topologically non-trivial therein (Fig. 5.1 and Appendix). As a result, for a dislocation loop with $\mathbf{b} = \mathbf{e}_x$, according to the $\mathbf{K}\text{-}\mathbf{b}\text{-}\mathbf{t}$ rule, we find modes bound only to the the edge-dislocation parts. As both these planes contribute the midgap states, we expect a double Kramers pair of the propagating metallic states, which our numerical computations indeed confirm. However, these modes can mix in the dislocation loop, since no symmetry relates the momenta M and R giving rise to them. Nevertheless, in terms of principle we thus observe that the richer $\mathbf{K}\text{-}\mathbf{b}\text{-}\mathbf{t}$ rule consistently unveils the formation mechanism of the dislocation modes, whereas the the underlying symmetry directly conveys the stability.

Finally, we consider the tetragonal $p4_{X',R}$ ($p4_{Y',R}$) phase obtained by deforming the cubic lattice in the \mathbf{e}_y (\mathbf{e}_x) direction with the corresponding band-inversions at $(\pi, 0, \pi)$ $[(0, \pi, \pi)]$ and $(\pi, \alpha\pi, \pi)$ $[(\alpha\pi, \pi, \pi)]$ momenta (Fig. 5.1(D)). In this case, we find that no dislocation modes appear in the $p4_{X',R}$ phase, whereas in the $p4_{Y',R}$ phase only the band-inversion at momentum $(\alpha\pi, \pi, \pi)$ contributes a π flux, thus yielding the modes for both types of dislocations. These results are therefore similar as in the $T\text{-}p3(4)_R$ phase, as also confirmed by numerical computations showing modes propagating along the entire loop in the $x - z$ plane. Notice, nonetheless, that due to the unequivalence in directions the velocities along the loop are now in general anisotropic.

5.4 Experimental consequences

The response to dislocations in TBIs is evidently consequential from an experimental point of view, as these defects are ubiquitous in any crystals. In particular, the electron-doped mixed-valent perovskite oxide BaBiO_3 with a simple cubic crystal symmetry has

been recently predicted to be a \mathbb{Z}_2 topological band insulator [143]. Most interestingly, the associated topological phase is believed to entail the symmetric $T\text{-}p3(4)_R$ phase, which should host propagating gapless modes along any dislocation loop, as demonstrated above. The effective tight-binding model (5.3) therefore describes this phase in terms of the explicit parameters $A = 2.5\text{eV}\cdot\text{\AA}$, $B = 9.0\text{eV}\cdot\text{\AA}^2$, $M = 5.08\text{eV}$, and the lattice constant $a = 4.35\text{\AA}$ [143], implying that the velocity of the dislocation modes is $v = A/\hbar = 4.3 \times 10^5\text{m/s}$, while the localization length $\lambda \sim \sqrt{B/(12Ba^{-2} - M)} \simeq 4.8\text{\AA}$. More generally, the enhanced density of states near the dislocation line in any non- Γ TBI [42, 144, 126, 127] should be observable by local probes, such as scanning tunneling microscopy. Angle-resolved photoemission spectroscopy may finally also be useful for mapping out these states, since the surface irregularities should not affect this probe.

5.5 Conclusions

In conclusion, we have addressed the specific criteria underlying the formation of propagating modes bound to dislocation defects in 3D \mathbb{Z}_2 topological band insulators, culminating in the formulation of the **K-b-t**-rule. As a general result, this rule directly signifies the consistency of the introduced space group classification framework from a physical response perspective and, in fact, exposes an intricate relation between the lattice topology and the electronic band topology. Specifically, dislocations are naturally associated with a fundamental reduction procedure, that is compatible with the relevant lattice symmetries and allows for a direct determination of the existence of dislocation modes for each subsystem of descendant momentum k in any specific topological phase. These results, in addition, bear experimental relevance, as dislocations represent ever-present defects in any crystal and serve as the universal probes of translational topological order. In particular, a strong representing and striking variant of the detailed mechanism occurs in the $T\text{-}p3(4)_R$ phase of materials that feature an isotropic O_h symmetric crystal structure, as in this case the modes propagate along arbitrarily oriented loops in a manner that is completely oblivious to the lattice directions.

5.A Model details

Although we have employed the $M - B$ class of models (Eqs. (2.7) and (2.8)) already extensively for verification purposes, we here present the details regarding the associated topological states realized on cubic and tetragonal lattices. We depart from the generic form comprising two spin degenerate orbitals as described by

$$H = \varepsilon(\mathbf{k})\mathbf{1} + \sum_{\alpha} d_{\alpha}(\mathbf{k})\gamma_{\alpha} + \sum_{\alpha\beta} d_{\alpha\beta}\gamma_{\alpha\beta} \quad (5.4)$$

where γ_{α} are the five Dirac matrices obeying the Clifford algebra $\{\gamma_{\alpha}, \gamma_{\beta}\} = 2\delta_{\alpha\beta}$ and $\gamma_{\alpha\beta}$ are the ten commutators $\gamma_{\alpha\beta} = \frac{1}{2i}[\gamma_{\alpha}, \gamma_{\beta}]$. Specifically, we take the following basis of γ -matrices

$$\gamma_0 = \sigma_0 \otimes \tau_3 \quad \gamma_1 = \sigma_1 \otimes \tau_1, \quad \gamma_2 = \sigma_2 \otimes \tau_1, \quad \gamma_3 = \sigma_3 \otimes \tau_1, \quad \gamma_5 \equiv -\gamma_0\gamma_1\gamma_2\gamma_3 = \sigma_0 \otimes \tau_2,$$

with σ and τ being the standard Pauli matrices acting in the spin and orbital space, respectively; $\mathbf{1} = \sigma_0 \otimes \tau_0$ with σ_0, τ_0 as the 2×2 unity matrices.

The explicit form of the Hamiltonian (5.4) is then determined by exploiting the symmetries. For simplicity we assume, in addition to time-reversal symmetry, a well-defined parity for the tight-binding model, as our interest lies in the topological aspects of the resulting phases. Concretely, time-reversal symmetry is represented by the operator $T = \vartheta K$, with $\vartheta = i\sigma_2 \otimes \tau_0$ and K as complex conjugation, whereas the parity operator is $P = \gamma_0$. As the commutators $\gamma_{\alpha\beta}$ transform under time-reversal and parity with the opposite sign, the assumption of having both these symmetries thus simply results in $d_{\alpha\beta} = 0$. The remaining functions $d_{\alpha}(\mathbf{k})$ of the effective model can then be obtained from the theory of invariants. Let us consider the space group $pm\bar{3}m$ with the point group O_h in particular. This point group has two one-dimensional, one two-dimensional and two three-dimensional irreducible representations. The matrix γ_0 anticommutes with the γ -matrices $\{\gamma_1, \gamma_2, \gamma_3\}$ and therefore represents the mass term, which is by construction even under the parity. The corresponding mass term has to be rotationally-symmetric and therefore entails an even polynomial in the momentum, \mathbf{k} . Using also that the γ -matrices $\{\gamma_1, \gamma_2, \gamma_3\}$ form a three-dimensional representation under rotations in O_h , we arrive at the following minimal continuum Hamiltonian that captures the topologically non-trivial phases of interest

$$H_{eff} = A(k_x\gamma_1 + k_y\gamma_2 + k_z\gamma_3) + M_m\gamma_0 + \mathcal{O}(k^3), \quad (5.5)$$

where $M_{nn} = m - 2B(k_x^2 + k_y^2 + k_z^2)$ and we have dropped the term $\sim \mathbf{1}$ not relevant for the topological analysis here. This Hamiltonian evidently generalizes the 2D model (3.1) to three dimensions (3D) and its different incarnations have already been used to describe topological states in Bismuth-based compounds [45, 142].

We can then readily determine the lattice-regularized version of the effective model (5.5) to arrive at the usual class of models. Considering a simple cubic lattice with nearest-neighbor (nn) hoppings, we obtain the following tight-binding Hamiltonian

$$H_{nn} = A(\gamma_1 \sin k_x + \gamma_2 \sin k_y + \gamma_3 \sin k_z) + M_{nn} \gamma_0, \quad (5.6)$$

with the effective mass parameter

$$M_{nn} = m - 2B(3 - \cos k_x - \cos k_y - \cos k_z).$$

In the above we have set the lattice constant a to unity and we note that the parameters A (B) represent the familiar hopping amplitudes between different (same) orbitals, while m is the difference of the onsite energies between the two orbitals. Furthermore, the hoppings in the Hamiltonian (5.6) are equal in the three orthogonal directions due to the rotational symmetry.

The above Hamiltonian reduces to the continuum Hamiltonian (5.5) when expanded around the Γ or the R -point located at the momentum (π, π, π) in the Brillouin zone (BZ). However, in order to enrich the phase diagram, we concede the possibility of adding next-nearest-neighbor hopping terms of the same fashion as the nearest-neighbor ones to the Hamiltonian. Taking into account that on a cube each site has four next-nearest in each of the three mutually orthogonal crystallographic planes, these additional terms assume the form

$$\begin{aligned} H_{nnn} = & \frac{\tilde{A}}{2} [\sin(k_x + k_y)(\gamma_1 + \gamma_2) + \sin(-k_x + k_y)(-\gamma_1 + \gamma_2)] \\ & + \frac{\tilde{A}}{2} [\sin(k_x + k_z)(\gamma_1 + \gamma_3) + \sin(-k_x + k_z)(-\gamma_1 + \gamma_3)] \\ & + \frac{\tilde{A}}{2} [\sin(k_y + k_z)(\gamma_2 + \gamma_3) + \sin(-k_y + k_z)(-\gamma_2 + \gamma_3)] \\ & - 4\tilde{B}[3 - \cos(k_x) \cos(k_y) - \cos(k_x) \cos(k_z) - \cos(k_y) \cos(k_z)] \gamma_0. \end{aligned} \quad (5.7)$$

Hence, considering both contributions the total Hamiltonian is given by

$$H_{TB} = H_{nn} + H_{nnn} \quad (5.8)$$

The different topological phases are then obtained by varying the mass term multiplying the γ_0 matrix. The topological phase transitions occur when the mass term vanishes at the time-reversal invariant momenta in the BZ and the corresponding phases can be characterized by the mass term at these special momenta, as outlined in the previous Chapter. As a result, the phase diagram, with $A = 1$, is readily obtained as a function of M/B and \tilde{B}/B , see Fig. 5.3.

Finally, note that by lowering the full rotational symmetry of the Hamiltonian (5.6) to in plane C_4 rotations, one directly obtains a minimal tight-binding Hamiltonian describing topological phases on a tetragonal lattice

$$H_{\text{nn}}^{\text{tetragonal}} = A_x \gamma_1 \sin k_x + A_y \gamma_2 \sin k_y + A_z \gamma_3 \sin k_z + [m - 2B_x(1 - \cos k_x) - 2B_y(1 - \cos k_y) - 2B_z(1 - \cos k_z)] \gamma_0, \quad (5.9)$$

which will be of use in the remainder.

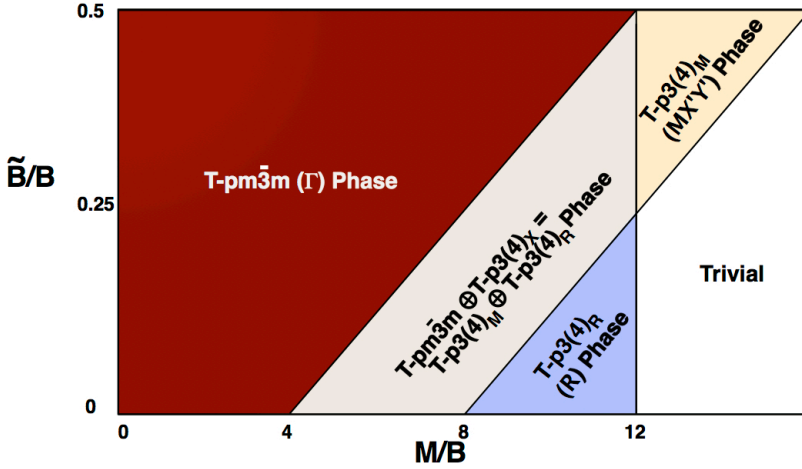


Figure 5.3: The phase diagram of the outlined model (5.8), in case of O_h symmetry or space group $pm\bar{3}m$. As function of the mass parameter M/B and the nearest neighbor coupling \tilde{B}/B , the mass parameters at the TRI momenta can be tuned to produce the different electronic topological configurations shown.

5.B Analytical and numerical evaluation of dislocation modes in three dimensional \mathbb{Z}_2 topological insulators

In this Appendix we elaborate on the details underlying the formation criteria of the dislocation modes in the context of the models of the previous section, illustrating the working of the **K-b-t** rule in a concrete setting. Let us first examine the effect of dislocations in the coarse-grained continuum theory. In this instance the lattice defects are described within the elastic continuum theory using vielbeins, encoding the map from the perfect lattice to the distorted lattice [114, 116]. The resulting torsion T^i and curvature R_j^i are then generally related to the vielbeins E_α^i and the spin connection ω_j^i by the Einstein-Cartan structure equations

$$\begin{aligned} T^i &= dE^i + \omega_j^i \wedge E^j \\ R_j^i &= d\omega_j^i + \omega_k^i \wedge \omega_j^k. \end{aligned} \quad (5.10)$$

For a dislocation defect, the curvature vanishes while the torsion is singular. Specifically, $T^i = b^i \delta(\mathbf{l})$ in terms of the Burgers vector \mathbf{b} and the position \mathbf{l} of the dislocation line. Since the curvature tensor vanishes for a dislocation, the corresponding spin-connection can therefore be set to zero, thereby resulting in an exclusive dependence of the above set of equations on the effective vielbeins.

5.B.1 Edge dislocations

Turning to the case of an edge dislocation oriented along the \hat{z} -direction, the vielbein takes the form

$$\hat{E} \equiv E_\alpha^i = \begin{pmatrix} 1 - \frac{by}{2\pi r^2} & \frac{bx}{2\pi r^2} & 0 \\ 0 & 1 & 0 \\ 0 & 0 & 1 \end{pmatrix}, \quad (A8)$$

where b is the magnitude of the Burgers vector \mathbf{b} , which is assumed to be along the \hat{x} -direction $\mathbf{b} = b\mathbf{e}_x$, and $r^2 = x^2 + y^2$. The inverse of the above vielbein is subsequently

readily computed, resulting in

$$\hat{E}^{-1} \equiv E_i^\alpha = \begin{pmatrix} \left(1 - \frac{by}{2\pi r^2}\right)^{-1} & -\frac{bx}{2\pi r^2} \left(1 - \frac{by}{2\pi r^2}\right)^{-1} & 0 \\ 0 & 1 & 0 \\ 0 & 0 & 1 \end{pmatrix}. \quad (5.11)$$

As for an elementary dislocation $b = a$, with a as the lattice constant, the distortion field $\mathbf{E}_i = \mathbf{e}_i + \boldsymbol{\epsilon}_i$ to the leading order in a/r is directly verified to be

$$\boldsymbol{\epsilon}_x = \frac{ay}{2\pi r^2} \mathbf{e}_x = \frac{y}{2\pi r^2} \mathbf{b} \quad \boldsymbol{\epsilon}_y = -\frac{ax}{2\pi r^2} \mathbf{e}_x = -\frac{x}{2\pi r^2} \mathbf{b}.$$

The corresponding gauge potential $\mathbf{A} = -\boldsymbol{\epsilon}_i \cdot \mathbf{K}_{\text{inv}}$, with \mathbf{K}_{inv} the band-inversion momentum, can then straightforwardly be obtained, reproducing Eq. (5.2) in the main text.

We can now consider the effect of an edge dislocation in a 3D topological insulator. We note that along the core of the dislocation translational symmetry is preserved. Henceforth, k_z is a good quantum number and we obtain a family of two-dimensional Hamiltonians

$$H(x, y, z) = \sum_{k_z} e^{ik_z z} H_{eff}(x, y, k_z). \quad (5.12)$$

The dimensionally-reduced Hamiltonian $H_{eff}(x, y, k_z)$ can then be treated using the methods of the previous Chapters, allowing for a direct evaluation of the spectrum of dislocation modes. Let us make this more concrete for the model with the Hamiltonian (5.8). We assume that the system is in the T - $p3(4)_R$ or R phase (Fig. 5.4). Using $\mathbf{k} \rightarrow \mathbf{k} + \mathbf{A} = \mathbf{k} + \frac{1}{2r} \mathbf{e}_\varphi$, a straightforward calculation yields

$$H_{eff}(x, y, k_z) = i\gamma_r \partial_r + i\gamma_\varphi \left(\frac{\partial_r}{r} + \frac{1}{2r} \right) + \gamma_0 \left[M - 2B \left(\Delta + \frac{i}{r^2} \partial_\varphi - \frac{1}{4r^2} \right) \right] + \sin(k_z) \gamma_3, \quad (5.13)$$

where

$$M = m - 8B - 2B(1 - \cos k_z) = \hat{M} - 2B(1 - \cos k_z). \quad (5.14)$$

Here, the Laplacian $\Delta = \partial_r^2 + \frac{\partial_r}{r} + \frac{1}{r^2} \partial_\varphi^2$, and (r, φ) refer to the usual polar coordinates, relating to the Cartesian ones as $x = r \cos \varphi$, $y = r \sin \varphi$.

To analyze the propagating dislocation-bound midgap modes, let us first neglect the last γ_3 term in the Hamiltonian $\sim \sin k_z$. In this scenario we then exactly retrieve the familiar 2D $M - B$ Hamiltonian with effective mass term M . Therefore, this Hamiltonian hosts zero modes for the values of the parameters m, B, k_z obeying $0 < M/B < 4$. Now, take $k_z = \pi$. Then, as $8 < m/B < 12$, it follows that $4 < \hat{M}/B < 8$, which is precisely

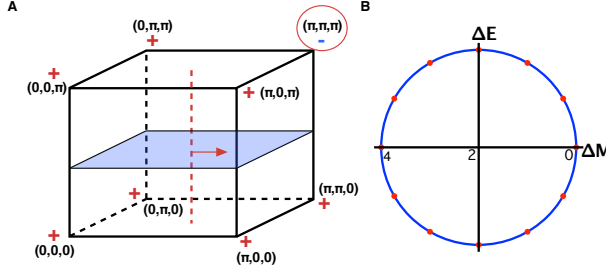


Figure 5.4: The left panel shows the schematic configuration of the $T\text{-}p3(4)_R$ or R phase in the Brillouin zone with an edge dislocation with Burgers vector $\mathbf{b} = \mathbf{e}_x$ and is oriented along the \hat{z} direction in the real space. The right panel displays the modes k_z on the unit circle in the complex plane. The imaginary part then encodes for the mass gap of the dislocation mode with respect to the zero mode, whereas the real part relates to the shift $\Delta M(k_z) = -M/B + \hat{M}/B = 2(1 - \cos(k_z))$ of the effective mass parameter in the associated dimensionally reduced $M - B$ model.

the condition for a zero mode solution bound to the dislocation. This solution entails the one derived and discussed in detail in previous Chapters. More specifically, in this parameter range the system entails the $T\text{-}p4$ or M phase in the reduced 2D Hamiltonian. Similarly, the next k_z value in a finite system results in a dislocation mode if the effective mass $\hat{M}(k_z)$ still satisfies the topological condition $4 < \hat{M}/B < 8$. Moreover, we can exactly determine the corresponding spectrum by reintroducing the last term in the Hamiltonian (5.13), $\Delta_3 \equiv \sin(k_z)\gamma_3$. Since k_z commutes with the Hamiltonian and γ_3 anticommutes with the other γ -matrices in the Hamiltonian, the term Δ_3 acts as a mass term for the modes comprising zero-energy subspace in its absence. The corresponding gap is thus $\pm|\sin(k_z)|$ with respect to the zero energy, and in the thermodynamic limit these midgap modes are linearly dispersing along the dislocation line with the velocity set by the hopping in this direction, in agreement with the **K-b-t** rule. These conclusions are schematically shown in Fig. 5.4. By displaying the allowed values of k_z in a finite system, $k_z = 2\pi n/L$, with $L \in \mathbb{Z}$ and $n = 0, 1, 2, \dots, L-1$, on the unit circle in the imaginary plane, the real part characterizes the effective \hat{M}/B , while the imaginary part signals the anticipated energy of the dislocation mode. We note that the shift in \hat{M} indeed ensures that the $T\text{-}p3(4)_R$ phase hosts no dislocation modes with $k_z = 0$ and in the thermodynamic limit all the propagating modes indeed descend from the zero modes at

the band-inversion momentum (π, π, π) , as expected from the **K-b-t** rule.

The above analytical results can easily be verified by numerical computations, and the two show an excellent agreement. In Fig. 5.5 we show the spectrum of a $12 \times 12 \times 12$ system on a torus (periodic boundary conditions) and the real space localization of the dislocation modes. We note that the modes are neatly localized and come as two Kramers pairs, one from the dislocation and one from the anti-dislocation. Moreover, since $\exp(ik_z)$ takes values in the set comprising of the twelfth roots of unity, we can compare the energy gaps with the anticipated $\sin(k_z)$ dependence and find agreement up to two decimals. In addition, we change the mass parameter m to confirm that modes can be added or removed from the spectrum consistent with the condition in Eq. (5.13), see Fig. 5.6. These results reproduce for various sizes of the system (ranging up to 16 sites in linear dimension), confirming the presence of the zero mode together with the descendant propagating states, as predicted by the **K-b-t** rule. Furthermore, when the next-nearest neighbor hoppings are included, the phase $T - p4_M$ protected by both TRS and crystal symmetries with the band inversions at the momenta $(0, \pi, \pi)$, $(\pi, 0, \pi)$, and $(\pi, \pi, 0)$ can be realized, see Fig.5.3. In that case, a dislocation with Burgers vector $\mathbf{b} = a\mathbf{e}_x$ and oriented along the z axis, $\hat{\mathbf{t}} = \mathbf{e}_z$, in both planes $k_z = 0$ and $k_z = \pi$ acts as π -flux, and thus a double Kramers pair is expected. This is indeed what we find numerically, see Fig. 5.7.

It is straightforward to generalize the explained reasoning to other phases. Let us illustrate this with the primitive tetragonal system taking $A_x = A_y = \frac{1}{2}A_z$ and $B_x = B_y = \frac{1}{2}B_z$ in Eq. (5.9). For these parameters we obtain the weak $p4_{M,R}$ phase with band-inversions at M and R points. This phase is displayed in Fig. 5.8, and is not protected by either time-reversal symmetry or a 3D space group symmetry, as opposed to a valley phase. By inserting an edge dislocation with $\mathbf{b} = \mathbf{e}_x$ and $\hat{\mathbf{t}} = \mathbf{e}_z$ we deduce that both time-reversal invariant planes ($k_z = 0, \pi$) orthogonal to $\hat{\mathbf{t}}$ are topologically non-trivial and host a π -flux, yielding zero modes at both momenta $k_z = 0$ and $k_z = \pi$. Therefore, one anticipates a doubled spectrum of descendant propagating modes along the dislocation, according to the **K-b-t** rule. We indeed find these propagating modes numerically and explicitly observe the doubling of the Dirac cones as detailed in Figs. (5.8) and (5.9). We stress, however, that the modes at $k_z = 0, \pi$ are in this case not protected by any symmetry and may therefore be gapped out trivially by relevant perturbations.

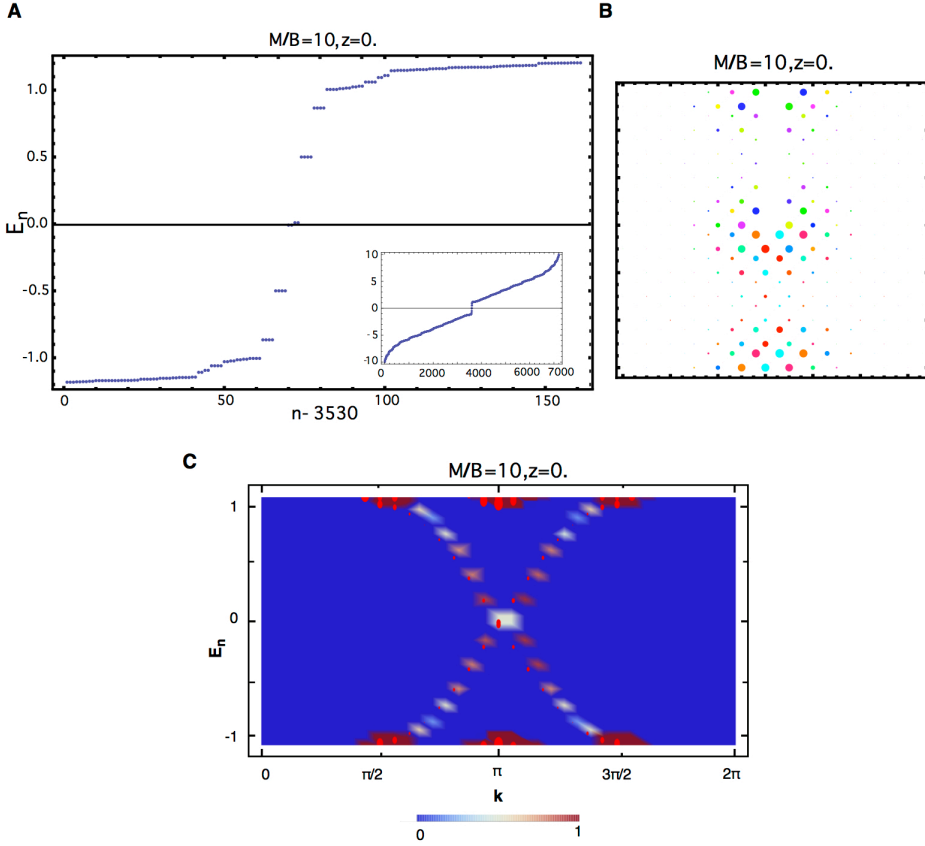


Figure 5.5: The spectrum of the $12 \times 12 \times 12$ system ($M/B = 10$) in the $T\text{-}p3(4)_R$ phase with the edge dislocation with periodic boundary conditions. The dislocation modes come in degenerate Kramers pairs, originating from the dislocation and anti-dislocation (panel A). The inset displays the complete spectrum. We note that the energy levels of these modes in the gap are located at $E_n = 0, \pm E_N = 0.50$ and at $\pm E_N = 0.86$, in agreement with the theory. Panel B shows the real space localization of the dislocation modes for a fixed \mathbf{e}_z plane. The weight of the wavefunction is represented here by the radius of the circles, whereas the color indicates the phase following the same conventions as in Fig 2 in the main text. Due to the translational symmetry, the \mathbf{e}_z planes are identical. Finally, panel C shows the the spectral density as function of the momentum $k = k_z$ along the dislocation line for a $12 \times 12 \times 28$ system. This spectral density is also plotted as circles, where the radius indicates the weight, in order to further emphasize the excellent agreement with numerics.

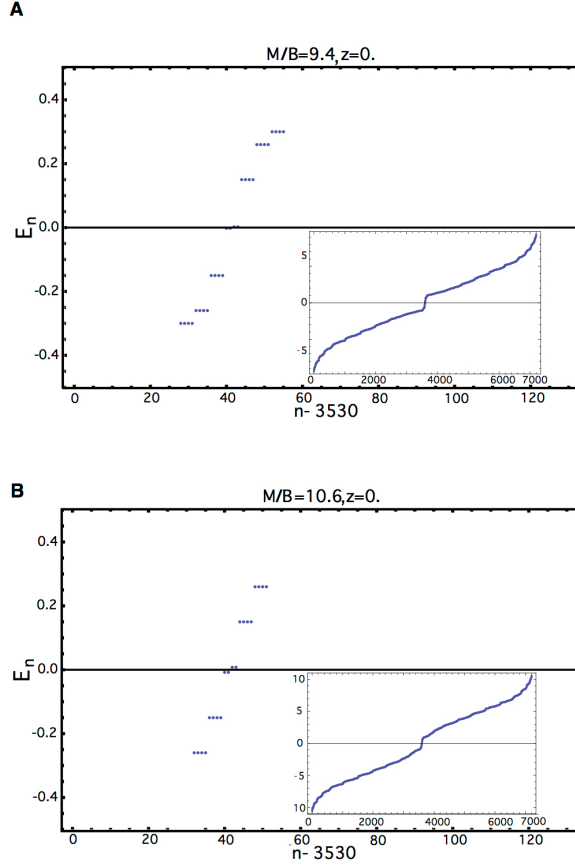


Figure 5.6: The spectra for two $12 \times 12 \times 12$ systems on a torus, with $M/B = 9.4$ and $M/B = 10.6$ in the presence of an edge dislocation with Burgers vector $\mathbf{b} = \mathbf{e}_x$. In this instance A_z was taken to be 0.3, shifting the energy levels to assure that they lie in the gap. The energy levels again take values that match the evaluation outlined above. Moreover, we observe that the $M/B = 9.4$ has one extra level, which is consistent with the mass condition $4 < \hat{M} < 8$.

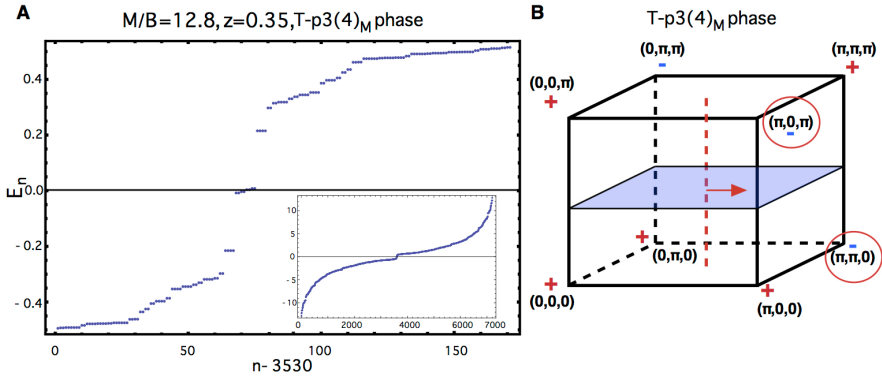


Figure 5.7: *Effect of an edge dislocation in the $T-p3(4)_M$ phase. The right panel shows the topological configuration, with an edge dislocation oriented along the \hat{z} direction and with $\mathbf{b} = \mathbf{e}_x$. The left shows the spectrum, and as expected both $k_z = 0$ and $k_z = \pi$ planes host a π flux yielding two Kramers pairs of zero modes. The resultant energy levels of the descendant states at finite energy are then fourfold degenerate. The modes originating from the $k_z = \pi$ plane result from the corresponding two-dimensional $p4$ phase, whereas the $k_z = 0$ plane is in the $T-p4$ phase.*

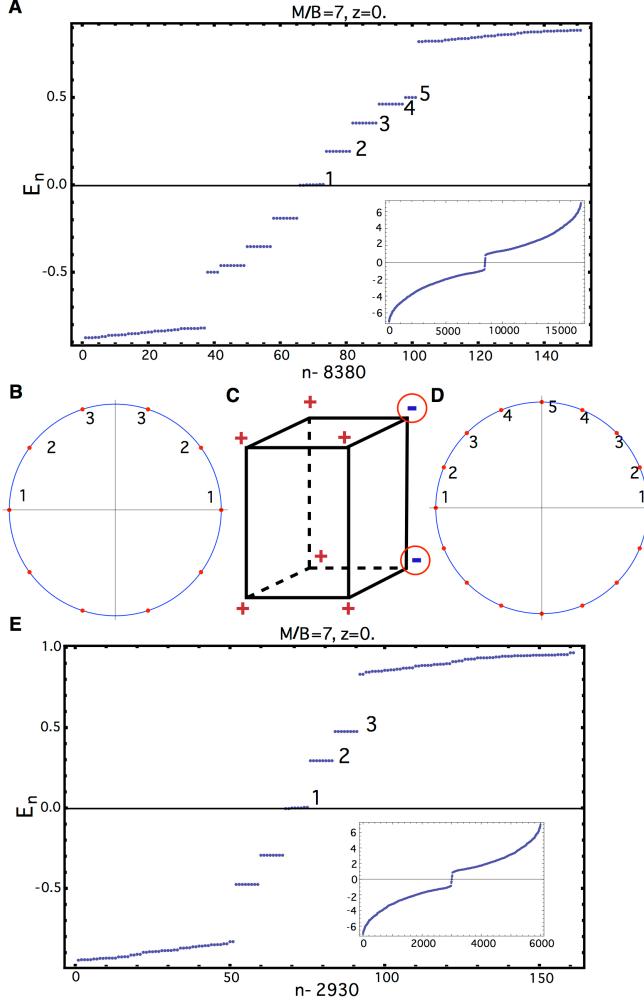


Figure 5.8: The spectra of the tetragonal system with $12 \times 12 \times 12$ (A and E) and a $10 \times 10 \times 10$ (D and E) sites on a torus in the $p4_{M,R}$ phase, with the topological configuration shown in panel C, and an edge dislocation with $\mathbf{b} = \mathbf{e}_x$. We note the eightfold degeneracy per level, consistent with the $\mathbf{K}\text{-}\mathbf{b}\text{-}\mathbf{t}$ rule. Namely as the $k_z = 0$ and $k_z = \pi$ planes host the effective π fluxes, the modes denoted by 1 in panels A and E are indeed localized around the defect as anticipated. Modes 2-5 and 2-3 in the same panels descend from these zero-energy modes with the spectra matching the analytical results.

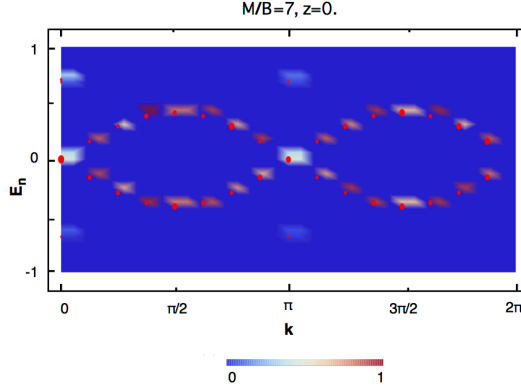


Figure 5.9: The spectral density of the $p_{4M,R}$ phase as function of the momentum $k = k_z$, in case of $16 \times 16 \times 16$ system with periodic boundary conditions. We observe a double Dirac cone situated at $k_z = 0$ and $k_z = \pi$, consistent with the findings in Fig.5.8. Conventions are identical as in Fig.5.5.

5.B.2 Screw dislocations

Three spatial dimensions, in contrast to the two dimensional case, also allow for an orientation of the Burgers vector parallel to the dislocation line. In contrast to the edge dislocation, which is essentially a 2D defect pulled out in the third dimension, the resulting screw dislocation is an intrinsic 3D defect. For a screw dislocation with the Burgers vector oriented along the \hat{z} -axis, $\mathbf{b} = b\mathbf{e}_z$, the vielbeins are given by

$$\hat{E} \equiv E_\alpha^i = \begin{pmatrix} 1 & 0 & 0 \\ 0 & 1 & 0 \\ -\frac{by}{2\pi r^2} & \frac{bx}{2\pi r^2} & 1 \end{pmatrix}, \quad (5.15)$$

and

$$\hat{E}^{-1} \equiv E_i^\alpha = \begin{pmatrix} 1 & 0 & 0 \\ 0 & 1 & 0 \\ \frac{by}{2\pi r^2} & -\frac{bx}{2\pi r^2} & 1 \end{pmatrix}. \quad (5.16)$$

The corresponding distortion field, taking into account that for an elementary dislocation $b = a$, is therefore again given by

$$\boldsymbol{\epsilon}_x = \frac{ay}{2\pi r^2} \mathbf{e}_z = \frac{y}{2\pi r^2} \mathbf{b} \quad \boldsymbol{\epsilon}_y = -\frac{ax}{2\pi r^2} \mathbf{e}_x = -\frac{x}{2\pi r^2} \mathbf{b}, \quad (5.17)$$

resulting in the same gauge potential given by Eq. (5.2) in the main text.

We note nonetheless that for a screw dislocation, the gauge potential can only be finite if $K_{\text{inv},z} \neq 0$. In the case of a screw dislocation, k_z is still a good quantum number, and henceforth we find the same equation for the zero-energy modes and the corresponding descendant states (5.13). In Figs. (5.10) and (5.11), we present the numerical analysis of the spectrum of the Hamiltonian in the $T - p3(4)_R$ phase in the presence of a screw dislocation. We obtain in essence the same spectrum as for the edge dislocation. For various system sizes, we find precisely the number of dislocation modes in the spectrum according to the topological condition below Eq. (5.13). Also, we find that the energy difference between the levels is proportional with the A_z coefficient. We do find however that the energy levels have shifted as compared with the ones obtained in the presence of an edge dislocation in the same phase. Tuning the mass parameter M/B deeper into the phase, (closer to the value of this parameter $M/B = 12$) results in levels closer to the analytically calculated value, as expected from the finite-size effects, and the fact that the matrix elements are now twisted with a factor e^{ik_z} along the dislocation direction. We observe in addition that, in general, the form of the underlying metric $ds^2 = dr^2 + r^2 d\vartheta^2 + (dz + \beta d\vartheta)^2$ may be mapped with $z \rightarrow z + \beta\theta$ to a flat space with non-trivial quasi-periodic boundary conditions, which indeed result in energy shifts, which we do not explicitly compute here but this in principle can be done using the outlined procedure.

In the translationally active $T-p3(4)_M$ phase, obtained from the Hamiltonian (5.8) and for the values of the parameters as shown in Fig. 5.3, a screw dislocation with the Burgers vector $\mathbf{b} = \mathbf{e}_x$ produces π fluxes in the plane $k_x = \pi$, which hosts a valley phase. Therefore, according to the **K-b-t** rule, we expect two Kramers pairs of the dislocation modes originating from the band-inversion at the M and the X' points. Our numerical computations indeed confirm this prediction, as shown in Fig.5.12.

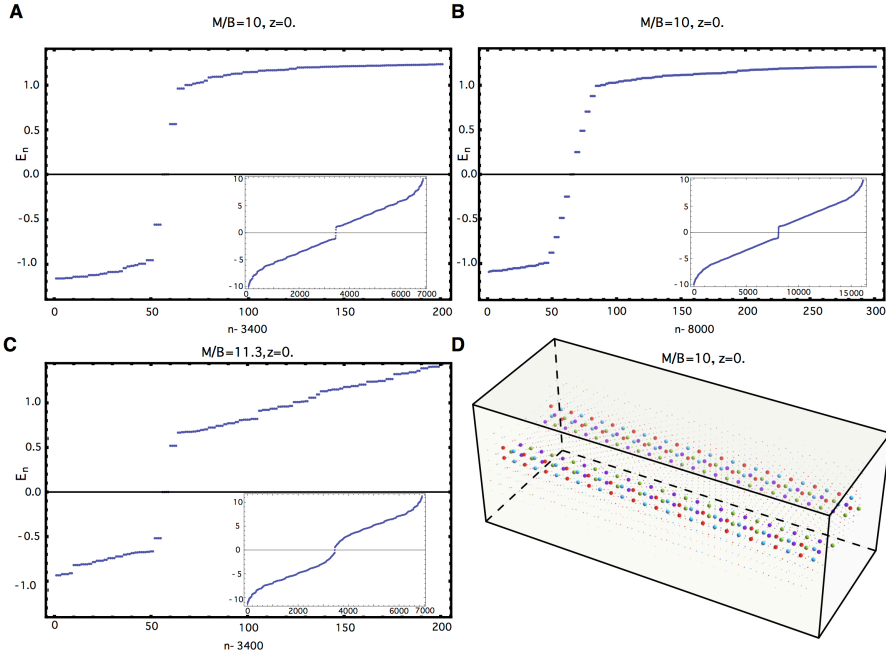


Figure 5.10: Numerical results concerning the effect of a screw dislocation, with $\mathbf{b} = \mathbf{e}_x$ oriented in the \mathbf{e}_x direction. Panel A shows the spectrum of the modes on a $12 \times 12 \times 12$ system with periodic boundary conditions. The modes are not exactly at ± 0.50 as expected from the continuum model. The deviation of the energy levels from the anticipated value as obtained from the analytical treatment becomes smaller for larger systems sizes. Panel B shows a $28 \times 12 \times 12$ system showing that the splitting of the energy levels converges to the result from the continuum model. Similarly the agreement with numerical results is also better in the $T - p4(3)_R$ phase when the system is closer to the transition point $M/B = 12$ (C). Finally panel D shows the real space localization of the mode with the color coding shown above.

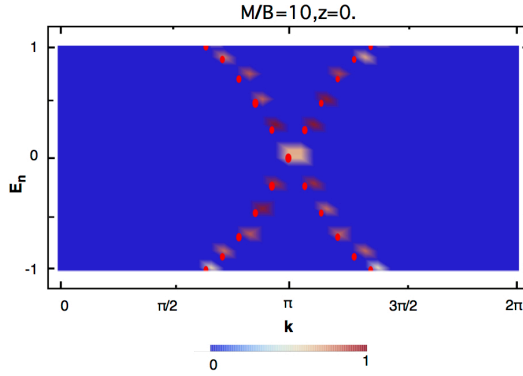


Figure 5.11: *The spectral density of a screw dislocation, with Burgers vector \mathbf{e}_x , in the $T\text{-}p3(4)_R$ phase of a $28 \times 12 \times 12$ system with periodic boundary conditions. The presentation is similar to the above Figures. The horizontal axis shows the momentum $k = k_x$ along the dislocation line. Although the energy levels are shifted due to the finite size of the system, the spectrum displays again a zero mode at $k_x = \pi$ and the expected number of descendant states that form a Dirac cone, analogous to the case of an edge dislocation.*

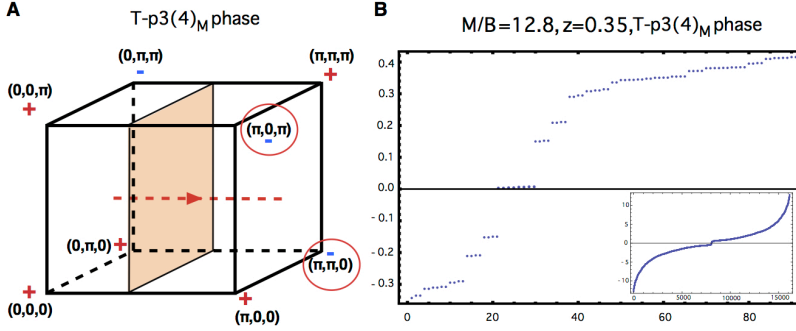


Figure 5.12: Numerical results concerning the effect of a screw dislocation in the $T\text{-}p3(4)_M$ phase. (A) The topological configuration of the $T\text{-}p3(4)_M$ phase. The screw dislocation, with Burgers vector $\mathbf{b} = \mathbf{e}_x$, acts on the encircled TRI momenta in the $\hat{y} - \hat{z}$ planes. (B) The resulting spectrum of a $28 \times 12 \times 12$ system with periodic boundary condition in the $T\text{-}p3(4)_M$ phase. The resulting spectrum shows a double pair of 'parent' helical zero modes. These modes originate from the encircled momenta, which form a 2D valley phase in the plane $k_x = \pi$, since these momenta are related by a threefold rotation around the axis connecting the Γ and the R points.

Let us now consider a dislocation loop, which can be thought of as a connected channel of screw and edge dislocations. Although the Burgers vector \mathbf{b} of any dislocation remains constant [114, 116], the planes orthogonal to the dislocation line are different for the edge and screw dislocation part of the circuit. In general one can consider the full scattering problem of an edge and screw dislocation [145, 146], which essentially pertains to matching the phases of the solutions of Eq. (5.13). Due to time-reversal symmetry, however, the helical modes are protect from backscattering, and we can thus conclude that dislocation loops have helical modes along the core when both the edge and the screw dislocation possess the propagating modes. We emphasize the implications of the $\mathbf{K-b-t}$ rule in this regard, dictating the precise existence criteria of the dislocation modes in the loop. Accordingly, the $T\text{-}p3(4)_R$ phase with a dislocation loop, see Fig (5.4), has dislocation modes along the loop for any orientation of the Burgers vector \mathbf{b} . In contrast, inserting a dislocation loop in the $\hat{x} - \hat{z}$ plane, with $\mathbf{b} = \mathbf{e}_x$, in the $p4_{M,R}$ phase only binds dislocation modes to the edge dislocation part of the circuit, resulting in the exact same spectrum shown in Fig. 5.8. Changing the orientation of the Burgers vector to \mathbf{e}_z then does result in dislocation modes along the loop, as the gauge

potential \mathbf{A} is non-trivial in all the planes normal to the dislocation lines and these planes are topologically non-trivial. At last, changing the Burgers vector to the \mathbf{e}_y direction, it is evident that the effective systems in each plane either has no flux or acquires 2π -flux. As a result we anticipate no modes, analogously to the case of a screw dislocation with $\mathbf{b} = \mathbf{e}_x$, which is confirmed by numerical computations, see Fig. 5.13.

Finally, we address the full compatibility of the outlined analysis with the underlying characterization of topological insulators with different space groups in terms of the band-inversions. Consider, for example, the composite phase $T-pm\bar{3}m \oplus T-4p3_X$, which is equivalent to the $T-4p3_M \oplus T-4p3_R$ or $\Gamma \oplus XYZ = MX'Y' \oplus R$ phase with the dislocation loop in the $y-z$ plane, as previously described, see Fig. 5.13. We expect here the response of the dislocations to be the same with both choices of the band-inversions. We see that upon applying the $\mathbf{K-b-t}$ rule to either set of the band inversions, one indeed obtains the same outcome in terms of the fluxes acting on the planes. Along the edge dislocation, the $k_z = 0$ plane hosts a π flux, in contrast to the $k_z = \pi$ plane. Similarly, for the screw dislocation part, which has momentum in the k_x direction, we see that the $k_x = \pi$ plane hosts a zero mode. Note that in the latter case, the screw dislocation acts as a π -flux in this phase, which with respect to the $k_x = \pi$ plane, may be thought of as the $T-p4mm$ or Γ phase, since the $(\pi, 0, 0)$ momentum acts as a Γ point in this plane. The descendant values of k_x thus contribute dislocation modes to the spectrum as long as the effective M/B parameter in the reduced model is in the range corresponding to the $T-p4mm$ in 2D. As result, we find that the complete dislocation loop has modes along the core.

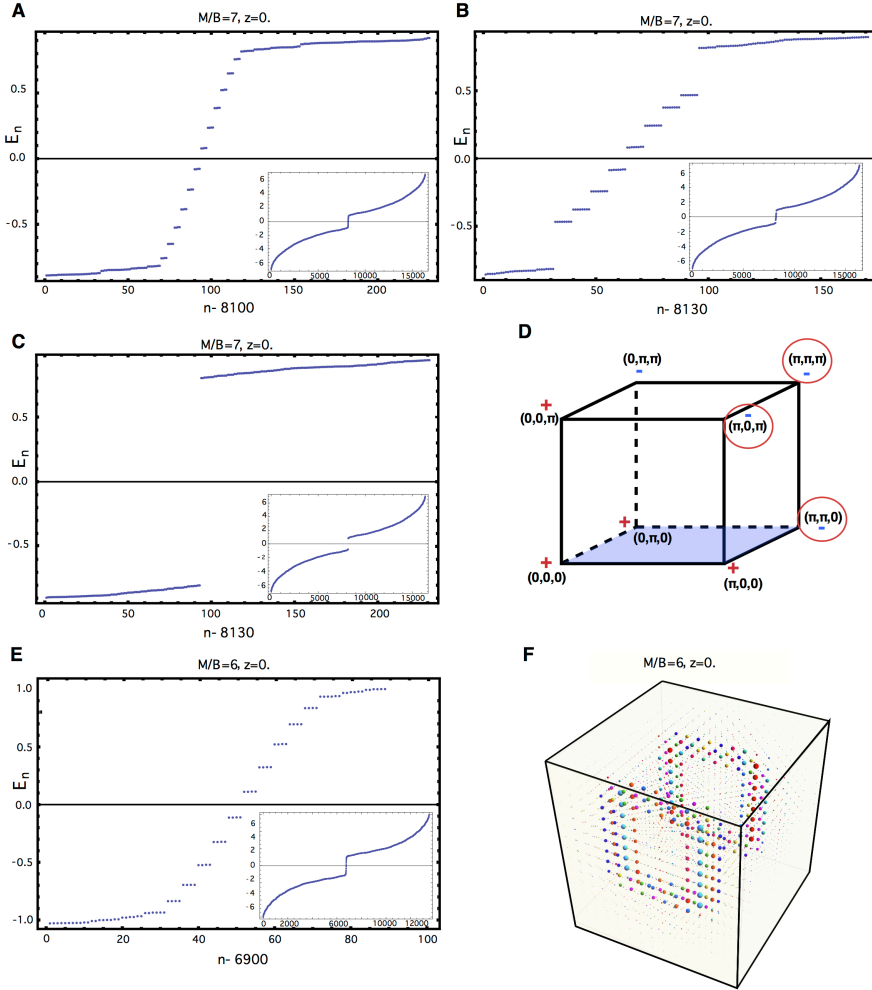


Figure 5.13: Dislocation loop in the $\hat{x}-\hat{z}$ plane with Burgers vector $\mathbf{b} = \mathbf{e}_x$. Panels A to C show the spectra corresponding to the dislocation loops in Fig. 5.1 in the main text. Namely, considering systems with periodic boundary conditions, we tune the system to the respective phases and get the anticipated dislocation modes in the spectrum. Panel D indicates the electronic topological configuration of the $T-4p3_M \oplus T-4p3_R$ phase. As each plane hosts an effective π -flux problem, inserting the same dislocation loops gives the anticipated spectrum (E), the modes of which show the familiar real space localization (F).

Chapter 6

Isospinless graphene on grain boundaries in topological band insulators

The mathematical description of any generic symmetry protected state of matter finds its robustness in the incompressibility of the underlying phase. Nonetheless, as detailed in the previous Chapters, the associated profound physical consequences of these topological entities in fact revolve around the appearance of anomalous *gapless* degrees of freedom that confine to boundary surfaces of a certain finite codimension. Turning to the \mathbb{Z}_2 topological insulator, for instance, the non-trivial order is necessarily accompanied by two spatially separated Kramers pairs of edge states, the existence of which then provides for an explicit indication of the topological characterization.

More recently, it became apparent that these correspondences can be exploited further, providing for a viable route of deducing derived topological notions to characterize semi-metallic band structures [147]. To make this more specific, consider a band structure over a three dimensional Brillouin zone T^3 that comprises two bands, touching at a finite number of isolated points. As subtracting a \mathbb{C} -number from the Hamiltonian does not effect the qualitative features, it is evident that the relevant mapping may be parameterized as usual,

$$H(k_x, k_y, k_z) = \mathbf{d}(\mathbf{k}) \cdot \boldsymbol{\tau}, \quad (6.1)$$

in terms of the Pauli matrices $\boldsymbol{\tau}$. Using this specific form, one can then imagine drawing a small spherical surface S_a , enclosing a single nodal point \mathbf{k}_a , and subsequently define a mapping from S_a into the Bloch space of Hamiltonians by considering the unit vector $\hat{\mathbf{d}}(\mathbf{k}) = \mathbf{d}(\mathbf{k})/|\mathbf{d}(\mathbf{k})|$. This mapping is well-defined on the specified surface and from a

topological point of view maps the two-sphere S^2 to itself. Therefore, in direct analogy with Eq. (2.5), this construction immediately gives rise to a topological invariant or winding number $w_a \in \pi_2(S^2) \cong \mathbb{Z}$ that is physically associated with the Berry-flux originating from the nodal point, acting as a monopole in this regard. We notice, however, that in this case the Nielsen-Ninomiya theorem [33, 34] cannot be evaded and consequently restricts the total sum of winding numbers, affiliated with all nodal points, identically to zero. As a matter of fact, the relation manifests in the case at hand a deep rooting of the doubling property in the geometry of the underlying manifold, which can readily be shown upon application of the efficient machinery of differential forms on the manifold \tilde{T}^3 , being the Brillouin zone T^3 from which the open balls U_a satisfying $\partial U_a = S_a$ are removed. In particular, denoting the two-sphere associated with $\hat{\mathbf{d}}(\mathbf{k})$ as $S_{\mathbf{d}}$, the winding number w_a is expressed as a pullback integral [25, 148]

$$w_a(S_a) = \int \phi^*(\alpha), \quad (6.2)$$

in terms of the function $\phi : S_a \rightarrow S_{\mathbf{d}}$ and the standard closed volume form α , obeying $\int_{S_{\mathbf{d}}} \alpha = 1$. Invoking Stokes's theorem and using that $\partial \tilde{T}^3 = \cup S_a$, one then promptly obtains

$$0 = \int_{\tilde{T}^3} \phi^*(d\alpha) = \int_{\tilde{T}^3} d\phi^*(\alpha) = \sum_a \int_{S_a} \phi^*(\alpha) = \sum_a w_a(S_a), \quad (6.3)$$

directly conveying the intricate relation between the fermion-doubling theorem and the homology of the underlying manifold in this scenario.

From a physical perspective, the outlined bulk system is commonly referred to as a Weyl semi-metal, reflecting the emergence of the Weyl equation as the effective continuum description in the vicinity of such a Fermi point, and entails an obvious generalization of the graphene model (1.6). Analogous to its lower dimensional counterpart, Weyl semi-metals also show exotic electronic transport features, including so-called Fermi arcs that heuristically pertain to gapless edge states connecting projected nodes of opposite chirality in momentum space [147], and find an evident correspondence to \mathbb{Z}_2 topological insulators (TBIs). Nonetheless, although the energy spectra in all cases resemble each other, the *stability* of their band structures has a dramatically different origin. Namely, in graphene and Weyl semi-metals the stability of the Fermi surface relies on the presence of fine-tuned *lattice symmetries*, while in topological band insulators the surface states inherit a robust protection from the *topology* of the bulk band structure. Therefore, it is of both fundamental and practical importance to answer the natural question whether there are realizations, other than the familiar edge modes, where a Dirac or

Weyl semi-metallic band structure emerges that does not require any fine-tuning or the application of external fields.

In this Chapter, we bridge this divide by showing that a topologically protected 1D semi-metal exhibiting a valley anomaly and a 2D semi-metal featuring an odd-integer quantum Hall effect – the isospinless graphene – can emerge and be experimentally observed on extended defects in \mathbb{Z}_2 topological insulators (TBIs). In particular, these states emerge on a grain boundary, a ubiquitous lattice defect in any crystalline material, thereby providing a novel and experimentally accessible route to topological semi-metals. Moreover, as the underlying mechanism capitalizes on the previous obtained insights by pertaining to the hybridization of spinon dislocation modes bound to grain boundaries, these results also accentuate the potential physical content of the above ideas and suggest that its associated generality can culminate in the emergence of new states of matter in any topological band insulator where lattice dislocations bind localized topological modes.

6.1 General principles underlying the emergence of semi-metals at grain boundaries

We here establish the general principles demonstrating that grain boundaries (GBs) can host time-reversal symmetry (TRS) protected topological semi-metals. Although, it is known that interfaces connecting TBIs can accommodate modes in the presence of a protecting mirror symmetry [149], grain boundaries have a real topological status in the crystal geometry [116, 150]. They arise at the interface of two crystal regions whose lattice vectors are misaligned by an angle θ , as illustrated in Fig. 6.1(A), and for small opening angles may be viewed as a stack of lattice dislocations described by a Burgers vector \mathbf{b} arranged on an array of spacing $d = |\mathbf{b}|/(\tan \theta)$. While grain boundaries are usually considered detrimental for their properties, they have actually been of experimental use as probes of the superconducting state in high-temperature superconductors [151, 152, 153]. In addition, they have recently been suggested for engineering thermoelectric devices [154] and for experimentally tuning the surface states in a 3D TBI [155]. Of topical interest, however, is the observation that GBs provide for an experimentally viable setting for the mobilization of the previously derived dislocation modes, serving as building blocks for new states of matter without requiring lattice symmetries or fine-

tuning. These emergent semi-metals may, from a heuristic perspective, be viewed as “halved” graphene-like states, that have lost their isospin degeneracy, and are intimately connected to the TBI surface states that can be controlled by applying external fields: 1D GBs in the bulk of a 2D TBIs exhibit a valley anomaly that under an applied electric field results in a spin imbalance of the TBI edge states on the different sides of the GB, while 2D GBs in 3D TBIs are characterized by an odd-integer quantum Hall effect.

Before proceeding to the 3D case, let us first discuss the general features of the mechanism in the more accessible setting of a 2D TBI. We assume hereafter that the TBI is prepared in a topological phase characterized by an odd number of band inversions at TRS momenta other than the Γ -point in the BZ, i.e. the translationally active phase. As detailed before, a lattice dislocation then acts as an effective magnetic π -flux and as a result binds a *single* Kramers pair of zero energy spinon modes localized to the core. Figure 6.1 shows that once this necessary condition is satisfied, a GB in such material supports a 1D propagating mode that is localized along it. Specifically, this state appears in the energy spectrum as a gapless mid-gap ‘bow-tie’ band that exhibits two non-degenerate nodes, reminiscent of the valleys in graphene. These nodes appear at the TRS momenta along the GB and persist for all GB angles including the maximal opening angle of $\theta = 45^\circ$. Thus for a neutral GB where the chemical potential is at the nodes, a one-dimensional graphene-like semi-metal emerges.

The microscopic mechanism underlying the emergence of this state is the hybridization of topological spinon modes, acting as effective π -flux modes, bound to the lattice dislocations that form the GB. When brought into proximity, the spinon modes hybridize between dislocations giving rise to a nearest-neighbour spinon hopping term of magnitude t . As detailed in Appendix 6.A, a translationally invariant GB can then be modeled in terms of a simple TRS tight-binding model by virtue of the incompressibility of the parent system, resulting in a momentum space Hamiltonian of the general form

$$H(q) = \mathbf{h}(q) \cdot \boldsymbol{\sigma}. \quad (6.4)$$

More importantly, as the Pauli matrices $\boldsymbol{\sigma}$ act in *spin space*, the presence of time reversal symmetry in turn requires $H(-q) = -H(q)$, resulting in the vanishing of $H(q)$ at the TRS momenta $q = 0$ and $q = \pi$ on general grounds. In the full TBI where the presence of a GB oriented in \hat{x} -direction has translational symmetry only with respect to the dislocation spacing d , these TRS momenta correspond to $k_x = 0$ and $k_x = \pi/d$. Hence, the spinons hybridize into two helical bands, one for each spin component, that are

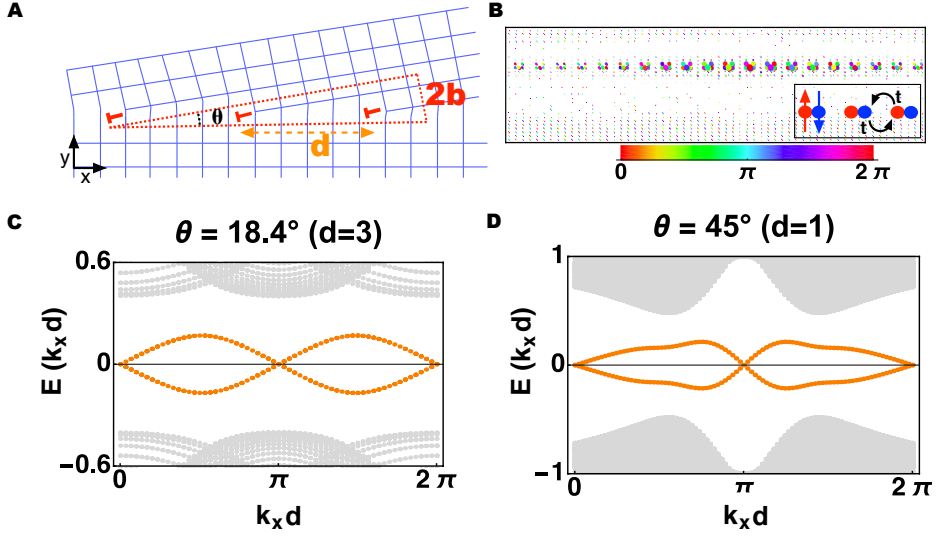


Figure 6.1: Graphene-like semi-metal on a 1D grain boundary in a translationally active 2D TBI (M-phase of the M-B model on a square lattice). (A) Schematic illustration of a GB. The coordination discrepancy due to the angular mismatch θ of lattice basis vectors results in an effective array of dislocations, each described by Burgers vector \mathbf{b} and marked by a 'T' symbol, of spacing $d = |\mathbf{b}|/\tan \theta$. (B) Real space numerical tight-binding calculation of the low-energy states in the presence of a GB. The spinons bound to the dislocations hybridize with tunneling amplitude t , which gives rise to an extended 1D state along the GB. The radii of the circles indicate the amplitude of a wave function, associated with the node at $k_x = \pi/d$ of panel (C), while the colors indicate the phase. (C) the characteristic mid-gap bow-tie dispersion of the spinon bands (orange) and bulk bands (grey), corresponding to GB opening angle $\theta = 18.4^\circ$ for which isolated dislocations along the GB are well defined, as the function of the momentum $0 \leq k_x \leq 2\pi/d$ along the GB. (D) The same plot for the maximal opening angle $\theta = 45^\circ$. While the picture of isolated dislocations breaks down and the simple nearest-neighbour hybridization based sinusoidal dispersion is lost, the defining TRS semi-metal dispersion with the nodes at the time-reversal symmetric momenta survives. The data pertain to 30×60 site or larger systems with periodic boundary conditions.

odd in momentum and feature TRS protected nodes at the two TRS invariant momenta, fulfilling the fermion doubling theorem [33, 34] by virtue of the nodal separation in momentum space. Accordingly, and consistent with our results in Figure 6.1, the spinon hybridization gives then rise to an emergent *helical spinon mid-gap band* with the exotic bow-tie dispersion $E_{\pm}(q) = \pm 2t \sin(q)$. We have verified (see Appendix 6.A.1) that for a wide range of GB angles θ the simple nearest neighbour tight-binding model indeed accurately approximates this dispersion with the two-dislocation hybridization energy $\varepsilon \sim t$ as the only input, verifying the outlined analysis.

To derive a more concrete effective model for the hybridization induced dynamics, we may employ an alternative heuristic soliton construction for the dislocation bound spinons that relies only on the existence of edge states originating from the band inversion momenta \mathbf{K}_i and their symmetries [138]. The generality with respect to the underlying topology of the parent state is then recovered by the $\mathbf{K}\text{-}\mathbf{b}\text{-}\mathbf{t}$ rule, as it unambiguously conveys the edge states relevant to construct the spinon modes in this context. To illustrate this, consider a system of two coupled helical edges along the \hat{y} -axis described by the Hamiltonian $H_0 = v\tilde{k}_y\mu_z \otimes \sigma_z + m\mu_x \otimes \sigma_0$. Here σ_z acts in spin space, while $\mu_z = \pm 1$ denotes the two edges. Furthermore the dispersion $v\tilde{k}_y$ is given in terms of the effective momentum \tilde{k}_y , being the effective momentum in the vicinity of the projection of the band inversion \mathbf{K}_{inv} . In general, a tunnelling of magnitude m gaps out the edge states at the interface of the two TBIs. However, when an additional row of atoms for $y > 0$ is inserted between the edges, or equivalently a dislocation with Burgers vector $\mathbf{b} = \mathbf{e}_x$ is created at $y = 0$, the mass term for $y > 0$ becomes $me^{i\sum_i \mathbf{K}_i \cdot \mathbf{b}}$. In a translationally active phase $\sum_i \mathbf{K}_i \cdot \mathbf{b} = \pi \pmod{2\pi}$ and thus the sign of the edge state tunneling becomes y -dependent. The system is therefore equivalent to the 1D continuum SSH model discussed in the introductory Chapters. Hence, it is evident that in a TRS system the domain wall binds a Kramers pair of localized spinons, which represent the dislocation modes and live for the Hamiltonian H_0 in a subspace described by the projector $P = (1 + \mu_y \otimes \sigma_z)/2$.

Using this construction, the adjacent edge states then couple by a translationally and TRS invariant Hamiltonian $H_{GB} = 2t[\cos(q)\mu_x \otimes \sigma_0 + \sin(q)\mu_y \otimes \sigma_0]$, where q spans as before the reduced Brillouin zone $k_x = 0 \geq q \geq k_x = 2\pi/d$, and we only took into account nearest neighbor hopping. Projecting this coupling into the spinon subspace, consistent with our prediction, we find that the spinons acquire a dynamics described by $P(H_0 + H_{GB})P = 2t \sin(q)\tilde{\sigma}_z$, where $\tilde{\sigma}_z$ entails an effective spin operator in the spinon

subspace (see Appendix 6.A.3). Moreover, we can heuristically consider the effect of S_z conservation breaking via a Rashba term, the effects of which we model by $H_R = \alpha k_y \mu_z \otimes \sigma_y$, and TRS breaking via the introduction of Zeeman terms $H_B = \sum_i b_i \mu_0 \otimes \sigma_i$. Projecting these into the spinon subspace yields an minimal effective model of the form (see Appendix 6.A.3)

$$H_{2D} = \left(\frac{v b_z + \alpha b_y}{\sqrt{v^2 + \alpha^2}} + 2t \sin(q) \right) \tilde{\sigma}_z, \quad (6.5)$$

which connects qualitatively to our numerics. That is, the construction reflects that for Rashba couplings not strong enough to close the gap the nodal spectrum persists and that Zeeman terms normal to GB need a finite Rashba coupling to have an effect.

This mechanism generalizes directly to 3D translationally active phases. As illustrated in Figure 6.2(A), for small angles θ a 2D GB can now be viewed as an array of parallel 1D edge dislocations, each of which effectively realizes a π -flux tube and hosts a pair of counter-propagating helical modes of velocity v_f . Letting k_z (k_x) denote the momentum parallel (transverse) to the dislocation lines, Figure 6.2(B) shows that the 2D GB in a 3D bulk TBI supports a graphene-like state with two non-degenerate linearly vanishing nodes at the two TRS momenta $(k_x, k_z) = (0, \pi)$ and $(\pi/d, \pi)$. Like in the 2D case, the emergence of this state can be understood in terms of pairwise hybridization of amplitude t of the adjacent helical modes. To derive a minimal effective model for their hybridization, we therefore again exploit the model-independent surface state construction that couples adjacent surfaces. In the geometry of Figure 6.2(A), this culminates in the Hamiltonian $H_0 = v_f (\tilde{k}_y \mu_z \otimes \sigma_y + \tilde{k}_z \mu_z \otimes \sigma_z) \mu^z + m(y) \mu_x \otimes \sigma_0 + H_{GB}$. Analogous to the 2D case, we then project this Hamiltonian into the spinon subspace, which in the presence of TRS breaking Zeeman terms $H_B = \sum_i b_i \mu_0 \otimes \sigma_i$ gives the general minimal model (see Appendices 6.A and 6.A.3)

$$H_{3D} = v_f \tilde{k}_z \tilde{\sigma}_z + (b_y + 2t \sin(q)) \tilde{\sigma}_x, \quad (6.6)$$

where the effective $\tilde{\sigma}$ matrices again act in spin space and \tilde{k}_z is again understood as the effective momentum. Consistent with Figure (6.2)B, this thus yields the anticipated helical semi-metallic state. We accentuate in this regard the opposite chirality of both emergent cones. This relates to the interpretation of the fermion doubling theorem [33, 34] described above and the similar topological entity of the parent TBI at either side of the grain boundary, as in the 2D case. There are, nonetheless, also two notable differences

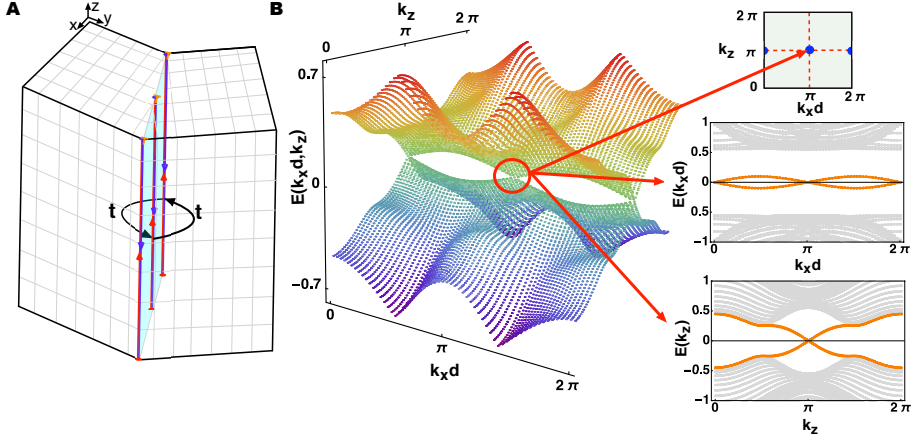


Figure 6.2: Graphene-like semi-metal localized on a 2D grain boundary in a translationally active 3D topological band insulator (*R*-phase on a cubic lattice). (A) Schematic illustration of the 2D GB, which now realizes a sheet of hybridizing parallel 1D edge dislocation lines that extend along the grain boundary. Each edge dislocation hosts a pair of propagating helical modes localized along the dislocation cores that cross at $k_z = \pi$. (B) On a GB of opening angle 18.4° , the hybridization of the helical modes results in the semi-metal band structure with two anisotropic pseudo-relativistic fermions at $(k_x, k_z) = (0, \pi)$ and $(\pi/d, \pi)$. Along the GB we recover the same mid-gap bow-tie dispersion as in the 2D case (shown top right for $k_z = \pi$), while along the edge dislocations the hybridized modes (orange) still flow into the bulk bands (gray) as a function of k_z (bottom right for $k_x = \pi/d$). The data pertain to $60 \times 60 \times 90$ systems with periodic boundary conditions.

to the 2D case: (i) The 2D graphene-like state localized along the GB is now not an isolated mid-gap band, but flows into the bulk bands due to the helical nature of the hybridizing modes, i.e. it is a property of the whole 3D bulk, and (ii) the dispersion is now two-dimensional, but with anisotropic velocities v_f along and $2t$ perpendicular to the dislocation lines, respectively. This anisotropy is reduced for larger opening angles θ due to an enhanced overlap of the helical modes. Finally, we note that, as with the 2D case, the semi-metal is stable in the presence of moderate disorder and the cones can only be gapped with a TRS breaking Zeeman term normal to the GB plane. This stability is the subject of the next Section.

6.2 Stability of the spinon metal

We now turn to the question to what extent these GB modes are stable and detail the underlying protection mechanism, which is inherited from the time-reversal symmetry of the parent TBI. As perturbations that do not break TRS, we have considered both Rashba spin-orbit coupling and local chemical potential disorder in the 2D TBI (see Appendix 6.B). Unless strong enough to close the bulk band gap, the Rashba coupling only deforms the hybridized bow-tie spectrum resulting in slightly different velocities at the nodes at the two TRS momenta. This stability follows from the Rashba term only modifying the spinon wavefunctions, while a gapping mass term is forbidden due to TRS. On the other hand, as in weak topological insulators with an even number of surface states, local random disorder can in principle gap the cones by inducing inter-valley scattering. Our numerical analysis shows that substantial spatial disorder is nonetheless tolerated, which can be understood in terms of disorder inducing local random deformations on the localized spinon wavefunctions. This translates into a random hopping problem for the spinons along the GB, governed by an effective gauge field shifting the cones in momentum space [156]. As long as this shift is smaller than the separation π/d of the cones in the BZ, the semi-metallic behavior is stable. As a consequence, a larger opening angle of the GB adds to the stability of these states against disorder. Similarly, random spinon tunneling can also result from bends along the GB. Hence, based on the principles just outlined, we expect the semi-metallic state to persist also in the absence of perfect translational symmetry along the GB. Moreover, TRS implies that, unlike normal fermions in 1D, the spinons on a GB are immune to Anderson localization [157]: a

localizing random chemical potential for the spinons requires a TRS breaking random Zeeman term. Regarding the influence of TRS breaking Zeeman terms, we find that the spinon semi-metal remains nodal as long as no mass term for the isolated spinons is introduced (see Appendices 6.A and 6.B). This once again signifies the intricate role of the topology of the parent \mathbb{Z}_2 state. Namely, the stability of the semi-metal is directly associated with the stability of the dislocation modes composing it, which in turn directly root in the non-trivial bulk entity. This directly corresponds with the intuition of the above arguments.

6.3 Experimental signatures

Let us now address the distinct experimental signatures characterizing GB semi-metals. To detect the graphene-like spinon semi-metal on the 1D GB inside a 2D TBI, one can carry out a two terminal transport measurement analogous to the one used to detect edge states in a 2D quantum spin Hall insulator [41]. When an electric field \mathbf{E} is applied along the GB, due to the two cones one should observe conductance of $\sigma = 4e^2/h$, i.e. twice the value measured for the QSH edge states. A more dramatic consequence of the helical bow-tie dispersion along a 1D GB is the existence of the parity anomaly [158] for each spin projection. In the presence of two chiral cones, it gives rise to a *valley anomaly*. As illustrated in Fig. 6.3(A), an electric field \mathbf{E} along the GB generates a current for both spin components that results in one valley having excess of spin up and the other spin down. As the valleys can be associated with two distinct channels through which the helical edge states can flow from one GB termination surface to the other, the valley anomaly gives rise to the spin polarization of the edge currents at different sides of the GB. This spin imbalance as a result of applied electric field is proportional to the hybridization strength $2t$ and it represents a hallmark signature of valley anomaly that originates from the parity anomaly for each spin component of the GB semi-metal. To detect it, one can carry out a two-terminal edge transport measurement illustrated in Fig. 6.3(A). When the two edges connected by the GB are biased by voltage V , one expects net current $I \sim 2t \frac{4e^2}{h} V$ reflecting unequal spin currents. Alternatively, the valley anomaly could be detected by measuring the magnetic moment due to spin imbalance [159] or using Kerr rotation microscopy [160, 161].

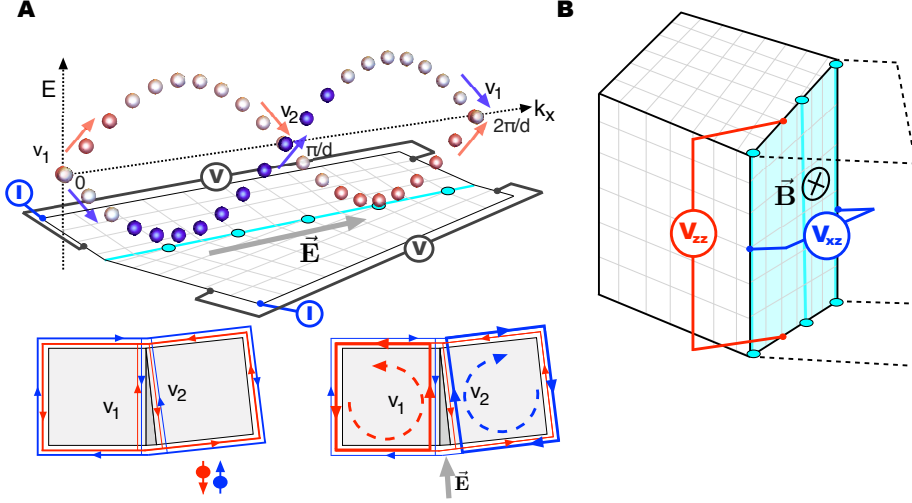


Figure 6.3: The experimental setups to identify the signatures of the isospinless graphene state. (A) the one-dimensional bow-tie dispersion of the spinon semi-metal on a 1D GB implies a parity anomaly when an electric field \vec{E} is applied along the grain boundary. The arrows indicate the shift in the spectrum from one valley to the other: Valley V_1 accumulates an excess of spin down (red), while valley V_2 accumulates excess spin up (blue). These valleys can be associated with two helical two-mode channels that connect the helical edge states from opposing surfaces. When \vec{E} is applied along the GB, a current for both spin orientations is driven parallel to it. At the GB edges this current flows into the edge states that propagate to opposite directions resulting in a doubled spin Hall effect-like spin imbalance of the edge states on the two sides of the GB. Measuring this imbalance is the hallmark signature of the valley anomaly exhibited by the spinon semi-metal. (B) The spinon semi-metal on a 2D GB – the isospinless graphene – features an odd integer Hall effect with transverse conductivity $\sigma_{xz} = (2n+1)e^2/h$ in the presence of the perpendicular magnetic field \vec{B} . In the absence of external fields, another signature is provided by the diagonal ballistic optical conductivity of $\sigma_{zz} = (\pi/4)e^2/h$, which is half that of graphene.

Although, the isospinless graphene on a 2D GB can also be viewed as two helical channels that connect the surface states of the 3D TBI and are hence anticipated to give rise to a smilier spin-pumping effect, it is experimentally most conveniently detected via two distinct "half-graphene" -like signatures. When a magnetic field is applied perpendicular to the GB in the setup shown in Fig. 6.3(B), the non-degeneracy of each cone implies a contribution of $(n + 1/2)e^2/h$ to the Hall conductivity, which in turn implies odd-integer quantum Hall effect with total Hall conductivity $\sigma_{xz} = (2n + 1)e^2/h$. In addition, in the absence of the magnetic field, the measured ballistic optical conductivity is $\sigma_{zz} = (\pi/4)e^2/h$, which is half the value measured in graphene [162]. Finally, we also expect the semi-metal to exhibit edge states that should contribute additional Fermi arc-like features to the surface states of the parent 3D TBI (see Appendix 6.A.2). Nonetheless, their detection is likely to be challenging.

6.4 Conclusions

In conclusion, we have shown that TRS protected semi-metals, encompassing helical wires exhibiting a valley anomaly and isospinless graphene states featuring an odd-integer quantum Hall effect, can emerge naturally on grain boundaries in \mathbb{Z}_2 topological band insulators. The only requirement for the parent TBI lies in the condition to be of the translationally active type where lattice dislocations bind a Kramers pair of spinons. The hybridization of these defect modes along the grain boundary then provides for the general mechanism underlying the emergence of these novel kinds of topological semi-metals. As grain boundaries occur naturally in crystalline samples, the challenge is to identify translationally active materials, although a convenient guide to candidates is in fact provided the space group classification. Here we have used the *M*- and *R*-phases of the 2D square and 3D cubic lattice, respectively, for modeling purposes, with the latter having a potential realization in electron doped BaBiO₂ [143]. Nonetheless, the outlined mechanism is completely general and available transitionally active candidates include Bi_xSb_{1-x} [42], the topological Kondo insulator SmB₆ featuring band inversions at the three *X* points [163, 164], and the topological crystalline insulating state in Sn-based compounds exhibiting band inversions at the *L*-points in the Brillouin zone as long as the protecting crystalline symmetry is respected [127, 144].

Although GBs provide a natural setting for arrays of topological spinons, the mech-

anism of their hybridization applies to any system where such an array can be realized. In topological states associated with different symmetry classes, where the nature of the bound solitons and thus of the hybridized state is in general distinct from \mathbb{Z}_2 topological band insulator, other novel topological states may emerge accordingly. For instance, lattice dislocations in Sr_2RuO_4 , a candidate for chiral p -wave superconductor, can host Majorana modes [165], which are expected to hybridize into novel superconducting states [166].

6.A Emergent time reversal symmetric semi-metals at grain boundaries

In this Appendix we present details on the emergence of the grain boundary metal in the specific setting of the models considered in the previous Chapters. Nonetheless, we stress that these evaluations should be considered as an illustration of the general outlined principles, which in fact solely depend on the characteristic appearance of dislocation modes in translationally active phases and their according hybridization in TRS protected systems.

6.A.1 Lattice dislocations and spinon zero mode hybridization

Turning first to $2 + 1$ dimensions, we recall that by taking the continuum limit of the $M - B$ model (3.41), the localized spinon zero modes $\Phi_s = \sum_r \phi_s(\mathbf{r}) \Psi_{s,\mathbf{r}}$ can be solved analytically near $M/B \rightarrow 8$ in the absence of the Rashba term. For a single spin component with a dislocation located at the origin, these solutions are given in terms of the orbital space spinors

$$\phi_{\uparrow}(\mathbf{r}) = \frac{\sin(\lambda r)}{N\sqrt{r}} e^{-r/\xi} \begin{pmatrix} e^{-i\theta} \\ i \end{pmatrix}, \quad (6.7)$$

where we adopted polar coordinates $\mathbf{r} = (r, \theta)$, $\xi = 2B$, $\lambda = \sqrt{1 - 4MB}/2B$ and N is a normalization constant. Time-reversal symmetry then requires that $\phi_{\downarrow}(\mathbf{r}) = \phi_{\uparrow}^*(\mathbf{r})$ and guarantees that even if these two modes are localised on the same dislocation, they do not hybridize even in the presence of a Rashba coupling. Consequently, isolated dislocations deep in the M -phase bind a Kramers pair of exponentially localized modes, the wavefunctions of which exhibit spatial oscillations at the wavelength λ , which depends on the microscopic parameters.

In the presence of many dislocations, all the bound modes $\Phi_{i,s}$ remain at mid gap energy as long as the separation d between all the dislocations satisfies $d \gg \xi$. Nonetheless, when two dislocations are brought into proximity ($d \approx \xi$), the wavefunctions overlap, giving rise to finite (possibly spin-flipping) tunneling amplitudes $t_{ss',|i-j|} \sim \int d\mathbf{r} \phi_{s,i}^{\dagger}(\mathbf{r}) \phi_{s',j}(\mathbf{r})$. As a result, the spinon modes hybridize, resulting in a pair of Kramers degenerate modes at finite energy $\varepsilon \sim t$ that are localized on both dislocations. In principle, this hybridization energy ε could be analytically obtained, but as the analytic solution is only applicable in the $M/B \rightarrow 8$ regime, let us perform a numerical analy-

sis instead. Figure 6.4(A) shows that the resulting two dislocation hybridization energy obeys the qualitative form $\varepsilon(d) \propto \cos(\lambda d)e^{-d/\xi}$ throughout the M -phase, with the wavelength λ decreasing with smaller M/B . These oscillations in the hybridization energy, that can cause a change of sign as function of dislocation separation d and thus energetically favor different specific separations, are qualitatively similar to π -flux vortices in other Dirac-like systems [167, 168]. We also find that while the localized spinon modes (6.7) possess full rotational symmetry near $M/B \rightarrow 8$, for smaller values they become anisotropic as the band gap minimum switches from the M -point (full rotation symmetry) to the X - and Y -points (C_4 symmetry of the square lattice). Therefore, it follows that also the hybridization energy should become anisotropic.

Let us now address the emergent state at the grain boundary. A grain boundary at small opening angle θ is well approximated by a 1D array of lattice dislocations. These again hybridize pairwise, with the hybridization energy ε as the function of the GB opening angle θ shown in Figure 6.4(B). Assuming only nearest-neighbor hybridization, which should be a good approximation for small angles due to the exponential localization of the spinon modes, the hybridization along the GB is thus governed by the time-reversal symmetric and S_z conserving tight-binding Hamiltonian

$$H_{2D} = \sum_j (i\varepsilon \psi_{\uparrow,j}^\dagger \psi_{\uparrow,j+1} - i\varepsilon \psi_{\downarrow,j}^\dagger \psi_{\downarrow,j+1} + \text{h.c.}), \quad (6.8)$$

where $\psi_{s,j}$ are the annihilation operators for the Kramers pair of the spinon modes at dislocation j . These operators are related by the anti-unitary TRS operator T , satisfying $T^2 = -1$, via $T \psi_{\uparrow,j} T^{-1} = \pm \psi_{\downarrow,j}$. Assuming translational invariance, a Fourier transform then gives a diagonal spectrum with dispersion $E_\pm(q) = \pm 2\varepsilon \sin(q)$. Figure 6.4(C) shows that as the opening angle θ of the grain boundary gets smaller, i.e. the spacing $d = |\mathbf{b}|/\tan \theta$ between the dislocations becomes larger and nearest-neighbor approximation is expected to be justified, the spectra of GB bands are indeed accurately approximated by this simple tight-binding model with the relevant two-spinon hybridization energy $\varepsilon(d)$ as the only input.

As a next step, we consider S_z conservation breaking terms by including the Rashba term,

$$T\boldsymbol{\delta} \rightarrow T\boldsymbol{\delta} + i\frac{R}{2}(\tau_0 + \tau_z)\mathbf{e}_z \cdot (\boldsymbol{\sigma} \times \boldsymbol{\delta}) \quad (6.9)$$

in Eq. (3.41), thereby allowing for spin-flipping tunneling $t_{s \neq s'}$ processes. Although this makes the hybridization problem more involved, on a qualitative level TRS still

enforces all the momentum space terms $h(q)$ of Eq. (6.4) to be odd, implying that the nodes survive as long as the bulk band gap does not close. We note in this regard that momentum terms $h_0(q)$ proportional to the identity σ_0 are ruled out *at the nodes* by charge neutrality of the valley degrees of freedom, which finds its origin in the Nielsen-Ninomiya theorem [33, 34] and the manifestation of TRS in the spinon space. Indeed, TRS enforces $d_0(q)$ to be an even function, whereas the degeneracy or chiral symmetry of the nodes in fact generates a particle hole symmetry that simultaneously demands $h_0(k)$ to be odd. Moreover, since the hybridization follows from spinon wavefunction overlaps, the system is subjected to the constraint $\sum_{s,s'} |t_{s,s'}| = 1$. Hence, to leading order in $t_{s \neq s'}/t_{s=s'}$ the effect of a Rashba coupling is to suppress the hybridized bandwidth by $\sqrt{1 - t_{s \neq s'}/t_{s=s'}}$. Accordingly, we have verified this numerically as displayed in Figure 6.5(A).

Finally, if TRS is broken in the original model by a S_z conserving Zeeman term $B_z \tau_0 \otimes \sigma_z$, the localized spinons obtain a mass of the same magnitude. This translates, as shown in Figure 6.5(B), to a shifting of the spinon bands in opposite direction of energy. On the other hand, the S_z breaking Zeeman terms $B_{x,y} \tau_0 \otimes \sigma_{x,y}$ modify the spinon wavefunctions (all four components become nonvanishing, since the Hamiltonian is no longer block-diagonal in the S_z -basis), but do not result in a spinon mass term. Consequently, the hybridized spectrum remains unchanged as long as the bulk band gap does not close.

6.A.2 Helical modes on dislocation lines and their hybridization

The above mechanism generalizes straightforwardly to translationally active phases in three spatial dimensions. Focussing for concreteness on the R -phase of the $M - B$ model (see Eqs. (2.8) and (5.6)), a dislocation now entails a line-like object binding a pair of helical modes that propagate along it. In addition, the spin of these helical modes is parallel to the dislocation line, which is taken to be the \hat{z} -direction in the remainder. As a result, the helical modes around the TRS momentum $K_z = \pi$ are minimally described by $H = v_z \tilde{k}_z \sigma_z$, where \tilde{k}_z is the effective momentum in the vicinity of the TRS momentum and v_z is the velocity of the 2D surface states along the \hat{z} -axis [138]. Nevertheless, when two parallel dislocations lines are brought in proximity, time-reversal symmetric spin-flipping back-scattering terms get allowed (there is no S_z conservation in the 3D model) and the helical modes hybridize. Indeed, in exact analogy to the 2D case, we find that the

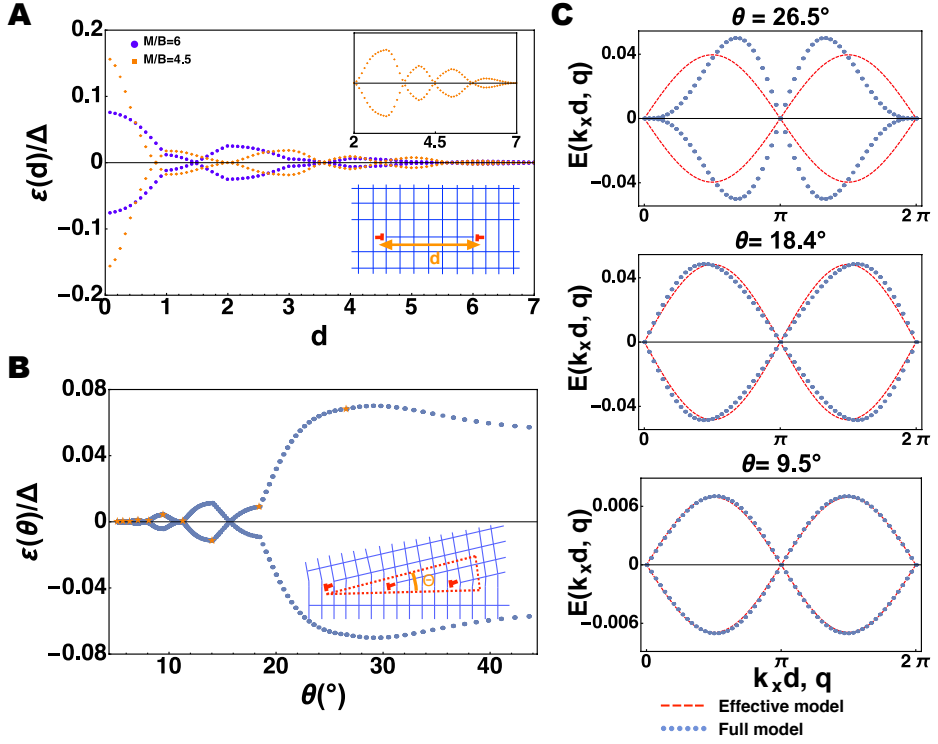


Figure 6.4: (A) The hybridization energy ε as the function of the separation d between two dislocations in units of the bulk band gap Δ . For different values of M/B the hybridization energy always exhibits exponential decay and characteristic oscillations that exhibit clear sinusoidal oscillations at larger separations (inset). The kinks as functions of d are artefacts of simulating smooth dislocation transport by adiabatically switching on and off the relevant couplings. (B) The two dislocation hybridization energy ε in the GB geometry as the function of the GB angle θ in units of the bulk band gap Δ . (C) The mid-gap spectra of the full model across the reduced Brillouin zone $0 < k_x < 2\pi/d$ for different GB angles $\theta = \arctan(|b|/d)$ and the approximation of each by the effective tight-binding model (6.8) over the $0 < q < 2\pi$ with the hybridization energy $\varepsilon(d)$ as the only input. As the dislocation separation $d \sim \theta^{-1}$ increases, the nearest-neighbor approximation becomes better and we find excellent agreement. All data has been produced using a 90×60 system with $M/B = 6$.

hybridization energy $\varepsilon(k_z)$ at the TRS momentum $K_z = \pi$ exhibits similar characteristic oscillations and an exponential decay with the dislocation line separation d .

Accordingly, we can address the physics of a grain boundary in a 3D TBI as a hybridization problem of a 2D sheet of straight parallel dislocation lines. In particular, parametrizing the direction along the dislocation lines as the \hat{z} -axis and the direction along the grain boundary as the \hat{x} -axis, leaving the \hat{y} -axis to be normal to the GB plane, the effective description takes the form

$$H(q, \tilde{k}_z) = v_f \tilde{k}_z \sigma_z + 2\varepsilon(\tilde{k}_z) \sin(q) \sum_a t_a(\tilde{k}_z) \sigma_a. \quad (6.10)$$

This generic form immediately conveys the nodal properties of the emergent band structure on grounds of the same principles applicable to the 2D case. That is, the hybridization results in a 2D spectrum that is gapped everywhere except at the TRS momenta $(k_x, k_z) = (0, \pi)$ and $(k_x, k_z) = (\pi/d, \pi)$. Nonetheless, in principle we expect the effective Hamiltonian to be even simpler. Indeed, performing for instance a rotation $R = e^{i\theta \sigma_z/2}$, with $\theta = \tan(t_2/t_1)$, it is straightforward to see that the σ_z term is unaltered, while the other q -dependent terms become proportional to σ_x . Moreover, from a physical perspective we know that the valley degrees of freedom are in fact associated with the edge state channels at either side of the GB, as conveyed by Fig. 6.3(A). Since such edge states are well-known to be helical [45, 142], we hence anticipate the grain boundary metal to be accurately described by the effective Hamiltonian

$$H_{3D}(q, \tilde{k}_z) = v_z \tilde{k}_z \sigma_z + 2\varepsilon \sin(q) \sigma_x, \quad (6.11)$$

which is again rooted in the mentioned chiral symmetry of the nodes and finds further concrete motivation in the next Subsection. Correspondingly, the dispersion around these momenta exhibits anisotropic spectral cones of opposite chirality, with the velocities along and perpendicular (along the GB) to the dislocation lines being given by v_z and 2ε , respectively. Akin to the 2D case, our numerics show that the magnitude of the spectral gap between the TRS momenta along k_x can indeed accurately be deduced from the bi-partite hybridization energy ε . Finally, turning to the TRS breaking perturbations, we find that the $B_y \tau_0 \otimes \sigma_y$ Zeeman term enables back-scattering of the helical modes in each dislocation line and immediately gaps the hybridized spectrum. On the other hand, the Zeeman terms in the plane of the GB, $B_{x,z} \tau_0 \otimes \sigma_{x,z}$, only modify the bandwidth without gapping the chiral cones.

Although, we are convinced about the form of Eq. (6.11) by the outlined arguments, definite confidence has to be found in an exact, yet model independent, mathematical argument. The relevance of this question is also reflected in the emergence of edge states. Namely, as both nodes feature an opposite winding [169], we expect interesting Fermi arc-like contributions to the surface states of the parent TBI [147]. A complementing direct indication finds its origin along the lines of Eq. (2.15). Specifically, considering the effective model (6.11) on a similar semi-infinite plane geometry, $z > 0$, relative to a reference vacuum, the question of existence of edge states heuristically corresponds to finding normalizable, boundary localized, zero energy states of the equation

$$(iv_z \partial_z \sigma_z + 2\varepsilon \sin(q) \sigma_x) \psi(z, q) = 0, \quad (6.12)$$

where $\pi < q = k_x/d < 2\pi$. Consequently, we see that the formal solutions

$$\psi(z, q)_\pm = e^{\frac{1}{v_z} \int_0^z dz' m(q, z')} \sigma_z \phi_\pm, \quad (6.13)$$

in terms of $\sigma_y \phi_\pm = \pm \phi_\pm$ and $m(q, z) = 2\varepsilon \sin(q)$, are spin split in momentum space. That is, one spin polarization is spanning the momentum range $0 < q < \pi$ of the projected Brillouin zone, whereas the other is spanning the complement. Since this situation is reversed at an assumed opposite edge, we thus observe the immediate similarity with 3D Weyl semi-metals [147]. Nonetheless, since the GB terminates on the surface of a TBI, the system must also host the usual TBI surface states. Therefore, in spite of the discrepancy of effective momentum of these states, the detection of the Fermi arc-like components via optical conductivity measurements [170] is likely to be challenged by unexplored hybridization phenomena.

6.A.3 Analytical motivation

While the previous two subsections conveyed the essential principles underlying the formation of the grain boundary semi-metal, let us now further motivate the generic mechanism from a more concrete point of view using a continuum approximation. Starting directly from the Volterra construction, the emergent dislocation modes in the parent translationally active topological band insulator can then heuristically be understood as solitons resulting from the effective coordination discrepancy. In particular, considering the imaginary Volterra cut in the plane of well-defined momentum $\mathbf{k} \cdot \hat{\mathbf{t}}$ (or the single plane without the notion of the perpendicular momentum in the two dimensional case),

one may assign two Kramers pairs of edge states to either side, which get accordingly gapped by the subsequent gluing process. In the case of a dislocation, however, these edges are misaligned upon a translation by the Burgers vector \mathbf{b} . This consequently translates into an effective phase shift $\mathbf{K}_{inv} \cdot \mathbf{b}$ of the hopping terms across the imaginary Volterra cut inducing a single pair of dislocation modes, as detailed by the evaluations in 2D and the $\mathbf{K}\text{-}\mathbf{b}\text{-}\mathbf{t}$ rule in 3D [138, 171].

The resulting spinon modes subsequently act as projection operators defining a reduced subspace, which adequately describes the semi-metal. Given the above results, one can therefore in principle construct the resulting midgap band structure and its relation to the edge states explicitly. However, in view of the complexity of the above solutions, let us at this moment illustrate matters from a complementary viewpoint. Specifically, assuming that the dislocation solitons may heuristically be modeled by a massive Dirac equation that changes sign at the defect core, a minimal description in the case of a 2D parent TBI attains the form

$$H(x) = (-i\partial_y)\mu_z \otimes (v\sigma_z + \alpha\sigma_y) + m(y)\mu_x \otimes \sigma_0. \quad (6.14)$$

In the above, the μ matrices parametrize the tunneling terms between the hypothetical edges, whereas the σ matrices act in the spin space of the associated edge states having dispersion $v\tilde{k}_y$ in the vicinity of the projected value of \mathbf{K}_{inv} . The change in mass term then effectively represents the attained phases of the hopping terms across the Volterra cut, which is taken to be the semi-infinite plane. That is, $m(y < 0) < 0$ and $m(y > 0) > 0$. Lastly, the term proportional to α effectively describes the breaking of S_z conservation due to the presence of the Rashba term.

The approximation (6.14) of the action of a dislocation with $\mathbf{b} = \mathbf{e}_y$ pertains to a toy model in every aspect. In particular, the richness regarding to the classification principles as outlined has to be incorporated actively. For example, in the two dimensional $p4$ phase, one has to assure that only the edge states corresponding to projected momentum $\tilde{k}_y = \pi$ feature a solitonic mass. Nevertheless, the compactness of the 'dislocation' solitons $\psi(y) = e^{1/v \int dy' m(y')} \phi$, where $\mu_y \otimes (v\sigma_z + \alpha\sigma_y)\phi = \sqrt{v^2 + \alpha^2}\phi$, and their corresponding projection operator $P = 1/2[1 + \mu_y \otimes (v\sigma_z + \alpha\sigma_y)/\sqrt{v^2 + \alpha^2}]$ does allow for an explicit illustration of the general projection mechanism, which should be generic in case core details of the modes can safely be ignored. Specifically, the general S_z preserving nearest-neighbor coupling between the spinon modes, forming the above

translationally invariant grain boundary in the \hat{x} -direction, is simply given by

$$H_{GB}(q) = 2t \cos(q) \mu_x \otimes \sigma_0 + 2t \sin(q) \mu_y \otimes \sigma_0, \quad (6.15)$$

where q spans the associated reduced Brillouin zone. Similarly, the spin flipping amplitudes in presence of the Rashba term ($\alpha \neq 0$) may be modeled as

$$H_{GB}^R(q) = 2t_R \sin(q) \mu_x \otimes \sigma_x + 2t_R \cos(q) \mu_y \otimes \sigma_x, \quad (6.16)$$

where as before we impose the total overlap condition $t + t_R = 1$ on the hopping amplitudes. We additionally note that, in principle, the term (6.16) may be generalized further, although being constraint by an evident relation to the defined projector. However, this should not alter the computations qualitatively, motivating this simple form. Finally, the time reversal symmetry breaking Zeeman terms B_j can also readily be incorporated as

$$B_j = b_j \mu_0 \otimes \sigma_j, \quad j = 1, 2, 3. \quad (6.17)$$

Having all terms in place, it is a simple matter to obtain the resulting effective description by projecting onto the subspace defined by the projection operator P near $x = 0$,

$$H_{eff} = P(H + H_{GB} + H_{GB}^R + \sum_j^3 B_j)P. \quad (6.18)$$

Concretely, using the above approximation, we then obtain

$$\begin{aligned} H_{eff}(q) = & \frac{\sin(q)}{\sqrt{v^2 + \alpha^2}} \left[t v \mu_0 \otimes \sigma_z - \alpha t_R \mu_z \otimes \sigma_z + t \sqrt{v^2 + \alpha^2} \mu_y \otimes \sigma_0 \right] + \\ & \frac{\sin(q)}{\sqrt{v^2 + \alpha^2}} \left[\sqrt{v^2 + \alpha^2} t_R \mu_x \otimes \sigma_x + \alpha t \mu_0 \otimes \sigma_y + t_R \mu_z \otimes \sigma_y \right] + \\ & \frac{v b_z + \alpha b_y}{2(v^2 + \alpha^2)} \left[v \mu_0 \otimes \sigma_z + \sqrt{v^2 + \alpha^2} \mu_y \otimes \sigma_0 + \alpha \mu_0 \otimes \sigma_y \right]. \end{aligned} \quad (6.19)$$

Accordingly, we retrieve a spectrum of the form

$$E(q) = \pm \sqrt{(4t^2 + 4t_R^2) \sin^2(q) + \frac{4t(vb_z + \alpha b_y) \sin(q)}{\sqrt{v^2 + \alpha^2}} + \frac{(vb_z + \alpha b_y)^2}{v^2 + \alpha^2}}, \quad (6.20)$$

in addition to the anticipated double zero eigenvalue. Hence, we find correspondence with the arguments and results of Subsection 6.A.1, albeit that the specific representation depends on the concrete model details. Indeed, by virtue of the zero eigenvalues, it is in

general possible to find a block diagonal form, which leads in case of $H_R = 0$ directly to Eq. (6.5) in terms of

$$\tilde{\sigma}_z = \left(v\mu_0 \otimes \sigma_z + \sqrt{v^2 + \alpha^2} \mu_y \otimes \sigma_0 + \alpha\mu_0 \sigma_y \right) / (2\sqrt{v^2 + \alpha^2}). \quad (6.21)$$

Moreover, the resulting two-band model subsequently has, in absence of the TRS breaking Zeeman terms B_j , a sinusoidal dispersion, the bandwidth of which gets reduced by increasing Rashba coupling. Furthermore, when $t_R = B_y = 0$, the Zeeman term B_z linearly gaps the spectrum, whereas B_y requires a finite Rashba to have an effect. Finally, we also note the natural particle hole symmetry \mathcal{P} generated by $\mu_z \otimes \sigma_z$ and the corresponding chiral symmetry C generated by $C = T\mathcal{P} = \mu_x \otimes \sigma_x$.

The same calculation can readily be repeated to support the general principles underlying the formation of grain boundary metals in 3D translationally active TBIs, as discussed in the previous Subsection. Assuming that the dislocation lines are oriented in the \hat{z} -direction, whereas the grain boundary is formed along the \hat{x} -direction, the analogue of Eq. (6.14) then reads

$$H(y, k_z)_{3D} = v(-i\partial_y \mu_z \otimes \sigma_y + \tilde{k}_z \mu_z \otimes \sigma_z) + m(y) \mu_x \otimes \sigma_0, \quad (6.22)$$

where we took advantage of the well-known helical texture of the edge states [45, 142]. As detailed by the **K-b-t** rule, \tilde{k}_z pertains to a well-defined quantum number and may be used to decompose a general dislocation spectrum in terms of its momentum depended descendant states. In particular, the dislocation modes and the corresponding projection operators are thus a function of \tilde{k}_z and lead to projective spinon states of finite energy when deviated away from the parent TRI momentum. As we are however interested in the nodal structure, let us therefore solely focus on $\tilde{k}_z = 0$. The projector onto the associated subspace is then simply given by $P_{3D} = 1/2[1 + \mu_y \otimes \sigma_y]$. Moreover, as the problem has no S_z conservation to begin with, we directly acquire

$$\begin{aligned} H_{eff,3D}(q, \tilde{k}_z) &= P_{3D}(H + H_{GB} + \sum_j^3 B_j)P_{3D} \\ &= 1/2[v\tilde{k}_z(\mu_z \otimes \sigma_z - \mu_x \otimes \sigma_x) + (b_y + t \sin(q))(\mu_0 \otimes \sigma_y + \mu_y \otimes \sigma_0)]. \end{aligned} \quad (6.23)$$

The above effective model again hosts two eigenvalues that identically equate to zero. More importantly, the two-band model spectrum is in this case given by

$$E(q, \tilde{k}_z) = \pm \sqrt{v^2 \tilde{k}_z^2 + (b_y + t \sin(q))^2}. \quad (6.24)$$

Hence, we again find direct connection with the previously obtained insights; the subsystem forms a semi-metal that is only gapped by TRS breaking Zeeman terms perpendicular to the grain boundary. As a matter of fact, we can define effective spin-1/2 Pauli matrices $\tilde{\sigma}_z = (\mu_z \otimes \sigma_z - \mu_x \otimes \sigma_x)/2$ and $\tilde{\sigma}_x = (\mu_0 \otimes \sigma_y + \mu_y \otimes \sigma_0)/2$, which anti-commute and square to identity in the projected subspace defined where $\mu_y \otimes \sigma_y = 1$. As result, the minimal model attains the anticipated form

$$H_{eff,3D}(q, \tilde{k}_z) = v\tilde{k}_z\tilde{\sigma}_z + (b_y - t \sin(q))\tilde{\sigma}_x, \quad (6.25)$$

connecting to the previous results.

The above evaluation, which can be adapted to the specific setting considered, thus reconfirms the general discussion on the stability and formation of the grain boundary metals. Nevertheless, we accentuate that general confidence in fact yet has to be found in more mathematically precise arguments, signifying the status of a grain boundary as a generic topological object.

6.B Disorder analysis of the grain boundary states

We here present numerical data on the stability of the graphene-like spinon semi-metal when random chemical potential disorder is included in the parent TBI. Such disorder breaks translational symmetry and can result in inter-node scattering that, when sufficiently strong, can gap out the extended state on the GB. Nonetheless, for small to moderate disorder the state is expected to be stable due to the collective quasiparticle nature of the spinon modes: local random chemical potential in the parent TBI is expected to only cause local random deformations on the wave functions and thus only lead to random tunneling terms in the effective models. These in turn translate to a random gauge field around the chiral cones that only shifts them around. Only when the mean displacement is of the order of q/d , i.e. of the order of the cone separation in momentum space, gapping is expected to take place. Consequently, large opening angle GBs are expected to be most stable.

To substantiate these general considerations, we have considered the effect of local random disorder on the bi-partite hybridization energies ε that enter the effective model as tunneling amplitudes. Figure 6.5(C) shows the data for the 2D case, conveying that even when the disorder averaged energies are strongly influenced by local random disorder (up to 50%) the system does not feature random sign flips. Thus, while any

disorder potential contains a Fourier component that corresponds to nodal scattering (perfect sign dimerization would gap out nodes even at maximal separation of π), we expect the spinon semi-metals not to gap out for small disorder. Indeed, the numerical data presented in Figure 6.5(D) shows in fact remarkable resilience with gapless mid-gap bands, that again persist for disorder strengths of up to 50%. We expect the similar stability to apply also for states on GBs in 3D.

Finally, we point out that another way random tunneling in the effective model can arise is due to random turns along the GB. Therefore, we extrapolate that the stability under local random disorder also implies stability in the absence of disorder, but with broken translational invariance along the GB. Indeed, Figure 6.5(D) shows that the gapless mid-gap state persists also for randomized GB positions along the GB. Thus while straight GBs are ideal for stability, we do not expect translational invariance to be a necessary requirement of the graphene-like spinon semi-metal to emerge along them.

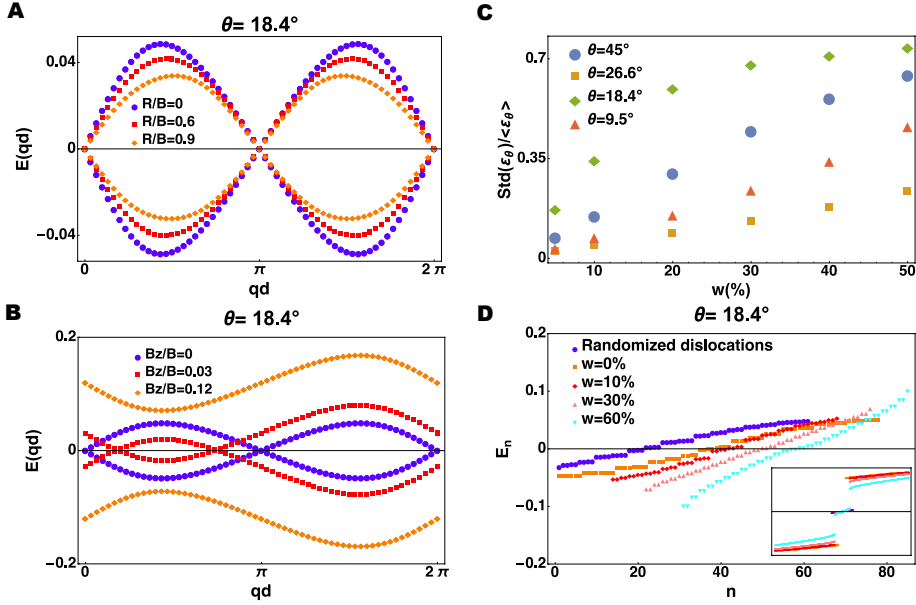


Figure 6.5: Stability of the graphene-like spinon semi-metal. (A) Inclusion of a Rashba term of magnitude R breaks S_z conservation, which leads to suppression of the bandwidth and different velocities at the cones, but TRS guarantees that the cones are stable. (B) An S_z conservation preserving Zeeman term of magnitude B_z , gives rise to a mass for the spinons. In the hybridized spectrum it shifts the spinon bands to opposite directions in energy and thereby moves the cones towards each other. The cones annihilate and gap out a quadratic touching point when B_z equals the bandwidth. (C) When local chemical potential disorder of magnitude w , i.e. μ is a random variable picked from box distribution $[(1-w)(M-4B), (1+w)(M-4B)]$, is introduced, the hybridization energies ϵ become also disordered with the fluctuations, as measurement by the standard deviation $\text{Std}(\epsilon)$ around the mean $\langle \epsilon \rangle$ increasing monotonously. The rate of increase depends on the microscopic details around the nearest-neighbour two dislocation hybridization energy corresponding to different GB angles θ as show in Figure 6.5(B). (D) In the full 2D TBI, we find that the gapless spinon semi-metal persists at least up to 50% chemical potential disorder (n enumerates the states), which is insufficient to close the bulk gap (inset). We have also simulated randomized dislocation positions (dislocations along the GB are randomly displaced by up to d lattice constants) and find similar stability. All data has been produced using a 90×60 system in 2D with $M/B = 6$. The disorder data has been produced for system size 42×30 , averaged over 100 disorder realizations.

Chapter 7

Conclusions and outlook

This thesis reflects an attempt to provide an alternative, lattice effect oriented, perspective on the old subject of topological band theory, which found revived research interest by virtue of the recently realized role of protecting symmetries. Although we believe that the intricate correspondence between our principal results and the presence of universal physical observables should result in an interesting agenda, only the course of time can reveal whether this old wine in a new glass will age well. Let us therefore seize the opportunity to put the obtained insights in more context, reflect upon a number of partly pursued ideas, and provide some outlooks.

Starting from the minimal continuum theory underlying the \mathbb{Z}_2 topological insulating state, the analytical evaluation presented in Chapter 3 reveals that the respective non-trivial entity can universally be probed by a π -flux vortex. From a heuristic perspective this was actually to be anticipated. Indeed, to date almost all bulk characterizations of topological order in fact revolve around the effects of symmetry consistent fluxes. Nonetheless, these insights in turn allowed for the identification of a related \mathbb{Z}_2 -flux observable that signifies the impact of the necessarily induced translation symmetry breaking by the underlying lattice: the dislocation. Accordingly, these considerations subsequently culminated in the prediction of profound 'zero-energy' dislocation modes, whose experimental verification would lie at heart of validating the essential results presented in this thesis. Given the omnipresence of dislocations in any sample and the status of techniques such as scanning tunneling spectroscopy in particular, we in fact feel that the only challenge of achieving this goal lies in establishing a suitable transitional active phase. Another appealing, yet unexplored, prospect of these modes centers around the

enticing theme of possible braiding statistics. As π -fluxes in \mathbb{Z}_2 topological insulators are known to display semionic behavior, we believe that the dislocation zero modes can hence provide for a realistic route of implementing this physics, where the spatial manipulation of the defects is being controlled by the application of shear stresses. Open questions in this regard, however, pertain to the considerations whether this semionic identification prevails for any generic transitionally active phase and, from a more fundamental point of view, where it finds its origin. Lastly, the zero modes might also prove to be consequential from a more mathematical angle. That is, our results actually allude to a generalization of the standard index theorem, characterizing the integer number of zero modes of a Dirac Hamiltonian, to a \mathbb{Z}_2 variant that governs the analytical result of the outlined effective theory.

Turning back to the formation principles, Chapter 4 then demonstrates that the dislocations modes actually manifest a natural space group classification of topological band insulators, analogous to the way edge states can be employed to discern the bulk \mathbb{Z}_2 order. Given its direct physical motivation, we therefore envisage the resulting indexing to find actual use as an experimental guide to the landscape of topological insulators. Nonetheless, from a principal standpoint it would be of future importance to rephrase the obtained insights actually in a more mathematical profound language. Although a number of proposals on this topic have surfaced recently, it is evident that concerning this aspect of the classification fundamental progress yet has been accomplished. This is not in the least place due to the elaborate infinite structure of a general space group and thus might disclose algebraic principles worth studying in their own right.

The space group classification also conveys that the proposed dislocation effects become even more pronounced in the arena of three spatial dimensions. This is not only expressed in the rich formation criteria addressed in Chapter 5, but moreover in the conceived related possibilities. Indeed, since dislocation lines still encode for effective fluxes, this leads to the suggestion that such defects may be exploited to study the braiding of non-trivial string-like objects. This is largely uncharted territory from a theoretical perspective, although one would expect intriguing relations with linking numbers and string theories, but certainly has had no better feasible connection with possible experimental implementation that we are aware of. Apart from these braiding considerations, the effective fluxes caused by dislocations might also find possible use in inducing striking features such as the Witten effect. Specifically, if the edge states of a topological insulator could be gapped without affecting the bulk topology, the surface endpoints of

dislocations would be expected to yield suchlike physical effects. Correspondingly, we have high hopes that the simultaneous inclusion of electromagnetic fluxes could lead to a very interesting new physical framework. As a specific instance, one can for example conceive the Gedankenexperiment of piercing a magnetic flux through a dislocation loop. Since the bound states are charged, it is obvious that this should result in a non-trivial outcome, being the product of an appealing interplay between the underlying topology, electromagnetism and the dynamics of a dislocation defect.

Finally, the physical content of the outlined results is furthermore reflected in the emergence of new states of matter due to the hybridization of many dislocation modes, as illustrated in Chapter 6. Of particular interest in this regard is the generality of the appearance of the retrieved semi-metal, suggesting that akin hybridization procedures in translational active topological insulators might lead to unexplored interesting phases. Our preliminary results on collective states of dislocations in two spatial dimensions, for example, show that such defect lattices generate mid-gap bands exhibiting well-defined Chern characters. Nonetheless, as pointed out in the previous Chapter, also the acquired isospinless graphene states themselves still pose worthwhile challenges. Indeed, detailing the hybridization interactions between the semi-metal, its edge states and the surface states of the parent topological insulator make up for an experimentally relevant pursuit, whereas ratifying the topological status of the grain boundary as an extended defect harbors a more principal question.

Let us then ultimately conclude by sketching a perceived distant horizon concerning the characterization of topological phases, that hosts from our perspective promising potential. Turning to general topologically non-trivial fermion systems it is evident that a unifying description is still far out of reach. Although in the context of the topological insulator the associated single particle description allows for a classification in the form of the tenfold way, a general physical interpretation of the difference to both intrinsic topological systems, displaying a ground state degeneracy, and the trivial counterparts is still lacking. This is also reflected in the fact that there is no consensus on the defining bulk field theory, besides the established response theory outlined in Chapter 2. We however suspect that by adopting a real space 'nodal' point of view one might shed light on the underlying structure. A reevaluation of the Hall effects already gives away some generic wisdoms in this regard. Starting from the single particle Landau levels (1.3), the

total antisymmetrized product state in complex coordinates z takes the simple form

$$\psi(z_1, \dots, z_n) = \prod_{i < j} (z_i - z_j) e^{-|z_i|^2/4l_B^2}. \quad (7.1)$$

Nonetheless, considering the Laughlin wavefunction

$$\psi(z_1, \dots, z_n) = \prod_{i < j} (z_i - z_j)^3 e^{-|z_i|^2/4l_B^2}, \quad (7.2)$$

one directly infers that the introduced sign structure has dramatic effects. Indeed, the above example of a fractional quantum Hall effect is a true quantum liquid and moreover features a topological ground state degeneracy. This in fact finds an interesting analogy in the effect of a non-trivial Chern number, which provides for an obstruction of writing band states as products of Wannier functions that are localized in both spatial dimensions. As a result, we therefore anticipate that a generic sign structure might be used to distinguish any symmetry protected state from a trivial product state, signifying the importance of the essential symmetry accordingly. For example in a \mathbb{Z}_2 topological band insulator, this could pertain to an odd number of minus signs that cannot be gauged away in the presence of time reversal symmetry. Furthermore, this would then at some level also correspond to the intricate effect of the considered monodromy defects, as they heuristically correspond to imposing anti-periodic boundary conditions along specific cuts.

Although the above ideas are still highly speculative, it is clear that from a topical standpoint we believe that the results presented in this thesis have only scratched the surface of a deeper framework that leaves quite some room for additional interesting physics to be explored.

References

- [1] A. Einstein, Herbert Spencer lecture delivered at Oxford (1933).
- [2] P. Anderson, *More is different*, Science **177**, 393 (1972).
- [3] V. Ginzburg and L. Landau, *To the theory of superconductivity*, Zh. Eksp. Teor. Fiz. **20**, 1064 (1950).
- [4] L. D. Landau and E. M. Lifshitz, *Statistical Physics, Third Edition: Volume 5* (Butterworth-Heinemann, 1980).
- [5] Y. Nambu, *Axial vector current conservation in weak Interactions*, Phys. Rev. Lett **4**, 380 (1960).
- [6] J. Goldstone, *Field theories with superconductor solutions*, Il Nuovo Cimento **19**, 154 (1961).
- [7] J. G. Bednorz and K. A. Müller, *Possible high- T_c superconductivity in the Ba-La-Cu-O system*, Z. Physik B **64**, 189 (1986).
- [8] G. 't Hooft, *Dimensional reduction in quantum gravity*, arxiv: gr-qc/9310026 (1993).
- [9] L. Susskind, *The world as a hologram*, J. Math. Phys. **36**, 6377 (1995).
- [10] J. M. Maldacena, *The large N limit of superconformal field theories and supergravity*, Adv. Theor. Math. Phys. **2**, 231 (1998).
- [11] S. S. Gubser, I. R. Klebanov, and A. M. Polyakov, *Gauge theory correlators from noncritical string theory*, Phys. Lett. B **428**, 105 (1998).

- [12] E. Witten, *Anti-de Sitter space and holography*, Adv. Theor. Math. Phys. **2**, 253 (1998).
- [13] K. von Klitzing, G. Dorda, and M. Pepper, *New method for high-accuracy determination of the fine-structure constant based on quantized Hall resistance*, Phys. Rev. Lett **45**, 494 (1980).
- [14] D. C. Tsui, H. L. Stormer, and A. C. Gossard, *Two-Dimensional magnetotransport in the extreme quantum limit*, Phys. Rev. Lett **48**, 1559 (1982).
- [15] X.-G. Wen, *Topological orders and edge excitations in FQH states*, Adv. in Phys. **44**, 405 (1995).
- [16] Z.-C. G. X. Chen and X.-G. Wen, *Local unitary transformation, long-range quantum entanglement, wave function renormalization, and topological order*, Phys. Rev. B **82**, 155138 (2010).
- [17] R. Laughlin, *Anomalous quantum Hall effect: an incompressible quantum fluid with fractionally charged excitations*, Phys. Rev. Lett **50**, 1395 (1983).
- [18] S. M. Girvin, A. H. MacDonald, and P. M. Platzman, *Collective-excitation gap in the fractional quantum Hall effect*, Phys. Rev. Lett **54**, 581 (1985).
- [19] R. Laughlin, *Quantized Hall conductivity in two dimensions*, Phys. Rev. B **23**, 5632 (1981).
- [20] D. Thouless, *Quantization of particle transport*, Phys. Rev. B **27**, 6083 (1983).
- [21] D. T. Q. Niu, *Quantised adiabatic charge transport in the presence of substrate disorder and many-body interaction*, J. Phys. A **17**, 2453 (1984).
- [22] D. J. Thouless, M. Kohmoto, M. P. Nightingale, and M. den Nijs, *Quantized hall conductance in a two-dimensional periodic potential*, Phys. Rev. Lett. **49**, 405 (1982).
- [23] Q. Niu, D. J. Thouless, and Y.-S. Wu, *Quantized Hall conductance as a topological invariant*, Phys. Rev. B **31**, 3372 (1985).
- [24] R. Kubo, *Statistical-mechanical theory of irreversible processes. I. General theory and simple applications to magnetic and conduction problems*, J. Phys. Soc. **12**, 570 (1957).

- [25] M. Nakahara, *Geometry, Topology and Physics* (IOP Publishing Ltd, 1990).
- [26] B. Simon, *Holonomy, the quantum adiabatic theorem, and Berry's Phase*, Phys. Rev. Lett. **51**, 2167 (1983).
- [27] F. Haldane, *Model for a quantum Hall effect without Landau levels: condensed-matter realization of the "parity anomaly"*, Phys. Rev. Lett. **61**, 2015 (1988).
- [28] G. Semenof, *Condensed-matter simulation of a three-dimensional Anomaly*, Phys. Rev. Lett. **53**, 2449 (1984).
- [29] P. R. Wallace, *The band theory of graphite*, Phys. Rev. **71**, 622 (1947).
- [30] R. Saito, G. Dresselhaus, and M. S. Dresselhaus, *Physical Properties of Carbon Nanotubes* (Imperial College Press, 1998).
- [31] C. L. Kane and E. Mele, *\mathbb{Z}_2 topological order and the quantum spin Hall effect*, Phys. Rev. Lett. **95**, 146802 (2005).
- [32] C. L. Kane and E. Mele, *Quantum spin hall effect in graphene*, Phys. Rev. Lett. **95**, 226801 (2005).
- [33] H. Nielsen and M. Ninomiya, *Absence of neutrinos on a lattice: (I). Proof by homotopy theory*, Nucl. Phys. B **185**, 20 (1981).
- [34] H. Nielsen and M. Ninomiya, *Absence of neutrinos on a lattice: (II). Intuitive topological proof*, Nucl. Phys. B **193**, 173 (1981).
- [35] M. F. Atiyah, *K-theory, Advanced Book Classics (2nd ed.)* (Addison-Wesley, 1989).
- [36] M. F. Atiyah, *Collected Works. Vol. 2 K-theory* (The Clarendon Press Oxford University Press, 1989).
- [37] L. Fu, C. L. Kane, and E. J. Mele, *Topological insulators in three Dimensions*, Phys. Rev. Lett. **98**, 106803 (2007).
- [38] L. Fu and C. L. Kane, *Topological insulators with inversion symmetry*, Phys. Rev. B **76**, 045302 (2007).

- [39] J. Moore and L. Balents, *Topological invariants of time-reversal-invariant band structures*, Phys. Rev. B **75**, 121306 (2007).
- [40] B. A. Bernevig, T. Hughes, and S. Zhang, *Quantum spin Hall effect and topological phase transition in HgTe quantum wells*, Science **314**, 1757 (2006).
- [41] M. König, S. Wiedmann, C. Brüne, A. Roth, H. Buhmann, L. Molenkamp, and S.-C. Z. X.-L. Qi, *Quantum spin Hall insulator state in HgTe quantum wells*, Science **318**, 766 (2007).
- [42] D. Hsieh, D. Qian, L. Wray, Y. Xia, Y. S. Hor, R. J. Cava, and M. Z. Hasan, *A topological Dirac insulator in a quantum spin Hall phase*, Nature **452**, 970 (2008).
- [43] Y. Xia, D. Qian, D. Hsieh, L. Wray, A. Pal, H. Lin, A. Bansil, D. Grauer, Y. S. Hor, R. J. Cava, and M. Z. Hasan, *Observation of a large-gap topological-insulator class with a single Dirac cone on the surface*, Nature Phys. **5**, 398 (2009).
- [44] Y. L. Chen, J. G. Analytis, J.-H. Chu, Z. K. Liu, S.-K. Mo, X. L. Qi, H. J. Zhang, D. H. Lu, X. Dai, Z. Fang, S. C. Zhang, I. R. Fisher, Z. Hussain, and Z.-X. Shen, *Experimental Realization of a Three-Dimensional Topological Insulator, Bi₂Te₃*, Science **325**, 178 (2009).
- [45] H. Zhang, C.-X. Liu, X.-L. Qi, X. Dai, and Z. F. S.-C. Zhang, *Topological insulators in Bi₂Se₃, Bi₂Te₃ and Sb₂Te₃ with a single Dirac cone on the surface*, Nature Phys. **5**, 438 (2009).
- [46] A. Altland and M. R. Zirnbauer, *Nonstandard symmetry classes in mesoscopic normal-superconducting hybrid structures*, Phys. Rev. B **55**, 1142 (1997).
- [47] A. Kitaev, *Periodic table for topological insulators and superconductors*, AIP Conf. Proc. **22**, 1132 (2009).
- [48] A. P. Schnyder, S. Ryu, A. Furusaki, and A. Ludwig, *Classification of topological insulators and superconductors in three spatial dimensions*, Phys. Rev. B **78**, 195125 (2008).
- [49] S. Ryu, A. P. Schnyder, A. Furusaki, and A. Ludwig, *Classification of topological insulators and superconductors in three spatial dimensions*, New J. Phys. **12**, 065010 (2010).

- [50] X. Chen, Z.-G. Gu, Z.-X. Liu, and X.-G. Wen, *Symmetry-protected topological orders in interacting bosonic systems*, Science **338**, 1604 (2012).
- [51] X. Chen, Z.-G. Gu, Z.-X. Liu, and X.-G. Wen, *Symmetry protected topological orders and the group cohomology of their symmetry group*, Phys. Rev. B **87**, 155114 (2013).
- [52] A. Mesaros and Y. Ran, *Classification of symmetry enriched topological phases with exactly solvable models*, Phys. Rev. B **87**, 155115 (2012).
- [53] Z.-G. Gu and X.-G. Wen, *Symmetry-protected topological orders for interacting fermions: Fermionic topological nonlinear σ models and a special group supercohomology theory*, Phys. Rev. B **90**, 115141 (2014).
- [54] X.-L. Qi, *Symmetry meets topology*, Science **338**, 1550 (2012).
- [55] R. Dijkgraaf and E. Witten, *Topological gauge theories and group cohomology*, Commun. Math. Phys. **129**, 393 (2014).
- [56] M. Kleman and J. Friedel, *Disclinations, dislocations, and continuous defects: A reappraisal*, Rev. Mod. Phys. **80**, 61 (2008).
- [57] H. Kleinert, *Gauge Fields in Condensed Matter* (World Scientific, 1989).
- [58] X. Lee and M. B. Y. Duan, *Torsion structure in Riemann-Cartan manifold and dislocation*, General Relativity and Gravitation **34**, 1569 (2002).
- [59] F. Hehl, P. von der Heyde, G. D. Kerlick, and J. M. Nester, *General relativity with spin and torsion: foundations and prospects*, Rev. Mod. Phys. **48**, 393 (1976).
- [60] A. Yavari and A. Goriely, *RiemannCartan geometry of nonlinear dislocation mechanics*, Archive for Rational Mechanics and Analysis **205**, 59 (2012).
- [61] Y. Aharonov and D. Bohm, *Significance of electromagnetic potentials in the quantum theory*, Phys. Rev. **115**, 485 (1959).
- [62] M. Levin and Z.-G. Gu, *Braiding statistics approach to symmetry-protected topological phases*, Phys. Rev. B **86**, 115109 (2012).

- [63] X.-G. Wen, *Symmetry-protected topological invariants of symmetry-protected topological phases of interacting bosons and fermions*, Phys. Rev. B **89**, 035147 (2014).
- [64] A. Kitaev, *Anyons in an exactly solved model and beyond*, Annals of Physics **321**, 2 (2006).
- [65] C. Nayak, S. H. Simon, A. Stern, M. Freedman, and S. D. Sarma, *Non-abelian anyons and topological quantum computation*, Rev. Mod. Phys. **80**, 1083 (2008).
- [66] V. Mourik, K. Zuo, S. M. Frolov, S. R. Plissard, E. P. A. M. Bakkers, and L. P. Kouwenhoven, *Signatures of majorana fermions in hybrid superconductor-semiconductor nanowire devices*, Science **336**, 1003 (2012).
- [67] C. W. J. Beenakker, *Search for majorana fermions in superconductors*, Annual Review of Condensed Matter Physics **4**, 113 (2013).
- [68] M. Berry, *Quantal phase factors accompanying adiabatic changes*, Proc. R. Soc. Lond. A **392**, 45 (1984).
- [69] X.-L. Qi, T. L. Hughes, and S.-C. Zhang, *Topological field theory of time-reversal invariant insulators*, Phys. Rev. B **78**, 195424 (2008).
- [70] X.-L. Qi, Y.-S. Wu, and S.-C. Zhang, *Topological quantization of the spin Hall effect in two-dimensional paramagnetic semiconductors*, Phys. Rev. B **74**, 085308 (2006).
- [71] A. Redlich, *Parity violation and gauge noninvariance of the effective gauge field action in three dimensions*, Phys. Rev. D **29**, 2366 (1984).
- [72] A. Redlich, *Gauge noninvariance and parity nonconservation of three-dimensional Fermions*, Phys. Rev. Lett. **52**, 18 (1984).
- [73] S.-S. Chern and J. Simons, *Characteristic forms and geometric invariants*, Annals of Mathematics **99**, 1 (1974).
- [74] S.-C. Zhang and J. Hu, *A four-dimensional generalization of the quantum Hall effect*, Science **294**, 26 (2001).

-
- [75] K. Hasebe, *Higher dimensional quantum Hall effect as A-class topological insulator*, Nucl. Phys. B **886**, 952 (2014).
- [76] S.-C. Zhang, *To see a world in a grain of sand*, arxiv: hep-th/0210162 (2002).
- [77] H. Hopf, *Über die Abbildungen der dreidimensionalen Sphäre auf die Kugelfläche*, Math. Ann. **104**, 637 (1931).
- [78] F. Haldane, *Fractional quantization of the Hall effect: a hierarchy of incompressible quantum fluid states*, Phys. Rev. Lett. **51**, 605 (1983).
- [79] J. von Neumann and E. Wigner, *Über das Verhalten von Eigenwerten bei adiabatischen Prozessen*, Phys. Z. **30**, 467 (1929).
- [80] C. Callan, R. F. Dashen, and D. Gross, *The structure of the gauge theory vacuum*, Phys. Lett. B **63**, 334 (1976).
- [81] R. Jackiw and C. Rebbi, *Vacuum Periodicity in a Yang-Mills quantum theory*, Phys. Lett. **37**, 172 (1976).
- [82] R. D. Li, J. Wang, X. L. Qi, and S. C. Zhang, *Dynamical axion field in topological magnetic insulators*, Nat. Phys. **6**, 284 (2010).
- [83] E. Witten, *Dyons of charge $e\theta/2\pi$* , Phys. Lett. B **86**, 283 (1979).
- [84] W. P. Su, J. R. Schrieffer, and A. J. Heeger, *Solitons in polyacetylene*, Pys. Rev. Lett **42**, 1698 (1979).
- [85] W. P. Su, J. R. Schrieffer, and A. J. Heeger, *Solitons excitations in polyacetylene*, Pys. Rev. B **28**, 1138 (1983).
- [86] A. J. Heeger, S. Kivelson, J. R. Schrieffer, and W. P. Su, *Solitons in conducting polymers*, Rev. Mod. Phys. **60**, 781 (1988).
- [87] F. Wilczek and A. Zee, *Linking numbers, spin, and statistics of solitons*, Pys. Rev. Lett **51**, 2250 (1983).
- [88] F. Wilczek, *Two applications of axion electrodynamics*, Pys. Rev. Lett **58**, 1799 (1987).
- [89] J. Zaanen, *The Classical Condensate*, course notes University of Leiden (1996).

- [90] R. Jackiw and C. Rebbi, *Solitons with fermion number 1/2*, Pys. Rev. D **13**, 3398 (1976).
- [91] R. Jackiw and P. Rossi, *Zero modes of the vortex-fermion system*, Pys. Rev. D **4**, 681 (1981).
- [92] M. Atiyah and I. M. Singer, *The index of elliptic operators on compact manifolds*, Bull. Amer. Math. Soc. **69**, 422 (1963).
- [93] M. Atiyah and I. M. Singer, *The Index problem for manifolds with boundary*, Ann. Math. **87**, 484 (1964).
- [94] J. Goldstone and F. Wilczek, *Fractional quantum numbers on solitons*, Pys. Rev. Lett **47**, 986 (1981).
- [95] C. Callan and J. A. Harvey, *Anomalies and fermion zero modes on strings and domain walls*, Nucl. Phys. B **250**, 427 (1985).
- [96] X. Wen, *Gapless boundary excitations in the quantum Hall states and in the chiral spin states*, Phys. Rev. B **43**, 11025 (1991).
- [97] J. M. Luttinger, *An exactly soluble model of a many-fermion system*, Journal of Math. Phys. **4**, 1154 (1963).
- [98] F. Haldane, *Luttinger liquid theory of one-dimensional quantum fluids*, J. Phys. C: Solid State Phys. **14**, 2585 (1981).
- [99] X.-L. Qi and S.-C. Zhang, *Spin-charge separation in the quantum spin Hall state*, Phys. Rev. Lett. **101**, 086802 (2008).
- [100] Y. Ran, A. Vishwanath, and D.-H. Lee, *Spin-charge separated solitons in a topological band insulator*, Phys. Rev. Lett. **101**, 086801 (2008).
- [101] V. Juricic, A. Mesaros, R. Slager, and J. Zaanen, *Universal probes of two-dimensional topological insulators: dislocation and π flux*, Phys. Rev. Lett. **108**, 106403 (2012).
- [102] G. Cho and J. E. Moore, *Topological BF field theory description of topological insulators*, Ann. of Phys. **326**, 1515 (2011).

-
- [103] Y. Aharonov and A. Casher, *Ground state of a spin-1/2 charged particle in a two-dimensional magnetic field*, Phys. Rev. A **19**, 2461 (1979).
- [104] R. Jackiw, *Fractional charge and zero modes for planar systems in a magnetic field*, Phys. Rev. D **33**, 2500 (1986).
- [105] M. M. Ansourian, *Index theory and the axial current anomaly in two dimensions*, Phys. Rev. Lett. B **70**, 301 (1977).
- [106] Y. Nishida, L. Santos, and C. Chamon, *Topological superconductors as nonrelativistic limits of Jackiw-Rossi and Jackiw-Rebbi models*, Phys. Rev. B **82**, 144513 (2010).
- [107] J. Weidmann, *Spectral Theory of Ordinary Differential Operators* (Springer-Verlag, 1987).
- [108] B. Thaller, *The Dirac Equation* (Springer-Verlag, 1992).
- [109] T. Fülöp, *Singular potentials in quantum mechanics and ambiguity in the self-adjoint hamiltonian*, Symmetry, Integrability and Geometry: Methods and Applications **3**, 107 (2007).
- [110] R. Jackiw, *Delta function potentials in two-dimensional and three-dimensional quantum mechanics* (1991).
- [111] A. Mesaros, R. Slager, J. Zaanen, and V. Juricic, *Zero-energy states bound to a magnetic π -flux vortex in a two-dimensional topological insulator*, Nucl. Phys. B **867**, 977 (2012).
- [112] A. Essin and J. E. Moore, *Topological insulators beyond the Brillouin zone via Chern parity*, Phys. Rev. B **76**, 165307 (2007).
- [113] Y. Zhang, J.-P. Hu, B. A. Bernevig, X. R. Wang, X. C. Xie, and W. M. Liu, *Quantum blockade and loop currents in graphene with topological defects*, Phys. Rev. B **78**, 155413 (2008).
- [114] L. D. Landau and E. M. Lifshitz, *Theory of Elasticity* (Pergamon Press, New York, 1980).

- [115] R. Bausch, R. Schmitz, and L. A. Turski, *Single-particle quantum states in a crystal with topological defects*, Phys. Rev. Lett. **80**, 2257 (1998).
- [116] H. Kleinert, *Gauge Fields in Condensed Matter*, vol.2 (Scientific, Singapore, 1989).
- [117] D. G. Rothe, R. W. Reinthaler, C.-X. Liu, L. W. Molenkamp, S.-C. Zhang, and E. M. Hankiewicz, *Fingerprint of different spinorbit terms for spin transport in HgTe quantum wells*, New J. Phys. **12**, 065012 (2010).
- [118] J. C. Y. Teo, L. Fu, and C. L. Kane, *Surface states and topological invariants in three-dimensional topological insulators: Application to $Bi_{1-x}Sb_x$* , Phys. Rev. B **78**, 045426 (2008).
- [119] L. Fu, *Topological Crystalline Insulators*, Phys. Rev. Lett. **106**, 106802 (2011).
- [120] T. H. Hsieh, H. Lin, J. Liu, W. Duan, A. Bansil, and L. Fu, *Topological Crystalline Insulators in the SnTe Material Class*, Nat. Comm. **3**, 982 (2012).
- [121] T. L. Hughes, E. Prodan, and B. A. Bernevig, *Inversion-symmetric topological insulators*, Phys. Rev. B **83**, 245132 (2011).
- [122] A. M. Turner, Y. Zhang, R. S. K. Mong, and A. Vishwanath, *Quantized response and topology of magnetic insulators with inversion symmetry*, Phys. Rev. B **85**, 165120 (2012).
- [123] L. Fu and C. Kane, *Time reversal polarization and a Z_2 adiabatic spin pump*, Phys. Rev. B **74**, 195312 (2006).
- [124] M. S. Dresselhaus, G. Dresselhaus, and A. Jorio, *Group Theory Application to the Physics of Condensed Matter* (Springer, Berlin, 2008).
- [125] D. Hsieh, Y. Xia, L. Wray, D. Qian, A. Pal, J. H. Dil, J. Osterwalder, F. Meier, G. Bihlmayer, C. L. Kane, Y. S. Hor, R. J. Cava, and M. Z. Hasan, *Observation of unconventional quantum spin textures in topological insulators*, Science **323**, 919 (2009).
- [126] S. Y. Xu, C. Liu, N. Alidoust, M. Neupane, D. Qian, I. Belopolski, J. D. Denlinger, Y. J. Wang, H. Lin, L. A. Wray, G. Landolt, B. Slomski, J. Dil,

- A. Marcinkova, E. Morosan, Q. Gibson, R. Sankar, F. C. Chou, R. J. Cava, A. Bansil, and M. Z. Hasan, *Observation of a topological crystalline insulator phase and topological phase transition in $Pb_{1-x}Sn_xTe$ material class*, Nat. Comm. **3**, 1192 (2012).
- [127] P. Dziawa, B. J. Kowalski, K. D. and R. Buczko, A. Szczerbakow, M. Szot, E. Lusakowska, T. Balasubramanian, B. M. Wojek, M. H. Berntsen, O. Tjernberg, and T. Story, *Topological crystalline insulator states in $Pb_{1-x}Sn_xTe$* , Nat. Mat. **11**, 1023 (2012).
- [128] Z. Wang, X.-L. Qi, and S.-C. Zhang, *Bulk-boundary correspondence of topological insulators from their respective Greens functions*, Phys. Rev. Lett. **105**, 256803 (2010).
- [129] A. M. Essin and V. Gurari, *Bulk-boundary correspondence of topological insulators from their respective Greens functions*, Phys. Rev. B **84**, 125132 (2011).
- [130] M. A. Zubkov and G. E. Volovik, *Momentum space topological invariants for the 4D relativistic vacua with mass gap*, Nucl. Phys. B **860**, 295 (2012).
- [131] M. A. Zubkov, *Generalized unparticles, zeros of the Green function, and momentum space topology of the lattice model with overlap fermions*, Phys. Rev. D **86**, 034505 (2012).
- [132] G. D. Mahan, *Many-Particle Physics*, 3rd ed. (Kluwer Academic, New York, 2000).
- [133] R. Slager, L. Rademaker, J. Zaanen, and L. Balents, *Impurity-bound states and Green's function zeros as local signatures of topology*, Phys. Rev. B **92**, 085126 (2015).
- [134] X. Zhanga, H. Zhang, J. Wang, C. Felser, and S. C. Zhang, *Actinide topological insulator materials with strong interaction*, Science **335**, 1464 (2012).
- [135] S. Murakami, *Quantum spin Hall phases*, Prog. Theor. Phys. Suppl. **176**, 279 (2008).
- [136] S. Murakami and S. Kuga, *Universal phase diagrams for quantum spin Hall systems*, Phys. Rev. B **78**, 165313 (2008).

- [137] C. Lu and I. F. Herbut, *Zero modes and charged skyrmions in graphene bilayer*, Phys. Rev. Lett. **108**, 266402 (2012).
- [138] Y. Ran, Y. Zhang, and A. Viswanath, *One-dimensional topologically protected modes in topological insulators with lattice dislocations*, Nat. Phys. **5**, 298 (2009).
- [139] J. C. Y. Teo and C. L. Kane, *Topological defects and gapless modes in insulators and superconductors*, Phys. Rev. B **82**, 115120 (2010).
- [140] Y. Ran, *Weak indices and dislocations in general topological band structures*, arxiv: 1006.5454 (2010).
- [141] K.-I. Imura, Y. Takane, and A. Tanaka, *Weak topological insulator with protected gapless helical states*, Phys. Rev. B **84**, 035443 (2011).
- [142] C.-X. Liu, X.-L. Qi, H. Zhang, X. Dai, Z. Fang, and S.-C. Zhang, *Model Hamiltonian for topological insulators*, Phys. Rev. B **82**, 045122 (2010).
- [143] B. Yan, M. Jansen, and C. Felser, *A large-energy-gap oxide topological insulator based on the superconductor BaBiO₃*, Nat. Phys. **9**, 709 (2013).
- [144] Y. Tanaka, Z. Ren, T. Sato, K. Nakayama, S. Souma, T. Takahashi, K. Segawa, and Y. Ando, *Experimental realization of a topological crystalline insulator in SnTe*, Nat. Phys. **8**, 800 (2012).
- [145] K. Kawamura, *A new theory on scattering of electrons due to spiral dislocations*, Z. Phys. B **29**, 101 (1978).
- [146] K. Kawamura, *Scattering of a tight-binding electron off an edge dislocation*, Z. Phys. B **48**, 201 (1982).
- [147] X. Wan, A. M. Turner, A. Vishwanath, and S. Savrasov, *Topological semimetal and Fermi-arc surface states in the electronic structure of pyrochlore iridates*, Phys. Rev. B **83**, 205101 (2011).
- [148] E. Witten, *Three Lectures On Topological Phases Of Matter*, arxiv: 1507.07698 (2015).

-
- [149] R. Takahashi and S. Murakami, *Gapless Interface States between Topological Insulators with Opposite Dirac Velocities*, Phys. Rev. Lett. **107**, 166805 (2011).
- [150] O. Yazyev and S. Louie, *Topological defects in graphene: Dislocations and grain boundaries*, Phys. Rev. B **81**, 195420 (2010).
- [151] J. Mannhart, H. Hilgenkamp, B. Mayer, C. Gerber, J. R. Kirtley, K. A. Moler, and M. Sigrist, *Generation of Magnetic Flux by Single Grain Boundaries of $YBa_2Cu_3O_{7-x}$* , Phys. Rev. Lett. **77**, 2782 (1996).
- [152] J. R. Kirtley, C. C. Tsuei, M. Rupp, J. Z. Sun, L. S. Yu-Jahnes, A. Gupta, M. B. Ketchen, K. A. Moler, and M. Bhushan, *Direct Imaging of Integer and Half-Integer Josephson Vortices in High- T_c Grain Boundaries*, Phys. Rev. Lett. **76**, 1336 (1996).
- [153] H. Hilgenkamp and J. Mannhart, *Grain boundaries in high- T_c superconductors*, Rev. Mod. Phys. **74**, 485 (2002).
- [154] S. Kim, K. Lee, H. A. Mun, H. Kim, S. Hwang, J. Roh, D. Yang, W. Shin, X. Li, Y. H. Lee, G. J. Snyder, and S. W. Kim, *Dense dislocation arrays embedded in grain boundaries for high-performance bulk thermoelectrics*, Science **348**, 6230 (2015).
- [155] Y. Liu, Y. Y. Li, S. Rajput, D. Gilks, L. Lari, P. L. Galindo, M. Weinert, V. K. Lazarov, and L. Li, *Tuning Dirac states by strain in the topological insulator Bi_2Se_3* , Nat. Phys. **10**, 294 (2014).
- [156] M. S. Foster and A. W. W. Ludwig, *Interaction effects on two-dimensional fermions with random hopping*, Phys. Rev. B **73**, 155104 (2006).
- [157] P. Anderson, *Absence of Diffusion in Certain Random Lattices*, Phys. Rev. **109**, 1492 (1958).
- [158] H. Nielsen and M. Ninomiya, *The Adler-Bell-Jackiw anomaly and Weyl fermions in a crystal*, Phys. Lett. B **130**, 6 (1983).
- [159] K. Nowack, E. M. Spanton, M. Baenninger, M. König, J. R. Kirtley, B. Kalisky, C. Ames, P. Leubner, C. Brüne, H. Buhmann, L. W. Molenkamp, D. Goldhaber-Gordon, and K. A. Moler, *Imaging currents in $HgTe$ quantum wells in the quantum spin Hall regime*, Nature Mat. **12**, 787 (2013).

- [160] Y. K. Kato, R. C. Myers, A. C. Gossard, and D. D. Awschalom, *Observation of the spin Hall effect in semiconductors*, Science **306**, 1910 (2004).
- [161] V. Sih, R. C. Myers, Y. K. Kato, W. Lau, A. C. Gossard, and D. D. Awschalom, *Spatial imaging of the spin Hall effect and current-induced polarization in two-dimensional electron gases*, Nat. Phys. **1**, 31 (2005).
- [162] R. R. Nair, P. Blake, A. N. Grigorenko, K. S. Novoselov, T. J. Booth, T. Stauber, N. M. R. Peres, and A. K. Geim, *Fine Structure Constant Defines Visual Transparency of Graphene*, Science **320**, 1308 (2008).
- [163] N. Xu, P. K. Biswas, J. H. D. and R. S. Dhaka, G. Landolt, S. Muff, C. E. Matt, X. Shi, N. C. Plumb, M. Radovic, E. Pomjakushina, K. Conder, A. Amato, S. V. Borisenko, R. Yu, H.-M. Weng, Z. Fang, X. Dai, J. Mesot, H. Ding, and M. Shi, *Direct observation of the spin texture in SmB6 as evidence of the topological Kondo insulator*, Nat. Comm. **5**, 4566 (2014).
- [164] D. J. Kim, J. Xia, and Z. Fisk, *Topological surface state in the Kondo insulator samarium hexaboride*, Nat. Mat. **13**, 466 (2014).
- [165] H. Y. T. L. Hughes and X.-L. Qi, *Majorana zero modes in dislocations of Sr_2RuO_4* , Phys. Rev. B **90**, 235123 (2014).
- [166] J. P. V. Lahtinen, A.W.W. Ludwig and S. Trebst, *Topological liquid nucleation induced by vortex-vortex interactions in Kitaev's honeycomb model*, Phys. Rev. B **86**, 075115 (2012).
- [167] M. Cheng, R. M. L. and V. Galitski, and S. D. Sarma, *Splitting of Majorana modes due to intervortex tunneling in a $p+ip$ superconductor*, Phys. Rev. Lett. **103**, 107001 (2012).
- [168] V. Lahtinen, *Interacting non-Abelian anyons as Majorana fermions in the honeycomb lattice model*, New J. Phys. **13**, 075009 (2011).
- [169] C.-H. Park and N. Marzari, *Berry phase and pseudospin winding number in bilayer graphene*, Phys. Rev. B **84**, 205440 (2011).
- [170] C.-H. Park and N. Marzari, *Coexistence of Fermi arcs with two-dimensional gapless Dirac states*, Phys. Rev. B **91**, 121109 (2015).

-
- [171] R. J. Slager, A. Mesaros, V. Juricic, and J. Zaanen, *Interplay between electronic topology and crystal symmetry: Dislocation-line modes in topological band-insulators*, Phys. Rev. B **90**, 241403 (2014).

List of Publications

- *Universal probes of two-dimensional topological insulators: Dislocation and π -flux*, Vladimir Juričić, Andrej Mesaros, Robert-Jan Slager and Jan Zaanen, Phys. Rev. Lett. **108**, 106403 (2012). [Chapter 3]
- *Zero-energy states bound to a magnetic π -flux vortex in a two-dimensional topological insulator*, Andrej Mesaros, Robert-Jan Slager, Jan Zaanen and Vladimir Juričić, Nucl. Phys. B **867**, 977 (2012). [Chapter 3]
- *The space group classification of topological band insulators*, Robert-Jan Slager, Andrej Mesaros, Vladimir Juričić and Jan Zaanen, Nat. Phys. **9**, 98 (2013). [Chapter 4, Science editors' choice]
- *Interplay between electronic topology and crystal symmetry: Dislocation-line modes in topological band insulators*, Robert-Jan Slager, Andrej Mesaros, Vladimir Juričić and Jan Zaanen, Phys. Rev. B **90**, 241403 (R) (2014). [Chapter 5]
- *Classification of nematic order in 2+1D: Dislocation Melting and $O(2)/Z_n$ lattice gauge theory*, Ke Liu, Jaakko Nissinen, Zohar Nussinov, Robert-Jan Slager, Kai Wu and Jan Zaanen, Phys. Rev. B **91**, 075103 (2015).
- *Impurity bound states and Green's functions zeroes as local signatures of topology*, Robert-Jan Slager, Louk Rademaker, Jan Zaanen and Leon Balents, Phys. Rev. B **92**, 085126 (2015). [Chapter 4]
- *Isospinless graphene on grain boundaries in topological band insulators*, Robert-Jan Slager, Vladimir Juričić, Ville Lahtinen and Jan Zaanen, *rejected in refereeing stage Science, submitted to Nature Physics*. [Chapter 6]

In preparation:

- *Chiral liquid crystals: the vestigial order of O and T matter*, Ke Liu, Jaakko Nissinen, Robert-Jan Slager and Jan Zaanen.
- *Lattice gauge theoretical description of nematic ordering*, Ke Liu, Jaakko Nissinen, Zohar Nussinov, Robert-Jan Slager, Kai Wu and Jan Zaanen.

Samenvatting

Theoretische natuurkunde als wetenschap tracht de rijkdom aan fysische fenomenen om ons heen te vatten in universele wiskundige vergelijkingen, die desalniettemin zo minimalistisch mogelijk zijn. De diepgaande schoonheid van dergelijke mathematische structuren wordt dan ook veelal gereflecteerd in hun toepasbaarheid op verschillende vraagstukken, al dan niet door middel van zogenaamde dualiteiten. Dit is niet in de laatste plaats het geval voor het deelgebied van de gecondenseerde materie, waar de beschrijvingen van emergente systemen die bestaan uit astronomische hoeveelheden deeltjes (waar men moet denken aan getallen in de orde van 10^{26}) vaak direct contact maken met de bekende fundamentele ijk- en zelfs snaartheorieën.

Vanuit een traditioneel oogpunt vinden de bovengenoemde analyses vaak hun oorsprong in algemene *symmetrieoverwegingen*. Daarnaast werd het in de jaren tachtig, voornamelijk met de ontdekkingen omtrent de kwantum Hall effecten, duidelijk dat zelfs begrippen vanuit het vakgebied van de *topologie* een bepalende rol kunnen spelen in de karakterisering van collectieve kwantummechanische gedragingen. Specifiek refereert topologie hier naar een tak van wiskunde die zich grofweg bezig houdt met de studie van vormen en ruimten; objecten die in dezelfde topologische klasse zitten, kunnen in elkaar vervormd worden door ze te buigen en op te rekken zonder te knippen of te plakken. Recentelijk is er echter juist interessante progressie geboekt door bestudering van de *samenhang* van de bovengenoemde a priori ongerelateerde benaderingen. Dit heeft in het bijzonder geleid tot de vinding van een tienvoudig mathematisch raamwerk, dat eenduidig alle mogelijke topologische toestanden van een willekeurig dimensionaal vrij-elektronsysteem in de aanwezigheid van een bepaalde discrete symmetrie uittelt.

Een hoogtepunt van deze ontwikkelingen wordt gevormd door de theoretische voorspelling en experimentele verificatie van het concept van de topologische band isolator. In een topologische isolator vormen de elektronen, net als in een normale isolator, een

incompressibele bandenstructuur, die evenwel een topologische identiteit heeft. Heuristisch gesproken betekent dit dat de elektrongolffuncties een onontwarbare knoop vormen die topologisch gezien niet tot een triviaal spectrum kan worden vervormd zolang de bepalende tijdsymmetrie (T-symmetrie) wordt gerespecteerd. Dit heeft verstrekkende fysische consequenties. Zo wordt een topologisch isolerend kristal gekenmerkt door onverwoestbare geleidende toestanden op de rand en bieden zulke topologische materialen bovendien de mogelijkheid tot de creatie van bijzondere majorana deeltjes, die ten grondslag zouden kunnen liggen aan de realisatie van de kwantumcomputer.

In dit proefschrift worden dergelijke structuren onderzocht vanuit een alternatief perspectief dat zich richt op de fundamentele aspecten van de onderliggende kristalsymmetrie. Het is namelijk een gegeven dat de bekende classificatieschema's, zonder uitzondering, berusten op de aanname dat de topologische variëteit van relevante momentum variabelen een torus betreft. In het bijzonder impliceert zo'n gedefiniëerde Brillouin zone via Blochs theorema het bestaan van een onderliggend rooster, waarvan de symmetrie wordt beschreven door een bijbehorende ruimtengroep. Een essentieel resultaat in dit proefschrift betreft dan ook een expliciete uitbreiding van het tienvoudige raamwerk met een classificatie die deze ruimtengroepsymmetrieën op natuurlijke wijze incorporeert. Bovendien worden deze resultaten fysisch inzichtelijk gemaakt door de bestudering van het rijke samenspel tussen deze beschrijving en de universele topologische defecten die de breking van de translatiesymmetrie van de vrije ruimte karakteriseren, te weten roosterdislocaties.

Na een bondige introductie, vangen wij deze queeste in hoofdstuk drie aan middels bestudering van het vereenvoudigde probleem van een π -flux dragende vortex in een twee-dimensionale (2D) topologische band isolator. Dit vraagstuk blijkt in de effectieve veldentheoretische benadering analytisch oplosbaar en we vinden dat zo'n vortex speciale nul-energie toestanden bindt. Deze toestanden herbergen rijke fysica an sich. Zo vertoont het emergente Kramers paar een scheidingsfenomeen van spin en lading; de excitaties dragen, afhankelijk van welke toestanden zijn opgevuld, *ofwel* spin *ofwel* lading relatief tot het vacuüm. Desalniettemin komen deze beschouwingen pas echt tot leven in het geval van dislocaties. We tonen namelijk aan dat, indien aan bepaalde voorwaarden wordt voldaan, roosterdislocaties in topologische band isolatoren kunnen worden opgevat als *effectieve* (π -) *fluxen* in een geometrische zin. Aangezien deze specifieke voorwaarden dus leiden tot verschillende responsen binnen dezelfde topologische klasse, duidt dit stante pede op het bestaan van de geanticiperde subclassificatie.

Dit idee wordt vervolgens wiskundig geformaliseerd in hoofdstuk vier en leidt zodoende tot een *ruimtegroep classificatie van topologische band isolatoren*. Hoewel deze beschouwing aangeeft dat er 18 2D en, op zijn minst, 70 verschillende 3D topologische isolerende fasen mogelijk zijn, identificeert dit schema bovendien 3 algemene klassen;

(I) Γ -fasen,

(II) Translationele actieve fasen,

(III) Kristallijne fasen.

De eerste twee categorieën zijn topologisch niet-triviaal in de zin van het genoemde tienvoudige raamwerk en vinden een bescherming in de vorm van de onderliggende T-symmetrie. Nochtans is er wel degelijk een verschil aangezien alleen representanten van de translationele actieve klasse dislocatietoestanden binden en dus ontvankelijk zijn voor roosterwanorde. De laatstgenoemde kristallijne groep wordt zelfs uitsluitend beschermd door de bepalende ruimtegroepsymmetrie. Tenslotte worden deze bevindingen ook nog belicht vanuit het perspectief van de Greense functies. In bijzonder vinden we dat de gevonden topologische structuur direct samenhangt met de aanwezigheid van nulpunten van de gereduceerde Greense functie op bepaalde doorsneden van de Brillouin zone.

Met de ruimtegroepordening van topologische fasen in handen, grijpen we vervolgens in hoofdstuk vijf terug op het responsmechanisme van dislocaties in drie ruimtelijke dimensies. Aangezien dislocatiedefecten in dit geval lijnen vormen, mag men verwachten dat deze beschouwing een grotere veelzijdigheid vertoont. Dit vermoeden wordt inderdaad gestaafd. Bovendien blijken deze resultaten natuurlijk onder een noemer te brengen met de gevonden classificatie, hetgeen ons primair voor ogen stond. Sterker nog, de uitkomsten kunnen worden verenigd in één simpele regel, die we bestempelen als de **K-b-t**-regel. Deze regel relateert zodoende de elektronische bandtopologie, beschreven door een effectief momentumpunt **K**, eenduidig met de onderliggende roostertopologie, welke gerepresenteerd wordt door dislocatielijnen met Burgersvector **b** en richtingsvector **t**.

Tenslotte besluiten we in hoofdstuk zes met een expliciete toepassing van de opgedane inzichten in de vorm van een studie rond zogenoemde korrelgrenzen in translationele actieve topologische materialen. Dergelijke oppervlakken ontstaan op breuklijnen tussen twee polykristallijne structuren en vormen een natuurlijke bron van dislocatienetwerken. Derhalve vertaalt dit vraagstuk zich direct naar een algemeen hybridisatiepro-

bleem van de eerder gevonden spin-lading gescheiden toestanden. Als gevolg van de, al dan niet emergente, symmetrieën resulteert dit vervolgens *op algemene gronden* in een *exotische semi-metallische bandenstructuur*, die veel raakvlakken heeft met het populaire grafeen en de recent ontdekte Weyl semi-metalen. Bovendien opent deze vinding een experimenteel toegankelijke route naar vele diepe natuurkundige fenomenen, waaronder verificatie van een illustere veldentheoretische anomalie en een expliciete manier om de oppervlaktetoestanden van de omvattende topologische isolator te manipuleren. Vanuit een breder perspectief gezien, sterken deze vele experimentele en theoretische implicaties dan ook onze overtuiging dat de bovengenoemde resultaten een interessante agenda kunnen vormen voor onderzoek in de nabije toekomst.

Curriculum Vitae

The author was born on the 24th of March 1988 in Goes, the Netherlands. Upon completion of the gymnasium as part of the bilingual pre-university stream vwo, an enrollment in mathematics and physics at the University of Leiden followed. The associated bachelor degrees were obtained three years later.

Subsequently, a master in theoretical physics was pursued. This track was cum laude concluded with the thesis entitled "Topological aspects of Aharonov-Bohm vortices in topological band insulators", which was carried out under the supervision of prof. dr. J. Zaanen. The results obtained during the master track were also awarded with a Shell prize. Moreover, after an extended summer holiday, this naturally resulted in the employment as a PhD researcher under the same supervisor at the Institute Lorentz of Leiden University. A coherent subset of this work is reported in this thesis.

The teaching duties during the PhD period comprised assisting the courses renewable energy at the University college the Hague, special relativity, statistical physics and elementary particles. In addition, other attempts to serve the community were made by acting as a reviewer for Phys. Rev. B and the American Department of Energy and by being a member of the Instituutsraad of the Leiden Institute of Physics.

Finally, the author had the privilege to attend conferences and/or to present his work in various places in Europe and the USA, including one invited opportunity at the EMRS meeting in Warsaw.

Acknowledgements

The moment I entered the building as a freshman I was quite intrigued by the theoretical physics section, as it seemed a rather special place. Now a few years later, I feel very privileged that in fact I have gotten the opportunity to be part of the warm atmosphere at the Institute Lorentz. Although I cannot appropriately acknowledge everybody in this short section, let me make a few exceptions.

First, I would like to express my gratitude to my supervisor Jan Zaanen. In spite of being a very achieved physicist with a proper critical eye, he nevertheless made me feel very much appreciated. Furthermore, I sincerely appreciate the effort of my other co-authors in all the conceived projects: Jaakko Nissinen, Kai Wu, Ke Liu, Zohar Nussinov, Louk Rademaker, Leon Balents, Ville Lahtinen, Andrej Mesaros and especially Vladimir Juričić. In this regard I also would like to thank Jaakko and Vladimir for proofreading parts of this thesis.

Apart from the scientific work, everybody in the institute has the good fortune that all other tasks are adequately taken care of by Marianne, Fran and Trudy, which certainly deserves mentioning. Additionally, I feel that the administrative machinery of the FOM should actually also be positively acclaimed for their effectiveness. Furthermore, other friendships that proved indispensable to get through the PhD process revolve around my physics friends/roommates comprising Bart, Thomas, Miguel, Louk and Bob.

Finally, words cannot express how grateful I am for my parents and my brother. Being quite a complex character, I have notwithstanding always been positively stimulated and raised in a prosperity that still reflects in every conceivable aspect of life. In fact, despite my parents' successes, they have provided us with some of the initial conditions that they were actually not given. I sincerely hope that our world lines will tie a highly non-trivial knot in the eternal fabric that is space-time.